CORROSION INHIBITION EFFECT OF MODIFIED SURFACE VIA NANOCAPSULE EMBEDDED COATING AND AL-SI-MG COATING

A Dissertation

by

CHANGKYU KIM

Submitted to the Graduate and Professional School of
Texas A&M University
in partial fulfillment of the requirements for the degree of

DOCTOR OF PHILOSOPHY

Chair of Committee,	Homero Castaneda
Committee Members,	Sarbajit Banerjee
	Raymundo Case
	Kelvin Xie
Head of Department,	Ibrahim Karaman

December 2021

Major Subject: Materials Science and Engineering

ABSTRACT

Corrosion of metals has been nominated as one of the major issues that contribute to material degradation which can ultimately trigger economic losses via unexpected accidents including material failure. The service period of metal can be extended by applying an either organic or inorganic coating. Nevertheless, the conventional coating types have shown their limitations regarding substrate protection, especially from the unintentionally formed defects or during their longer service time. Therefore, the improved coating systems have been required to extend the service period of the substrate by providing better protection.

To achieve enhanced and longer protection versus the conventional organic coating system, the application of corrosion inhibitor-loaded nanocapsules into the coating matrix was proposed as such technique allows overcoming the limitations existed in the case of the coating with directly applied corrosion inhibitor. According to the proposed studies, a corrosion inhibitor of triethanolamine was encapsulated with the double-shell-structured nanocapsules then embedded into the organic coating system that contained artificial defects. Upon the exposure to the corrosive electrolyte, the exposed metal surface experienced corrosion regime that caused pH gradient by couple anodic and cathodic reactions, and such pH gradient promoted autonomous healing of the corroded area by an accelerated release of the corrosion inhibitor from the nearby nanocapsules. As a result, by forming an inhibiting layer owing to the successfully released corrosion inhibitor, the

coating embedded with the nanocapsules revealed considerably delayed corrosion activity, allows a longer service period of such system at last.

To improve the anti-corrosion performance of the conventional Al-Si inorganic coating for hot-press-formed ultra-high-strength-steel system, the addition of Mg element was proposed. According to the proposed studies, the structural changes triggered by the addition of Mg element has been addressed, in both hot-dip-aluminizing and hot-press-forming processes. Such structural changes, including more compact surface layer with segregated Mg, thicker crack-free soft layer, and pore-filling effect of corrosion products, caused an improved anti-corrosion performance in terms of higher polarization resistance compared to the conventional Al-Si coating system.

DEDICATION

To my family.

ACKNOWLEDGEMENTS

First of all, I would like to express my sincere gratitude to my advisor, Dr. Homero Castaneda for his dedicated help, guidance, and encouragement throughout the course of this journey. He provided me many opportunities to learn not only the state-of-the-art techniques in corrosion field, but also how to think of new ideas, design experiments, write academic documents, and present my research in front of the audiences. Such valuable experiences enriched my journey towards Ph.D. degree and enlightened me to be an independent researcher equipped with professional attitude and scientific reasonings.

I would also like to thank my committee members, Dr. Sarbajit Banerjee, Dr. Raymundo Case, and Dr. Kelvin Xie for their valuable suggestions and support on my research project. I am also grateful to National Corrosion and Materials Reliability Center members who are the nicest and most talented people I have ever met. It was very lucky to have a chance to work with Dr. Ahmad Ivan Karayan, Dr. Seongkoo Cho, and Dr. Do-Eun Choe. With their helpful suggestions and efforts, I could have completed the journey more successfully. Thanks also goes to Lin Chen and Minho Lee who were always willing to share their time and provided valuable comments on my work. I also would like to express my sincere appreciation to whom not mentioned, but still supported and encouraged me.

Lastly, I sincerely thank my family for their unlimited support and unconditional love. None of my accomplishments would have been possible without their sacrifice and patience.

CONTRIBUTORS AND FUNDING SOURCES

Contributors

This work was supervised by a dissertation committee consisting of Professor Homero Castaneda (Department of Materials Science and Engineering), Professor Sarbajit Banerjee (Department of Chemistry), Professor Raymundo Case (Department of Materials Science and Engineering), and Professor Kelvin Xie (Department of Materials Science and Engineering) from Texas A&M University.

The part of work shown in Chapter 2, 3, and 4 was the result of collaboration with Dr. Jose Milla (Louisiana Department of Transportation and Development), Professor William Daly (Louisiana State University Department of Chemistry), Professor Christian Hilty (Texas A&M University Department of Chemistry), and Dr. Jihyun Kim (a former graduate student of Texas A&M University Department of Chemistry). Dr. Milla and Professor Daly helped with performing the encapsulation of TEA and TEM experiments, and Professor Hilty and Dr. Kim helped with performing the NMR experiments. In Chapter 5, Dr. Wonseog Yang, R&D Division in Hyundai Steel, prepared HPF samples and helped with performing the GDOES experiments. All other work conducted for the dissertation was completed by the student independently, including data processing and analysis.

All other work conducted for the dissertation was completed by the student independently.

Funding Sources

Graduate study was made possible in part by the funding sources including United States Department of Transportation (USDOT) Research and Innovative Technology Administration under Grant Number 17CLSU08, 19CTAM02, 19STLSU10 and 20CTAMU22, United States Department of Transportation (USDOT) Office of Pipeline Safety under Grant Number 693JK31910018POTA, TAMU-CONACyT under Grant Number 230303, Hyundai Steel Co. under Grant Number M1802824. Its contents are solely the responsibility of the authors and do not necessarily represent the official views.

NOMENCLATURE

Acronyms

AC	Alternating current
BA	Butyl acrylate
CPE	Constant phase element
CE	Counter electrode
DC	Direct current
DI	Deionized
DSS	Dimethyl-4-silapentane-1-sulfonic acid
ECR	Epoxy coated rebar
ED	Electrodeposited
EDS	Energy-dispersive X-ray spectroscopy
EEC	Electrical equivalent circuit
EGDMA	Ethylene glycol dimethyl acrylate
EIS	Electrochemical impedance spectroscopy
FAT	Fixed analyzer transmission
GDOES	Glow discharge optical emission spectrometer
HDA	Hot-dip-aluminizing
HF	High frequency
HPF	Hot-press-forming
LF	Low frequency

MAA	Methacrylic acid
MF	Mid frequency
MMA	Methyl methacrylate
NMR	Nuclear magnetic resonance
OCP	Open circuit potential
RE	Reference electrode
SCE	Saturated calomel electrode
SDBS	Sodium dodecyl benzenesulfonate
SEM	Scanning electron microscope
SVET	Scanning vibrating electrode technique
TC	Time constant
TEA	Triethanolamine
TEM	Transmission electron microscope
TXI	Triple resonance probe
UHSS	Ultra-high-strength-steel
WE	Working electrode
XPS	X-ray photoelectron spectroscopy
XRD	X-ray powder diffraction

Symbols

V_{SCE}	Potential versus SCE
Z'	Real part of impedance

Z''	Imaginary part of impedance
$\|Z\|$	Impedance modulus
R	Resistance
C	Capacitance
R_s	Solution resistance
R_c	Coating pore resistance
C_c	Coating capacitance
Q_c	CPE coating capacitance
n_c	CPE model parameter for CPE coating capacitance
R_f	Inhibiting layer resistance
C_f	Inhibiting layer capacitance
Q_f	CPE inhibiting layer capacitance
n_f	CPE model parameter for CPE inhibiting layer capacitance
R_{ox}	Oxide layer resistance
C_{ox}	Oxide layer capacitance
$\underline{Q_{ox}}$	CPE oxide layer capacitance
n_{ox}	CPE model parameter for CPE oxide layer capacitance
R_{ct}	Charge transfer resistance
C_{dl}	Double layer capacitance
Q_{dl}	CPE double layer capacitance
n_{dl}	CPE model parameter for CPE double layer capacitance
Z_D	Warburg impedance

Y_0	CPE model parameter
$\omega"_{max}$	Frequency at the maximum imaginary impedance
R_p	Polarization resistance
η	Inhibition efficiency
$R_{p,0}$	Polarization resistance in an absence of nanocapsules
C_c	Coating capacitance
R_{PB}	Pilling-Bedworth ratio
θ	XRD beam angle
W_R	Warburg diffusion resistance
W_T	Warburg time constant
χ^2	Goodness of fitting

TABLE OF CONTENTS

Page

LIST OF FIGURES

Page

LIST OF TABLES

Page

1. INTRODUCTION[*]

1.1. Corrosion of Metal

The corrosion of metals including material degradation not only affect to the material integrity but also leads to the economic losses by occurring unexpected accidents [1]. Corrosion of metals can be represented as the combination of 1) oxidation of metal and 2) reduction of water, as represented in equation (1) - (3) with an assumption of 2 valence metal ions. At the local anodic area, the oxidation of metal occurs, and the water reduction occurs at the local cathodic area. They have coupled each other to form an electrochemical corrosion cell that allows the continued metal loss of the substrate. Figure 1.1 also illustrates the schematic reaction path occurring in the corroding metal.

$$\text{Anode :} \quad 2\,M\,(s) \rightarrow 2\,M^{2+}\,(aq) + 4\,e^{-} \tag{1.1}$$

$$\text{Cathode :} \quad 2\,H_2O\,(l) + O_2\,(g) + 4\,e^{-} \rightarrow 4\,OH^{-}\,(aq) \tag{1.2}$$

$$\text{Overall :} \quad 2\,M\,(s) + 2\,H_2O\,(l) + O_2\,(g) \rightarrow 2\,M^{2+}\,(aq) + 4\,OH^{-}\,(aq) \tag{1.3}$$

It is also known that such reaction pathway is also thermodynamically preferred within the freely corroding potential range [2]. For example, in the H_2O-Fe system at around neutral (pH = 7) condition, shown in Figure 1.2 [3], the potential of Fe in between

[*] Part of this section is reprinted with permission from "Global and local parameters for characterizing and modeling external corrosion in underground coated steel pipelines" by Changkyu Kim[†], Lin Chen[†], Hui Wang, and Homero Castaneda, 2021. *Journal of Pipeline Science and Engineering*, 1, 17-35, Copyright © 2021 by Elsevier Ltd.

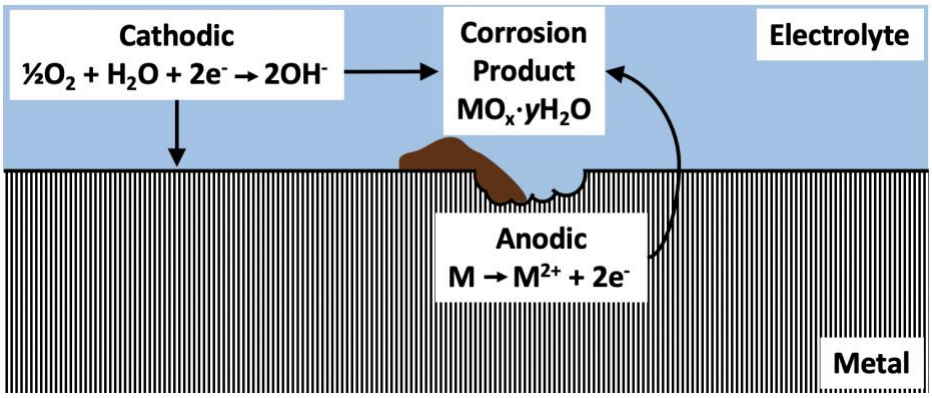

Figure 1.1. Schematic illustration of the corroding metal.

V_{SCE} = -0.2 V and -0.6 V are belonged to Fe^{2+} zone, which represents the formation of Fe^{2+} ion is thermodynamically preferable in such system. Therefore, the metal dissolution, also known as corrosion, is more favored in such range rather than the corrosion immunity illustrated as Fe in the presented Pourbaix diagram.

1.2. Conventional Organic Coatings

To delay the material degradation by suppressing the aforementioned electrochemical reactions, the coating has been applied on top of the metal substrate. The applied coating, either organic or inorganic, mostly aims to provide barrier protection that delays the water uptake hence the electrochemical reactions at the metal and electrolyte interface can be diminished.

Meanwhile, the barrier protection comes from the conventional coating is susceptible to the mechanical damage including scratch or holiday on the coating surface as shown in Figure 1.3. Once the metal is exposed by such damages, the part cannot be

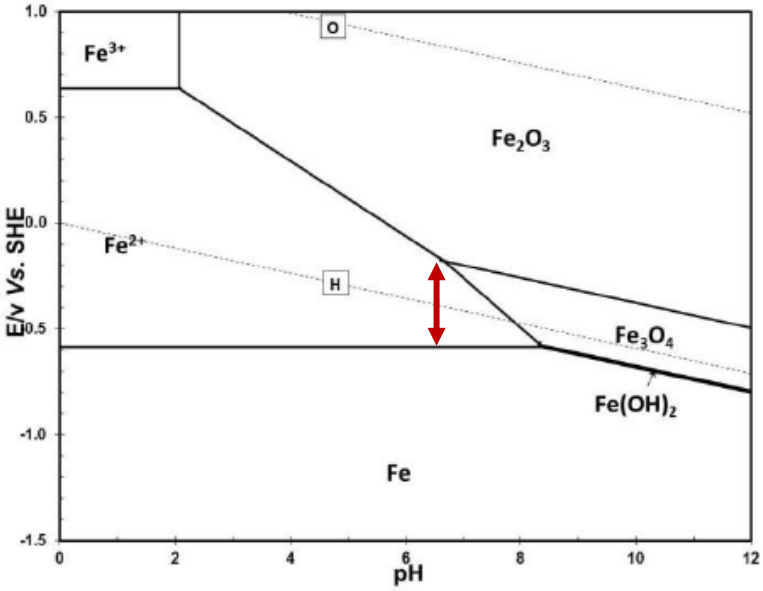

Figure 1.2. Pourbaix diagram for H_2O-Fe system at ambient condition.

protected anymore, and corrosion initiation occurs from the exposed substrate then propagates beneath the coating. Additionally, the coating can also be degraded once the water penetrates throughout the coating matrix and initiate the electrochemical reactions at the metal and coating interface. Since the corrosion product formed is generally known to be bulkier than the size of metal reacting [4], such formation of corrosion product in between the coating and substrate can trigger the delamination or blistering of the coating which also contribute to the accelerated corrosion by exposing more substrate to the electrolyte as shown in Figure 1.4 [5].

To overcome the aforementioned limitations of the conventional epoxy coating and provide the longer protection period of such coating system, the self-healing concept has been suggested with the usage of corrosion inhibitors [6,7]. Among the various types

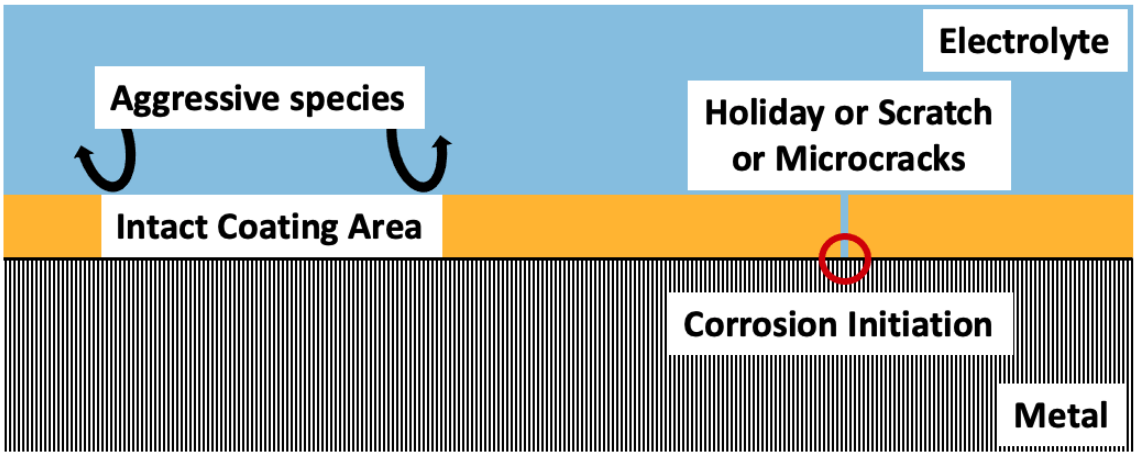

Figure 1.3. Schematic representation of the imperfect coating containing holiday or scratch or microcracks.

of corrosion inhibitors, the amine-based corrosion inhibitors has been popularly used since it can form an adsorption-derived barrier [8]. Such inhibitors can be applied either directly or indirectly, which the corrosion inhibitor is ad-mixed into the organic epoxy coating or the inhibitor is applied through the solution medium, respectively. The amine/silane-based coating [9] and polyaniline doped with inhibitor [10,11] studies showed the possible direct application of amine inhibitors to suppress metal oxidation through reducing the coating coupled with the substrate. On the other hand, the indirect application of amine-based inhibitors also have showed their potential to be used as anodic and cathodic inhibitors [12–15]. Among possible amine-based corrosion inhibitors, the triethanolamine (TEA) has been noticeable corrosion suppression even in chloride-rich environment due to its strong physisorption and chemical coordination ability [16–18].

Nevertheless, such applications of the inhibitor has revealed several drawbacks, including fast inhibitor exhaustion followed by either diminishment of barrier protection

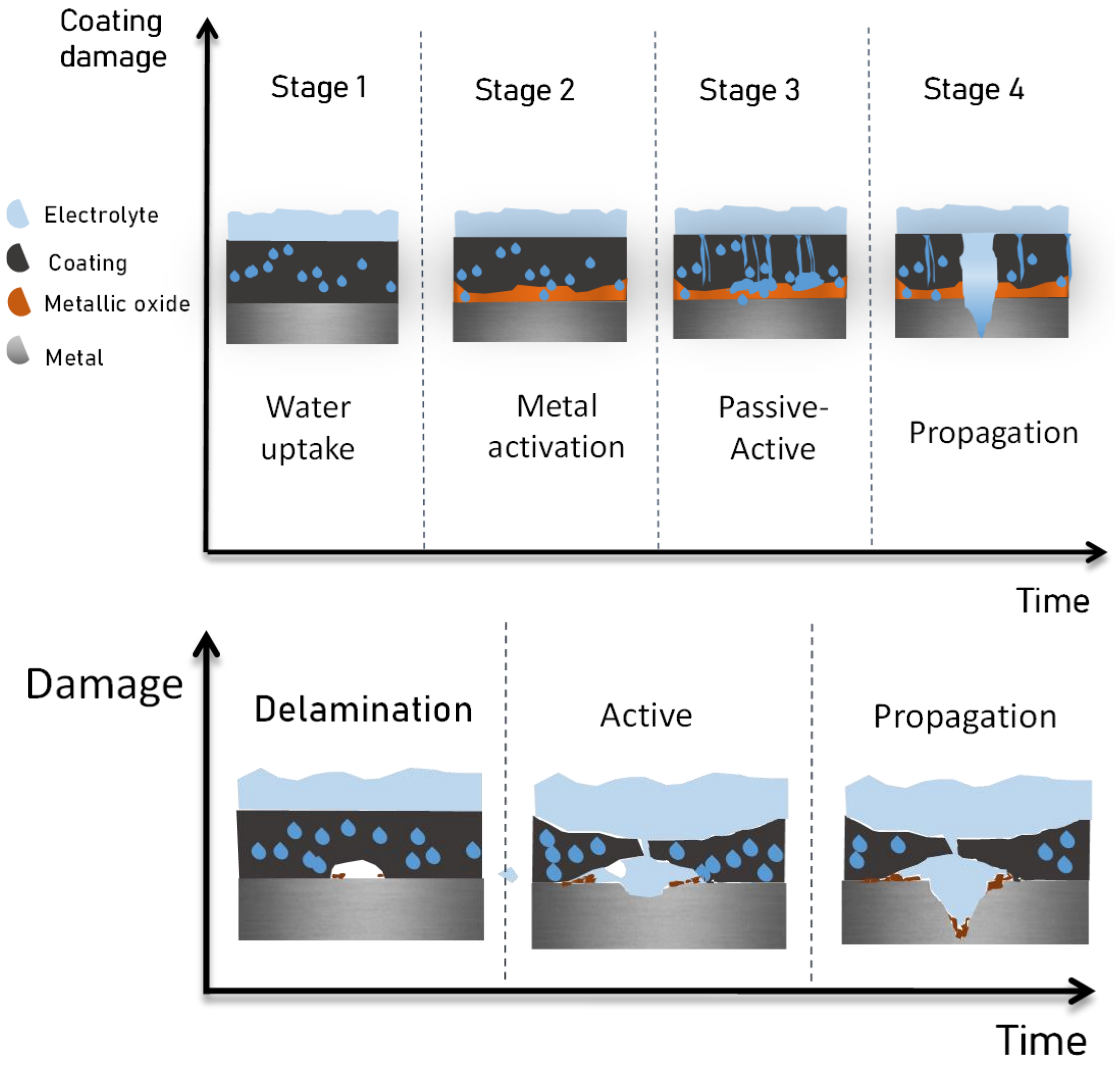

Figure 1.4. Damage evolution from intact organic coating to metal dissolution (top) and coating delamination (bottom).

or semipermeable film formation [19,20]. To overcome such limitations, the encapsulation concept has been suggested [21]. Such concept intends to produce the nano-sized capsules which containing the corrosion inhibitor, and the loaded inhibitors can be released only by a certain triggering action to prevent its fast exhaustion. The release-triggering

condition can be either mechanical rupture of the capsules by scratch and holiday or the local pH level change occurred by electrochemical reactions between metal and electrolyte [5]. It is expected that such application of nanocapsules into the organic coating can provide substrate protection for a long-term through the controlled-release of the corrosion inhibitor as illustrated more in-detail in Chapter 2.

1.3. Conventional Al-Si Coating for Hot-Press-Forming Steel

In case of the inorganic coating which may provide both barrier and cathodic protection, more complex risks exist, such as microcracks from its brittleness [22], delamination of coating from the formation of Kirkendall pores when heat-treatment exists [23], and alloying between coating and substrate [24], in addition to the aforementioned risks for the organic coating system. For instance, the Al-Si coating system that has been popularly used in automotive field for the ultra-high-strength-steel (UHSS) to enhance its anti-corrosion performance. The general coating application processes that include hot-dip-aluminizing (HDA), prolonged heat-treatment, and hot-press-forming (HPF) followed by water quenching [24]. The HDA process generally contains hot-dipping method under inert environment with thickness controlling action with nitrogen wiping. The coated sample is then heat-treated over 900°C in furnace to obtain austenite structure then pressed on die and quenched with water at an open environment.

It it has been known that the heat treatment applied to the substreate to perform austenization can induce the diffusion of the coating elements and substrate each other

[22]. Such diffusion phenomenon can result in the alloying among the Al, Si, and Fe during the heat-treatment period which reduces the cathodic protection capability of the coating [25]. Additonally, quenching process followed by the heat-treatment to achieve full martensitic microstructure for higher strength, can also induce the formation of microcracks, especially throughout the coating matrix by the difference in thermal expansion coefficient [24,26] that potentially decrease the anti-corrosion performance by allowing easier water-uptake through the existing microcracks. Additionally, it is also known that the Al-Si coating forms porous matrix, especially at the top-most surface which also contributes to the faster coating degradation [27]. Figure 1.5 illustrates the cross-sectional images of the Al-Si coating on 22MnB5 steel before and after the HDA and HPF processes, which reveals the existence of the numerous pores with microcracks that is indicative of the poor corrosion resistance up on the immersion condition.

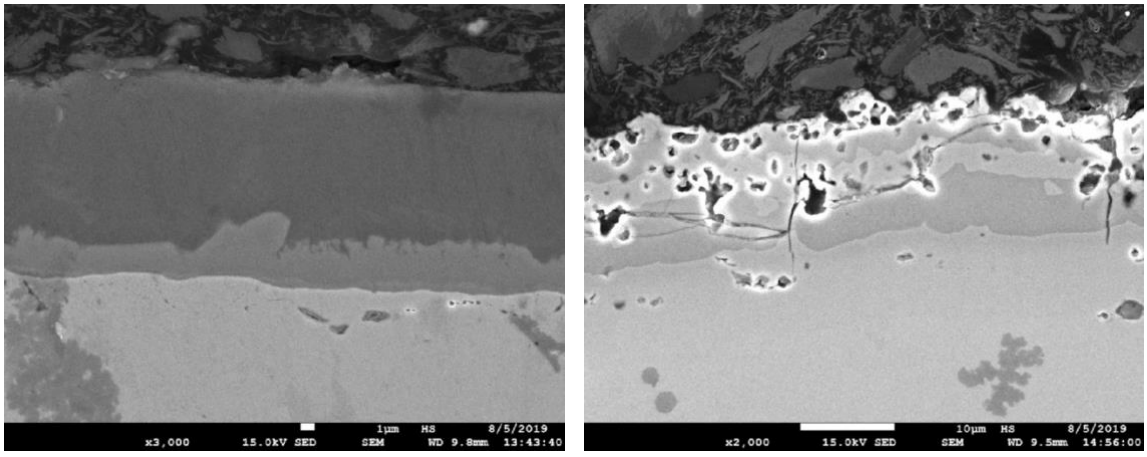

Figure 1.5. Cross-sectional SEM images of the conventional Al-Si coating after/before HDA/HPF (left), after HPF process (right). Heat-treatment conditions during HPF: 300 seconds at 930°C.

1.4. Motivation and Objectives

The applications of organic and inorganic coatings have been suggested to provent corrosion of substrate, such as aluminum or iron, that allows longer service period of such materials. Such forms of coatings have been shown a proper level of protection, but the existence of damages, either mechanical or electrochemical, have shown that such the barrier can be unexpectedly reach to its failure, that greatly decreases the lifetime of the asset.

For the organic coating, it is necessary to secure the corrosion inhibitor by its controlled release in order to extend the substrate's protection period. Compared to the direct application of corrosion inhibitor, the utilization of the nano- or micro-sized capsules has been suggested to work as the corrosion inhibitor reservoir that are only activated under a certain condition. Meanwhile, the amine-based corrosion inhibitors have been shown its superior adsorption capability that potentially combined with the nanoencapsulation technique to provide prolonged substrate protection even at the chloride-rich environment.

Meanwhile, for the inorganic coating that may contain the Al-Si coating that popularly used in the automotive field, the necessecity of the better corrosion protection coating system has been requied, due to its poor corrosion resistance that comes from the formation of pores throughout the coating matrix and the existence of microcracks that forms during quenching that originally intended for martensitic transformation of the substrate.

Thus, the objective of this study is to understand the effect of the prolonged or controlled release of corrosion inhibitor on the anti-corrosion performance, and to investigate the next generation of the inorganic coating that potentially replace the conventional Al-Si coating system for the purpose of automotive field application that contains HDA and HPF processes with high-temperature heat-treatment. This research can contribute to the effect of the modified surface either by the controlled release of the corrosion inhibitor or by the addition of extra element that along with the Al-Si coating matrix.

1.5. References

[1] T.L. Metroke, R.L. Parkhill, E.T. Knobbe, Passivation of metal alloys using sol–gel-derived materials—a review, Progress in Organic Coatings. 41 (2001) 233–238.

[2] M. Pourbaix, Atlas of electrochemical equilibria in aqueous solutions, National Association of Corrosion Engineers, 1974.

[3] J. Ning, Y. Zheng, B. Brown, D. Young, S. Nesic, A Thermodynamic Model for the Prediction of Mild Steel Corrosion Products in an Aqueous Hydrogen Sulfide Environment, Corrosion. 71 (2015) 945–960.

[4] C. Van Dinh, M. Kubouchi, An Approach for the Prediction of Blistering on Polymer–Steel Lining Systems Exposed to an Aqueous Environment, Ind. Eng. Chem. Res. 51 (2012) 11681–11687.

[5] C. Kim, L. Chen, H. Wang, H. Castaneda, Global and local parameters for characterizing and modeling external corrosion in underground coated steel pipelines: A review of critical factors, Journal of Pipeline Science and Engineering. 1 (2021) 17–35.

[6] S.K. Ghosh, Self-healing materials: fundamentals, design strategies, and applications, Wiley Online Library, 2009.

[7] A. Kumar, L.D. Stephenson, J.N. Murray, Self-healing coatings for steel, Progress in Organic Coatings. 55 (2006) 244–253.

[8] E. McCafferty, Introduction to corrosion science, Springer Science & Business Media, 2010.

[9] D. Zhu, W.J. Van Ooij, Corrosion protection of metals by water-based silane mixtures of bis-[trimethoxysilylpropyl] amine and vinyltriacetoxysilane, Progress in Organic Coatings. 49 (2004) 42–53.

[10] M. Kendig, M. Hon, L. Warren, 'Smart'corrosion inhibiting coatings, Progress in Organic Coatings. 47 (2003) 183–189.

[11] S. Sathiyanarayanan, S. Muthkrishnan, G. Venkatachari, Corrosion protection of steel by polyaniline blended coating, Electrochimica Acta. 51 (2006) 6313–6319.

[12] H. Kaesche, N. Hackerman, Corrosion inhibition by organic amines, Journal of the Electrochemical Society. 105 (1958) 191–198.

[13] T. Szauer, A. Brandt, The corrosion inhibition of iron by amines and fatty acids in neutral media, Corrosion Science. 23 (1983) 473–480.

[14] T. Szauer, A. Brandt, Adsorption of oleates of various amines on iron in acidic solution, Electrochimica Acta. 26 (1981) 1253–1256.

[15] S.-H. Yoo, Y.-W. Kim, K. Chung, N.-K. Kim, J.-S. Kim, Corrosion Inhibition Properties of Triazine Derivatives Containing Carboxylic Acid and Amine Groups in 1.0 M HCl Solution, Ind. Eng. Chem. Res. 52 (2013) 10880–10889.

[16] T. Szauer, A. Brandt, On the role of fatty acid in adsorption and corrosion inhibition of iron by amine—fatty acid salts in acidic solution, Electrochimica Acta. 26 (1981) 1257–1260.

[17] W. Shang, C. He, Y. Wen, Y. Wang, Z. Zhang, Performance evaluation of triethanolamine as corrosion inhibitor for magnesium alloy in 3.5 wt% NaCl solution, RSC Advances. 6 (2016) 113967–113980.

[18] L.B. Coelho, M. Taryba, M. Alves, X. Noirfalise, M.F. Montemor, M.-G. Olivier, The corrosion inhibition mechanisms of Ce (III) ions and triethanolamine on graphite—AA2024-T3 galvanic couples revealed by localised electrochemical techniques, Corrosion Science. 150 (2019) 207–217.

[19] V. Subramanian, W.J. van Ooij, Effect of the Amine Functional Group on Corrosion Rate of Iron Coated with Films of Organofunctional Silanes, CORROSION. 54 (1998) 204–215.

[20] J. Sinko, Challenges of chromate inhibitor pigments replacement in organic coatings, Progress in Organic Coatings. 42 (2001) 267–282.

[21] S.R. White, N.R. Sottos, P.H. Geubelle, J.S. Moore, M.R. Kessler, S.R. Sriram, E.N. Brown, S. Viswanathan, Autonomic healing of polymer composites, Nature. 409 (2001) 794–797.

[22] D.W. Fan, B.C.D. Cooman, State-of-the-Knowledge on Coating Systems for Hot Stamped Parts, Steel Research International. 83 (2012) 412–433.

[23] M.C. Galetz, C. Oskay, S. Madloch, Microstructural degradation and interdiffusion behavior of NiAl and Ge-modified NiAl coatings deposited on Alloy 602 CA, Surface and Coatings Technology. 364 (2019) 211–217.

[24] E. Billur, Hot Stamping of Ultra High-Strength Steels, Springer, 2019.

[25] L. Dosdat, J. Petitjean, T. Vietoris, O. Clauzeau, Corrosion Resistance of Different Metallic Coatings on Press-Hardened Steels for Automotive, Steel Research International. 82 (2011) 726–733.

[26] Y.-Y. Chang, C.-C. Tsaur, J.C. Rock, Microstructure studies of an aluminide coating on 9Cr-1Mo steel during high temperature oxidation, Surface and Coatings Technology. 200 (2006) 6588–6593.

[27] C. Kim, S. Cho, W. Yang, A.I. Karayan, H. Castaneda, Corrosion behavior of Al-Si-Mg coated hot-press-forming steel, Corrosion Science. 183 (2021) 109339.

2. ENCAPSULATION OF THE CORROSION INHIBITOR FOR A CONTROLLED RELEASE[*†]

In this chapter, the encapsulation of corrosion inhibitor by means of free-radical polymerization will be discussed by encapsulating one of the well-known corrosion inhibitors, triethanolamine (TEA). TEA was successfully encapsulated with a free-radical mini-emulsion polymerization technique adapted from previous studies [1–3]. On the basis of the results of transmission electron microscope (TEM), the polymerization yielded an average particle size of 450 nm. The nuclear magnetic resonance (NMR) investigated the different releasing behavior that depends on the different pH levels, which supports the corrosion inhibitor contained in the nanocapsules can undergo a controlled releasing regime to provide a prolonged barrier protection versus the corrosive electrolyte.

2.1. Introduction

[*] Part of this section is reprinted with permission from "Smart coating embedded with pH-responsive nanocapsules containing a corrosion inhibiting agent" by Changkyu Kim, Ahmad Ivan Karayan, Jose Milla, Marwa Hassan, and Homero Castaneda, 2020. *ACS Applied Materials & Interface*, 12, 6451-6459, Copyright © 2020 American Chemical Society.

[†] Part of this section is reprinted with permission from "Self-healing microcapsules as concrete aggregates for corrosion inhibition in reinforced concrete" by Homero Castaneda, Marwa Hassan, Miladin Radovic, and Jose Milla, 2018. *Transportation Consortium of South-Central States (Tran-SET)*, Project No. 17CLSU08.

Encapsulation is a process that the core material, either solid, liquid, or gas form, is enclosed by an inert shell or coating. Depending on the desired application, the core of the capsule can be loaded with the targeted chemicals or material, and the nano-sized capsules can be designed to protect the core materials based on the permeability of the shell. The activation of nanocapsules can be also varied by the target of applications, either by chemical, mechanical, or electrochemical pathways.

Conventionally, to delay the material degradation caused by corrosion, organic coating has been used to isolate the substrate from corrosive electrolytes. However, once there are unexpected defects of holidays, or the water penetrates throughout the coating layer, the substrate reacts with the corrosive electrolyte and builds up corrosion products. The corrosion products formed can be bulky and porous, which not only allows continued electrochemical reactions between electrolyte and the substrate, but also increases the area of interface between them by causing delamination or blister of the organic coating [4]. As a result, such an application of conventional coating does not provide enough barrier protection as expected, especially with the presence of unexpected damages or in terms of longer period protection.

To improve the period of protection in the conventional coating, the direct application of the corrosion inhibitor into the coating has been suggested [5–9]. However, main drawbacks of the direct application of the corrosion inhibitor into the coating were observed. First of all, in case of the low-solubility corrosion inhibitors, the amount of active inhibiting agent would not be enough to provide enough barrier protection of the

substrate. Meanwhile, if the solubility of the corrosion inhibitor is too high, the corrosion inhibitors may be consumed at an early age, even before the initiation of the corrosion of metal, which can eventually lead to less availability of active inhibiting agents to inhibit electrochemical reactions or bind the chloride at later stages [10].

Hence, the adaptation of encapsulating technique, especially encapsulating corrosion inhibitors, has been urged to address these problems by providing a controlled release of corrosion inhibitors. Specifically, this technique prevents early-period inhibitor loss by isolating the inhibiting agents within the nanocapsules and releases them only when they are needed. In this study, the effectiveness of the nanoencapsulated corrosion inhibitors, TEA, was investigated, and potential application of such technique were also discussed.

2.2. Experimental Procedure

2.2.1. Materials and Chemicals

The TEA encapsulation process required the production of a seed latex (which would attach to the TEA agent), followed by the formation of two shells and the neutralization of the seed materials with TEA. The equipment utilized in the encapsulation phase consisted of the following: a resin kettle equipped with a condenser, a nitrogen inlet, an overhead mechanical stirrer, a heating mantle with a thermocouple, and a pressure-equalizing funnel.

The seed latex was synthesized with four main monomers, namely, methyl methacrylate (MMA, ACROS Organics), methacrylic acid (MAA, ACROS Organics), butyl acrylate (BA, TCI America), and ethylene glycol dimethyl acrylate (EGDMA, BeanTown Chemical), which was used as a cross-linker to form the seed latex. These monomers were pretreated with sodium hydroxide to control their activity then subsequently dispersed in deionized (DI) water. Sodium dodecyl benzenesulfonate (SDBS, TCI America), sodium bicarbonate (ACROS Organics), and potassium persulfate (ACROS Organics) were also used as the surfactant, pH buffer, and initiator, respectively. The first shell was synthesized with MAA, BA, and MMA as the main monomers, pretreated with sodium hydroxide, and subsequently dispersed in DI water as well. The second shell was formed with styrene (ACROS Organics) as the main shell component, Triton X- 100 (ACROS Organics) as a surfactant, sodium persulfate (ACROS Organics) as the initiator, and TEA (Alfa Aesar) as the corrosion inhibitor to be encapsulated. All chemicals listed herein were used as received, with the exception of the monomers MMA, MAA, BA, and EGDMA.

2.2.2. Encapsulation of Corrosion Inhibitor

The procedure for the encapsulation of triethanolamine (TEA) was adapted from previous studies [1–3]. It involves a four-step process as schematically represented in Figure 2.1, requiring the production of the seed latex material, the formation of an

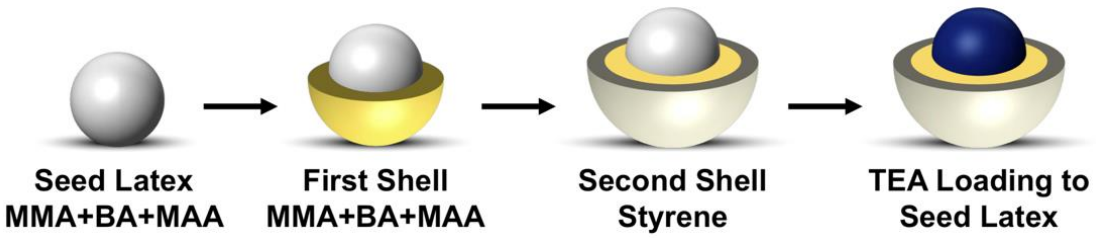

Figure 2.1. Schematic procedure of TEA encapsulation.

amphiphilic first shell, the formation of a hydrophobic second shell, and the neutralization of the seed materials with TEA (and thus loading the seed latex particles with TEA).

The method selected for the encapsulation of TEA was a free-radical polymerization micro-emulsion. Through this emulsion procedure, different parameters were changed to influence the seed latex such as the initiator and molecular weight. The equipment utilized in the development phase are the following; resin kettle equipped with condenser, a nitrogen inlet, an overhead mechanical stirrer, a heating mantle with a thermocouple, and a pressure equalizing funnel. To prevent early termination caused by airborne oxygen, the polymerization reactions were carried out in a kettle reactor under a nitrogen atmosphere.

2.2.2.1. Seed Latex

The seed latex consisted of four central monomers: methyl methacrylate (MMA), methacrylic acid (MAA), butyl acrylate (BA), and ethylene glycol dimethyl acrylate (EGDMA). The monomers were treated with sodium hydroxide in order to remove the polymerization inhibitors. This is because inhibitors were placed in monomer solutions in

order to prevent premature polymerization while shipping. MAA, BA, and MMA had a ratio of 28:9:63 with mean particle sizes of 130 nm. Using this ratio, the infusion of TEA onto the seed latex was optimized.

EGDMA monomer was used as a cross linker, potassium persulphate was used as the initiator, and sodium dodecyl benzene sulphonate (SDBS) was used as the surfactant. The SDBS surfactant and the monomers were added to a water-based solution at an elevated temperature (90 °C) and stirred at a low agitation rate. Sodium Bicarbonate was used as a buffer to prevent possible hydrolysis reactions within the solution at acidic pH levels. Sodium hydroxide was adjusted at 10% concentrations to control the activity amongst the monomers which in return increased the solid content. The potassium persulphate was used as an initiator in order to affect solid content of the resulting polymer.

Surfactants, monomers, and initiators are added to a water base solution. Micelles were formed due to the hydrophilic and hydrophobic properties of surfactants. Monomers attach to the hydrophobic tail of the micelle. The initiator reacted with the monomers and produced seed latex particles.

2.2.2.2. Shell Particles

The TEA nanocapsules contained two shell walls. The first shell was deployed for affinity increase between the hydrophilic seed latex and the hydrophobic polystyrene shell (second shell). This first shell and the ratio of the seed latex allowed for a well-regulated

fabrication of the hydrophobic polystyrene shell (second shell) with concentric shell particle morphology. The neutralization of the seed latex with triethanolamine was contingent on the balance between the first and second shell.

Before the second shell was positioned, triethanolamine must be infused onto the seed latex. The neutralization of triethanolamine helps insure the maximal inhibition efficiency. The maximal inhibitor loading efficiency in the shell phase was also aided by altering the following parameters: triethanolamine, water content, and sodium hydroxide concentration. Table 2.1 illustrates the overall procedures and related parameters chosen for the encapsulation of TEA with the double-shell structure.

Table 2.1. TEA encapsulation procedures and parameters.

Seed latex production procedures	Nanoencapsulation procedures
Phase 1 - Sodium bicarbonate (0.5g): buffer - Sodium dodecyl benzene sulphonate (0.5g): surfactant - DI water (200g) - Temperature: 90 °C - Mixing with PTFE Crescent Blade: 200 rpm	**Phase 4** - Seed latex (150g) - Potassium persulphate (0.5g): initiator - DI water (450g) - Temperature: 80 °C - Mixing with PTFE crescent blade: 200 rpm
↓	↓
Phase 2 - Methacrylic acid (MAA,10.96g): monomer - Butyl acrylate (BA,3.52g): monomer - Methyl methacrylate (MMA,24.7g): monomer - Sodium dodecyl benzene sulphonate (0.017g): surfactant - Ethylene glycol dimethyl acrylate (0.378g): cross linker - DI water (38g) - Sodium hydroxide (10% concentration)	**Phase 5** - Methacrylic acid (MAA,1.8g): monomer - Butyl acrylate (BA,4.2g): monomer - Methyl methacrylate (MMA,51g): monomer - DI water (38g) - Sodium hydroxide (10% concentration)
↓	↓

Seed latex production procedures	Nanoencapsulation procedures
Phase 3 - Potassium persulphate (0.5g): initiator - DI water (20g) - Stirring: 1 hr at 90 °C then decrease to 80 °C for phase 4	**Phase 6** - Triethanolamine (TEA,10g) - TEA releasing time: 15 minutes - Potassium persulphate (0.5g): initiator - Triton X-100 (0.33g): surfactant - Styrene (98g)

2.2.3. Materials Characterization

The synthesized nanocapsules were observed using a transmission electron microscope (TEM, JEOL 2011 high-resolution TEM). The TEA releasing behavior of the nanocapsules in different pH environments was studied by the nuclear magnetic resonance spectroscopy (NMR, Bruker 400 MHz NMR spectrometer) with triple-resonance probe (TXI). The 2g of dried nanoparticles were immersed in 100 mL of hydrochloric acid solution (pH 1.24), DI water (pH 5.87), and sodium hydroxide solution (pH 12.06), respectively, with a mild stirring for uniform solution concentration. In a total of 450 μL of solution samples that were collected at 1, 3, 5, 10, 24, 48, and 96 hrs after immersion, 50 μL of D_2O was added for a spin lock. The chemical shift was calibrated by adding 4,4-Dimethyl-4-silapentane-1-sulfonic acid (DSS). The spectra were acquired with a 90° excitation pulse with WATERGATE solvent suppression. To evaluate the concentration of TEA over time, the spectra acquired from the samples were mathematically integrated then compared to those of the pure TEA samples with a known concentration at the same pH, respectively.

2.3. Results and Discussion

2.3.1. Synthesis of Nanocapsules

The double-walled capsules containing TEA were synthesized by free-radical microemulsion polymerization. Figure 2.2 illustrates the seed- shell latex particles with no TEA, with TEA, and with TEA after separation. As shown in Figure 2.2b, the produced TEA capsules featured significant agglomerations that are undesirable for most applications. Therefore, the capsules were then added into water and dispersed at a moderate agitation rate to break up the agglomerates, as shown in Figures 2.2c and 2.2d.

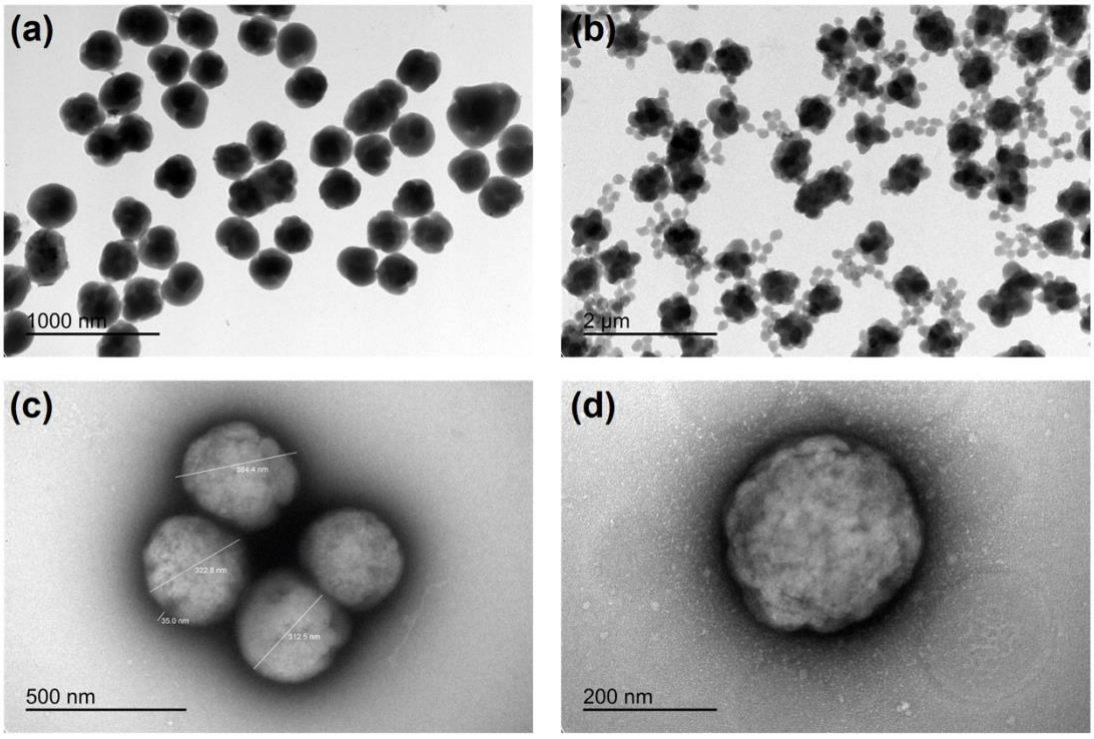

Figure 2.2. TEM *i*mage of (a) seed-shell latex particles without TEA, (b) seed-shell latex particles with TEA before separation, and (c-d) seed-shell latex particles with TEA after separation.

2.3.2. Inhibitor Releasing Behavior by NMR

The corrosion of metal, often represented by the accumulation of localized cathodic and anodic electrochemical reactions, can induce the local pH gradient that allows the release of corrosion inhibitor from the nearby nanocapsules. To investigate the different releasing behavior depends on the different pH levels, the dried nanocapsules were immersed in the solutions with different pH levels that can simulate local corrosion systems. As shown in Figure 2.3, it is observable that more of the TEA has released from either basic or acidic solution compared to the neutral solution. This is owing to the stronger ionization of the TEA that being more actively hydrolyzed at such biased pH levels rather than the neutral pH [11–13]. Meanwhile, the TEA concentration did not noticeably change over time after the early period release, indicative that the release of TEA requires the pH change of its surrounding environment.

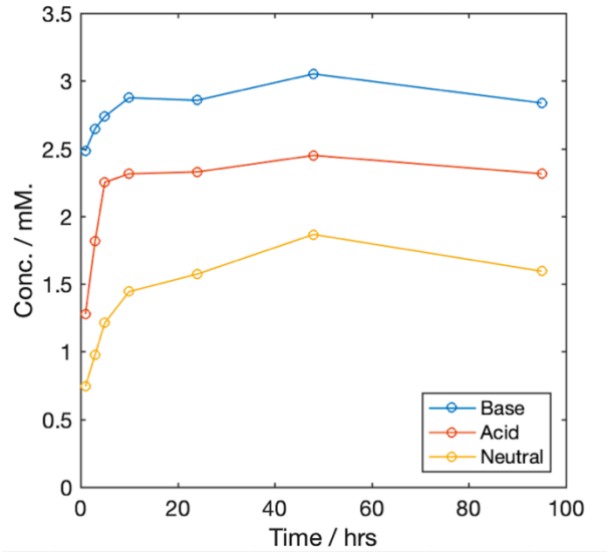

Figure 2.3. TEA releasing behavior of nanocapsules in different pH range.

2.4. Summary

This study described the encapsulation of the corrosion inhibitor, known as triethanolamine (TEA) into the double-shell structured nanocapsules. The TEA nanocapsules were successfully synthesized via a free-radical microemulsion polymerization. The mean particle size of the produced nanocapsules was 450 nm. The synthesized nanocapsules were observed to release more of TEA in both low and high pH rather than neutral pH, indicative that the corrosion reactions at the electrolyte/metal interface can induce the formation of protective layer, leading to the successful re-passivation of the exposed metal surface. These findings elucidate such technique could be successfully implemented into the corrosion field by means of providing a secondary barrier protection in addition to the role of conventional organic coatings as a primary barrier protection, by embedding them into the organic coating system.

2.5. References

[1] H. Choi, K.Y. Kim, J.M. Park, Encapsulation of aliphatic amines into nanoparticles for self-healing corrosion protection of steel sheets, Progress in Organic Coatings. 76 (2013) 1316–1324.

[2] C. Kim, A.I. Karayan, J. Milla, M. Hassan, H. Castaneda, Smart Coating Embedded with pH-Responsive Nanocapsules Containing a Corrosion Inhibiting Agent, ACS Appl. Mater. Interfaces. 12 (2020) 6451–6459.

[3] H. Castaneda, M. Hassan, M. Radovic, J. Milla, Self-Healing Microcapsules as Concrete Aggregates for Corrosion Inhibition in Reinforced Concrete, Transportation Consortium of South-Central States (Tran-SET), 2018

[4] C. Kim, L. Chen, H. Wang, H. Castaneda, Global and local parameters for characterizing and modeling external corrosion in underground coated steel pipelines: A review of critical factors, Journal of Pipeline Science and Engineering. 1 (2021) 17–35.

[5] D. Zhu, W.J. Van Ooij, Corrosion protection of metals by water-based silane mixtures of bis-[trimethoxysilylpropyl] amine and vinyltriacetoxysilane, Progress in Organic Coatings. 49 (2004) 42–53.

[6] M. Kendig, M. Hon, L. Warren, 'Smart'corrosion inhibiting coatings, Progress in Organic Coatings. 47 (2003) 183–189.

[7] S. Sathiyanarayanan, S. Muthkrishnan, G. Venkatachari, Corrosion protection of steel by polyaniline blended coating, Electrochimica Acta. 51 (2006) 6313–6319.

[8] V. Subramanian, W.J. van Ooij, Effect of the Amine Functional Group on Corrosion Rate of Iron Coated with Films of Organofunctional Silanes, CORROSION. 54 (1998) 204–215.

[9] J. Sinko, Challenges of chromate inhibitor pigments replacement in organic coatings, Progress in Organic Coatings. 42 (2001) 267–282.

[10] Y. Wang, G. Fang, W. Ding, N. Han, F. Xing, B. Dong, Self-immunity microcapsules for corrosion protection of steel bar in reinforced concrete, Sci Rep. 5 (2015) 18484.

[11] H. Choi, Y.K. Song, K.Y. Kim, J.M. Park, Encapsulation of triethanolamine as organic corrosion inhibitor into nanoparticles and its active corrosion protection for steel sheets, Surface and Coatings Technology. 206 (2012) 2354–2362.

[12] J. Mudassir, N.M. Ranjha, Dynamic and equilibrium swelling studies: crosslinked pH sensitive methyl methacrylate-co-itaconic acid (MMA-co-IA) hydrogels, Journal of Polymer Research. 15 (2008) 195–203.

[13] B.R. Saunders, H.M. Crowther, B. Vincent, Poly [(methyl methacrylate)-co-(methacrylic acid)] microgel particles: swelling control using pH, cononsolvency, and osmotic deswelling, Macromolecules. 30 (1997) 482–487.

3. SMART COATING EMBEDDED WITH PH-RESPONSIVE NANOCAPSULES CONTAINING A CORROSION INHIBITING AGENT[*]

3.1. Introduction

The corrosion of metals includes progressive material degradation that affects material integrity and ultimately leads to large economic losses [1]. One of the common approaches for the protection of metallic surfaces is the application of an organic coating that provides a barrier effect. However, such barrier protection is vulnerable to damages via mechanical impact that forms holes during its application, resulting in the exposure of the metal substrate to the environment. In addition, a coating can also lose its barrier protection when water and aggressive species diffuse into the coating and reach the metal substrate, forming corrosion products that cause delamination or blistering of the coating [2].

Alternatively, metal surfaces can be protected through the application of organic or hybrid corrosion inhibitors. In particular, amine functional groups with an aliphatic tail are known to slow the access of corrosive species, such as water molecules or active anions, by forming an adsorption-derived barrier [3]. The role of the amine as a cross-

[*] Part of this section is reprinted with permission from "Smart coating embedded with pH-responsive nanocapsules containing a corrosion inhibiting agent" by Changkyu Kim, Ahmad Ivan Karayan, Jose Milla, Marwa Hassan, and Homero Castaneda, 2020. *ACS Applied Materials & Interface*, 12, 6451-6459, Copyright © 2020 American Chemical Society.

linking agent and the effect of π-bonds have been explored, as they dominate the corrosion inhibition performance [4]. Such inhibitors are applied either indirectly through the surrounding medium at small concentrations or directly into the coating. The indirect applications of various amine-based corrosion inhibitors have been reported in acidic and neutral environments and have shown potential for their use as anodic and cathodic inhibitors [5–8]. Among them, triethanolamine (TEA) has been considerably studied because of its strong physisorption and chemical coordination with the metal substrate, which is beneficial even in acidic or chloride-rich environments [4,9,10].

The direct application of corrosion inhibitors into coatings has also been a topic of interest. An amine/silane-based coating on aluminum showed comparable barrier performance to a conventional chromate-based coating [11]. An application of polyaniline doped with an inhibitor for coating purposes has also been widely studied using a conductive coating nature that allows the release of an inhibitor by the reduction of the coating coupled to metal oxidation [12,13]. However, several drawbacks of direct inhibitor applications have been reported, such as fast inhibitor exhaustion, diminishment of barrier protection, and semipermeable film formation [14,15].

One approach to overcome the aforementioned drawbacks is by encapsulating the corrosion inhibitors. Such a technique prevents leaching of the inhibitor and allows an autonomous healing of the material by releasing the inhibitor when needed. Various capsule activation mechanisms for mechanically or electrochemically driven damages have been suggested to build a protective layer that prevents further material degradation

[16–18]. For instance, capsules may be triggered to release the inhibitor or healing agent through mechanically driven damage caused by scratches or cracking or through electrochemically driven damage caused by a local pH level change due to corrosion [19].

The inhibition efficiency and the effective prolonged time of the encapsulated corrosion inhibitor depend on several factors. The proper level of inhibitor solubility in water has been considered to be an important factor. A low solubility results in a negligible inhibiting performance, whereas a high solubility results in excessive leaching of the inhibitor that leads to a short inhibition time [16,20]. The interaction between the inhibitor and the coating matrix is another parameter to consider because it can hinder corrosion inhibition by chemical coating degradation [21]. The anticorrosion efficiency depends on the concentration of inhibitor containers, and their position in the coating matrix has also been suggested [22,23]. In addition, the effective inhibition period can be extended by a controlled release mechanism of the nanocapsules, which is influenced by their shell properties. Despite the extensive studies regarding encapsulated corrosion inhibitors, few have undergone long-term measurements [24,25]. A prolonged release of the inhibitor is highly desirable because it can provide long-term corrosion protection and increase its feasibility for practical applications. This can be achieved by adding nanocapsules into the coating that would release the inhibitor autonomously once the coating gets damaged. As such, this study evaluates the long-term performance of the coating, with and without the encapsulated TEA to determine whether the proposed technology effectively inhibits corrosion after the original protective coating has been damaged.

In the present work, the organic corrosion inhibitor, TEA, was encapsulated and added to an epoxy coating. The long-term anticorrosion performance of the coating, enabled by its self-healing property, was investigated to improve the corrosion protection of the aluminum alloy.

3.2. Experimental Procedure

3.2.1. Sample Preparation

Panels of aluminum alloy 3003- H14 (Cu 0.05−0.2, Fe < 0.7, Mn 1−1.5, Si < 0.6, Zn < 0.1, Al balance, all wt %) were obtained from Q-Lab and used for all experiments. MasterEmaco ADH 1090RS two-part epoxy (BASF) and sodium chloride (Sigma-Aldrich) were used for the coating and electrolyte, respectively. The TEA encapsulation was performed by following the procedures and related parameters shown in Table 2.1.

Prior to the coating, the aluminum substrates were ground by 400-, 800-, and 1000-grit SiC sandpapers and then cleaned and degreased by deionized water and ethanol. The substrates were then subjected to ultrasonic cleaning and subsequently air-dried. The coating was prepared by mixing 10 wt % of the synthesized nanocapsules and epoxy. The mixture was then applied on the substrate with a final coating thickness of 400 μm and cured for 24 h for initial cure and then 7 days for full cure, both at room temperature, before the electrochemical tests. An X-shaped artificial defect with a length of ∼1.2 cm and a width of ∼150 μm was produced on the coating before the coating was fully cured to prevent mechanical capsule rupture. Pure epoxy-coated samples with the same

thickness and artificial defect were prepared as controls and tested under the same conditions for comparison. Duplicates of each coating type were also prepared to assess the reproducibility of the observed results.

3.2.2. Corrosion Testing

To compare the corrosion performance, the samples were immersed in a 5 wt % sodium chloride (NaCl) solution. Electrochemical impedance spectroscopy (EIS) measure- ments were performed at the open-circuit potential (OCP) using a Gamry Reference 1000E potentiostat. A three-electrode electrochemical cell was used with the coated sample, saturated calomel electrode (SCE), and graphite as the working, reference, and counter electrodes, respectively. The measuring frequency range of the test was from 100 kHz to 10 mHz with an amplitude of 10 mV. The experimental setup used for the encapsulated TEA coating is shown in Figure 3.1. The same setup was also used for the control coating.

The scanning vibrating electrode technique (SVET, VersaScan, AMETEK), equipped with a vibrating electrode made of Pt/Ir covered with a polymer that leaves a ~10 μm tip diameter, was conducted in 1.5 mM NaOH electrolyte at 25 °C (pH ~9, conductivity ~320 μS/cm). The above weak alkaline electrolyte was selected to evaluate the workability of the smart coating even under a condition that does not allow the formation of the passive oxide layer of the substrate [26]. Samples for SVET characterization were prepared to have a coating thickness of 50 μm with the same width

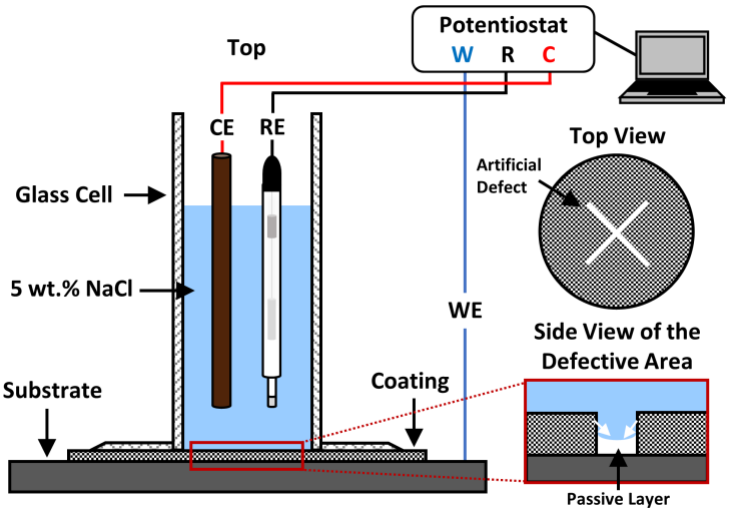

Figure 3.1. Experimental setup for corrosion testing in 5 wt % NaCl (encapsulated TEA coating).

as the artificial defect. The probe had vibration amplitudes and frequencies of 30 µm and 80 Hz, respectively, and its tip was located 100 µm from the artificial defect. The area scanned was 400 µm × 400 µm with a 10 µm/s scan speed and a 10 µm step size. All scanning processes were controlled by VersaScan software.

3.2.3. Materials Characterization

Scanning electron microscope (SEM, JEOL JCM-600 Plus) coupled to energy-dispersive X-ray spectroscopy (EDS) was used to characterize the substrate surface. The SEM visualized the artificially defective area to provide surface conditions after the corrosion testing, and the EDS revealed the elemental distribution of the defective area to investigate the effect of the inhibitors on protecting the surface. The surface of the samples

used for the corrosion testing was pretreated with a 2 nm thick Pt coating applied with a sputter coater (Cressington 208 HR) to minimize surface charging prior to SEM-EDS.

The nuclear magnetic resonance (NMR) spectra were obtained using a Bruker 400 MHz NMR spectrometer equipped with triple- resonance probes (TXI) to identify the release of TEA from the encapsulated TEA coating. The electrolyte was collected from the immersed samples with the absence and presence of encapsulated TEA, respectively, after the 60 days of corrosion testing. Pure TEA solution was also prepared for comparison. In a total of 450 μL of obtained solution samples, 50 μL of D2O was added for the spin lock. 4,4-Dimethyl-4-silapentane-1-sulfonic acid (DSS) was also added for the chemical shift calibration. All spectra were acquired using a 90° excitation pulse with WATERGATE solvent suppression. To confirm the existence of TEA, the spectra obtained from the samples after 60 days of corrosion testing were matched with the pure TEA solution.

3.3. Results and Discussion

3.3.1. EIS Study in 5 wt % NaCl Solution

To obtain information about the changes in surface properties and estimate the effect of the inhibitor-loaded nanocapsules, EIS investigations for different coatings were performed in a 5 wt % NaCl solution. Such electrolyte concentration was chosen to accelerate the initiation of the corrosion regime and to investigate the inhibition efficiency of the embedded capsules triggered by the corrosion reaction of the substrate. Figures 3.2

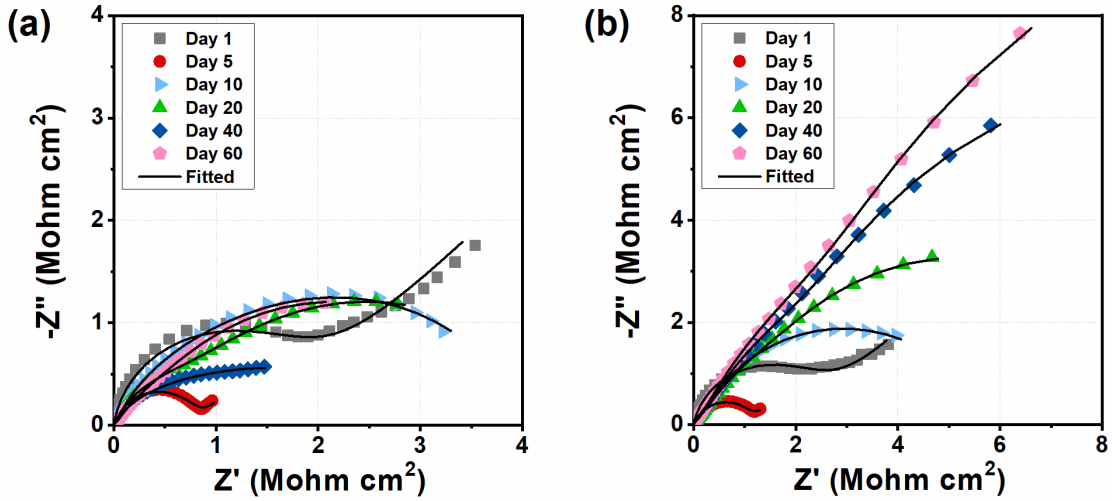

Figure 3.2. Nyquist plots for the corrosion of aluminum alloy 3003 in 5 wt % NaCl with the (a) absence and (b) presence of encapsulated TEA.

and 3.3 show Nyquist plots and Bode-phase angle plots measured over 60 days, respectively.

Figure 3.2a,b shows the Nyquist plots for a control and an encapsulated TEA coating, respectively. As shown in these figures, a diffusion regime was evidenced by a straight line in the low-frequency (LF) range due to the diffusion of corrosion reactants or products [27] and was observed until the fifth day of immersion for both samples. The depressed semicircle prior to the straight line was attributed to the contribution of coating and the charge transfer through the double layer [28]. Over the experimental period of the control sample, shown in Figure 3.2a, the diffusion regime was replaced by the formation of the corrosion product layer, which was observed in the LF range, followed by a charge-transfer phenomenon. The diameter of the depressed semicircle either increases or decreases within a similar range over time by the accumulation of repeated water

penetration of the corrosion product layer, respectively. Such a trend suggests that the corrosion product layer did not provide a sufficient barrier effect to protect the substrate.

Meanwhile, in Figure 3.2b, for the encapsulated TEA sample, the diffusion regime also disappeared after day 5. However, there was a noticeable increase in the semicircle diameter with a raised shape from day 5 to day 60, suggesting a considerable growth of impedance magnitudes. Such results indicate that active corrosion in the early immersion period triggered the release of corrosion inhibitors to slow the factors that contribute to active corrosion, for example, charge transfer and diffusion. The signature clearly demonstrates the formation of the inhibiting layer that contributed to the enhanced anticorrosion performance.

For both cases, the effect of the diffusion process shown as the straight line at LF in the early period was diluted after day 5, which means that the film, either an oxide or inhibiting layer, and charge-transfer resistance play dominant roles in the corrosion of the metal surface [29,30].

The Bode plots of the control and encapsulated TEA coating during 60 days of testing are presented in Figure 3.3a,b, respectively. Until day 5, both samples revealed two time constants (TCs) with Warburg impedance, and the TCs can be assigned to the contribution of the coating and the charge transfer. After the initial period, both samples experienced a transition to introduce another TC in the LF range, representing either an oxide or an inhibiting layer. The sample with the presence of encapsulated TEA revealed a gradual increase in the phase angle throughout the mid- to low- frequency range. In

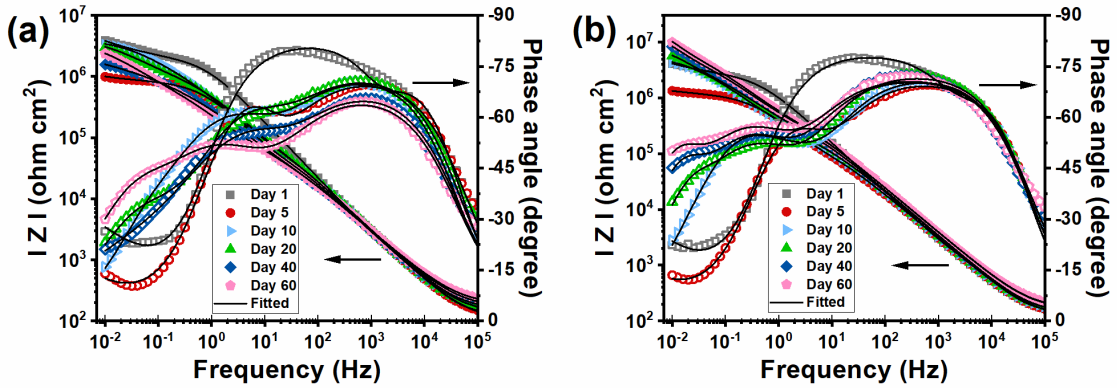

Figure 3.3. Bode phase angle plots for the corrosion of aluminum alloy 3003 in 5 wt % NaCl with the (a) absence and (b) presence of encapsulated TEA.

particular, the phase angle change from 15° (day 5) to 50° (day 60) at the lowest frequency indicated a transition from resistive to semi-capacitive behavior by the effective adsorption of the inhibitor. Similarly, a considerable increase in the LF impedance modulus (|Z|), which is attributed to the presence of the nanocapsules, was also observed, whereas that of the control sample was maintained at a lower level compared with its value on day 1.

Two equivalent circuit (EC) models are proposed in Figure 3.4 to provide a quantitative analysis by representing effective parameters of the impedance spectra in the absence and presence of the nanocapsules. The impedance spectra that included the Warburg impedance were fitted with the EC shown in Figure 3.4a to represent the system until day 5, and the others were fitted with the EC, shown in Figure 3.4b, for the remainder of the testing period [28,31]. The ECs were composed of numerous elements, namely, the solution resistance (R_s), pore resistance (R_c), oxide layer or inhibiting layer resistance (R_f),

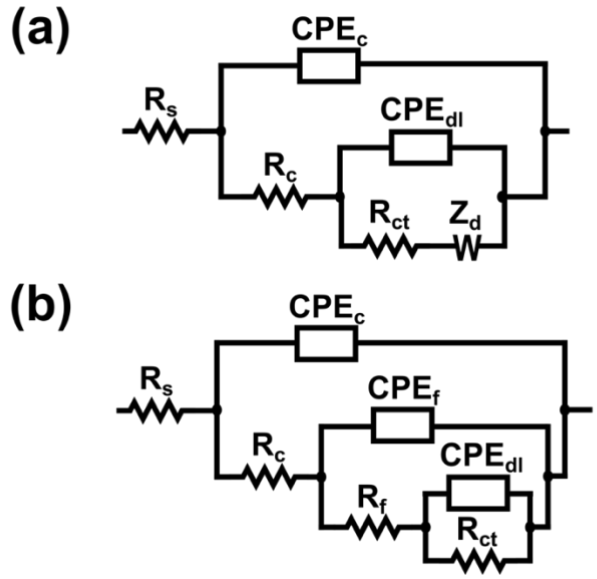

Figure 3.4. Schematic representation of the corresponding equivalent circuits used for fitting the experimental EIS results (a) until day 5 and (b) after day 5.

charge-transfer resistance (R_{ct}), capacitance in terms of the constant phase element (CPE), coating capacitance (C_c), oxide layer or inhibiting layer capacitance (C_f), double-layer capacitance (C_{dl}), and Warburg impedance (Z_D) for ionic diffusion.

A CPE concept was used to represent the depressed impedance loops, which occurred from distributions of the physical properties that result in the distribution of the time constants [32]. The capacitance deduced from the CPE concept is described as follows [33]:

$$C = Y_0(\omega''_{max})^{n-1} \tag{3.1}$$

where Y_0 and $0 < n \leq 1$ are the model parameters, and ω''_{max} is the frequency at the maximum imaginary impedance, Z''.

The inhibition efficiency of the inhibitors was calculated from the polarization resistance, $R_p = R_f + R_{ct}$, using the following equation:

$$\eta(\%) = \frac{R_p - R_{p,0}}{R_p} \times 100 \quad (3.2)$$

where R_p and $R_{p,0}$ represent the polarization resistance in the presence and absence of the nanocapsules, respectively.

The impedance parameters obtained from the ECs are listed in Table 3.1. Up until day 5, the decreasing R_{ct} value for both samples was attributed to the increasing charge-transfer phenomena, which resulted in the dissolution of the substrate by having active sites on its surface. However, after day 5, both R_f and R_{ct} values started to increase in the presence of the nanocapsules until the end of the experimental period. This can be caused by the increased adsorption of the inhibitor, which provides a sufficient level of barrier protection and results in the recovery of the R_{ct} by blocking corrosive ionic or molecular species.

The capacitance of the coating layer, C_c, and the produced film layer, C_f, imply the level of water uptake that is critical for the metal protection [34]. From the initiation of the corrosion, after day 5, the capacitance of the inhibiting layer of the encapsulated TEA sample was gradually decreased, which indicated that there was a packed adsorption of the inhibitors that formed an inhibiting layer that prevented further water penetration.

Table 3.1. Impedance parameters for the corrosion of aluminum alloy 3003 in 5 wt % NaCl.

Time (day)	R_c ($\Omega\, cm^2$)	C_c ($F\, cm^{-2}\, s^{n-1}$)	n_c	R_f ($\Omega\, cm^2$)	C_f ($F\, cm^{-2}\, s^{n-1}$)	n_f	R_{ct} ($\Omega\, cm^2$)	C_{dl} ($F\, cm^{-2}\, s^{n-1}$)	n_{dl}	W ($\Omega\, cm^2\, s^{-1/2}$)	R_p ($\Omega\, cm^2$)	η (%)
Control Coating												
1	7.28×10^3	1.08×10^{-7}	0.893	-	-	-	1.83×10^6	2.03×10^{-8}	0.978	4.30×10^5	1.83×10^6	-
5	1.21×10^5	3.09×10^{-7}	0.803	-	-	-	6.97×10^5	1.05×10^{-7}	0.966	4.70×10^4	6.97×10^5	-
10	1.35×10^5	2.63×10^{-7}	0.813	2.22×10^6	2.62×10^{-7}	0.733	1.70×10^6	1.29×10^{-6}	0.753	-	3.92×10^6	-
20	1.34×10^5	2.57×10^{-7}	0.815	1.85×10^6	1.73×10^{-7}	0.611	2.46×10^6	1.97×10^{-6}	0.782	-	4.31×10^6	-
40	8.19×10^4	4.07×10^{-7}	0.769	8.12×10^5	3.42×10^{-7}	0.743	2.28×10^6	2.55×10^{-6}	0.463	-	3.09×10^6	-
60	7.14×10^4	4.20×10^{-7}	0.762	1.61×10^6	8.43×10^{-7}	0.633	2.60×10^6	1.18×10^{-6}	0.691	-	4.21×10^6	-
Encapsulated TEA Coating												
1	5.49×10^3	1.23×10^{-7}	0.877	-	-	-	2.48×10^6	4.28×10^{-8}	0.887	3.76×10^5	2.48×10^6	-
5	2.03×10^5	3.09×10^{-7}	0.797	-	-	-	9.42×10^5	2.45×10^{-7}	0.872	5.43×10^4	9.42×10^5	-
10	2.32×10^5	2.56×10^{-7}	0.808	3.60×10^6	5.17×10^{-7}	0.708	1.97×10^6	1.76×10^{-7}	1	-	5.57×10^6	29.8
20	3.81×10^5	2.34×10^{-7}	0.815	5.61×10^6	4.99×10^{-7}	0.700	4.02×10^6	1.75×10^{-6}	1	-	9.63×10^6	55.3
40	5.75×10^5	2.33×10^{-7}	0.807	7.60×10^6	3.49×10^{-7}	0.737	1.13×10^7	1.13×10^{-6}	1	-	1.89×10^7	83.7
60	6.35×10^5	2.32×10^{-7}	0.802	1.05×10^7	2.92×10^{-7}	0.733	1.91×10^7	8.24×10^{-7}	1	-	2.97×10^7	85.8

Meanwhile, in the control sample, there were only small changes in the R_f and R_{ct} values after day 5, which can be caused by an accumulation of permeable corrosion products that allow active corrosion throughout the entire experimental period. In addition, the evolution of the oxide layer capacitance over time could also be attributed to the formation of a porous layer made from corrosion products, which allowed a continuous water supply that led to a sequential metal dissolution. Such an increase in the oxide layer capacitance suggests that this layer continuously allowed water uptake and was unable to provide a satisfactory barrier protection.

As a result, the change in the impedance parameters in the presence of the nanocapsules showed a clear trend that suggests enhanced anticorrosive properties driven by the formation of the inhibiting layer, as shown in Figure 3.5. The inhibition efficiency, η, increased as the Rp value increased, whereas the $R_{p,0}$ value was maintained at a similar level. An inhibition efficiency >85% was achieved on day 60, demonstrating that the encapsulated TEA coating provided an effective protection to prevent the corrosion of aluminum, even over an extended experimental period.

3.3.2. Corrosion Inhibition Action by SVET Analysis in an Alkaline Environment

The localized cathodic and anodic reactions on the artificially defective area of the control and encapsulated TEA coating in 1.5 mM NaOH solution (pH ~9, conductivity ~ 320 μS/cm) were studied using SVET analysis, as shown in Figure 3.6. The above electrolyte enabled an environment in which the aluminum alloy actively corrodes in the

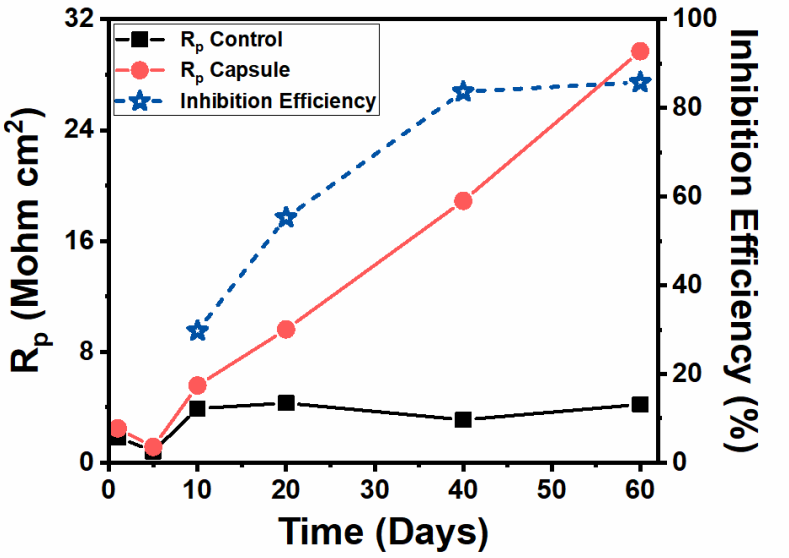

Figure 3.5. Polarization resistance (R_p) and inhibition efficiency (η) obtained by fitting the EIS spectra.

absence of a native passive film. As such, this allowed the examination of the anticorrosion performance of the encapsulated TEA coating. The control sample showed vigorous charge-transfer reactions represented by the high current density shown in Figure 3.6a, whereas a greatly decreased corrosion attack was observed in the coating with encapsulated TEA according to Figure 3.6b. Such suppression of the corrosion attack under the accelerated environmental condition indicated that the embedded nanocapsules can help delay the material degradation process, which is in agreement with the previously shown results.

3.3.3. Surface Examination with an Optical Microscope

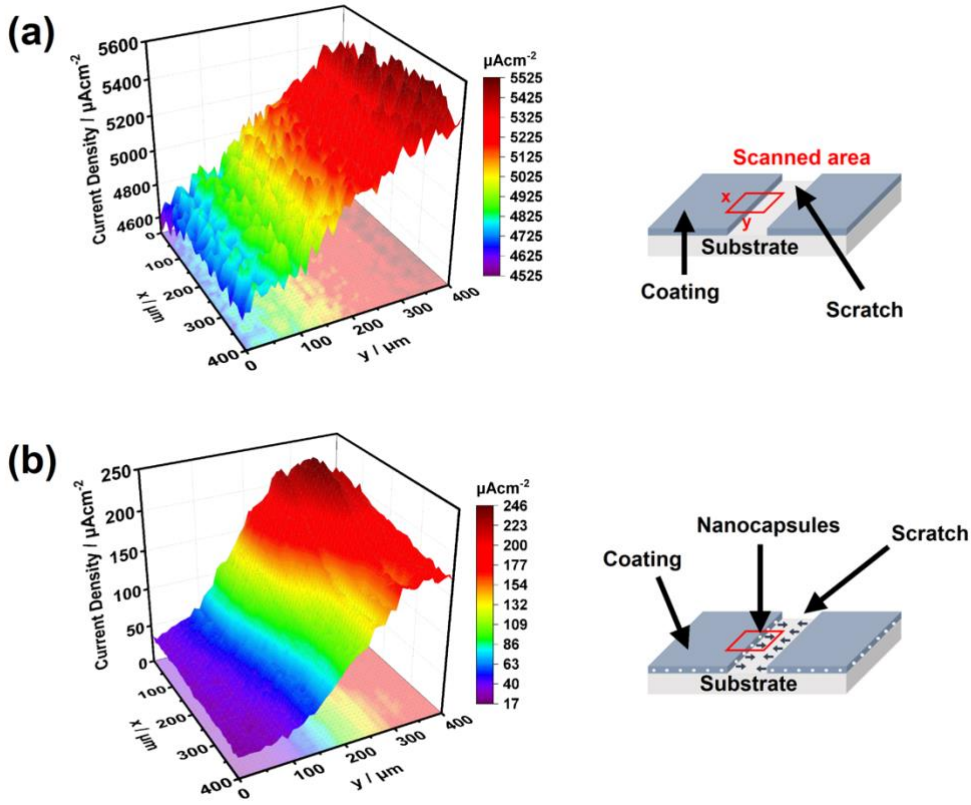

Figure 3.6. SVET current density maps of the scanned area after a 3 h immersion in 1.5 mM NaOH with the (a) absence and (b) presence of encapsulated TEA.

The optical microscope images shown in Figure 3.7 revealed the condition of the artificial defects before and after 60 days of immersion testing for the control (a and b) and the encapsulated TEA coating (c and d). In Figure 3.7a,b, a black corrosion product was observed that covered a considerable area of the control sample. Meanwhile, in the presence of the encapsulated TEA coating, an effective corrosion protection was observed, as its surface remained relatively unstained after 60 days of testing, as shown in Figure 3.7c,d. This well-preserved surface suggests that an inhibiting layer was formed on the metal substrate.

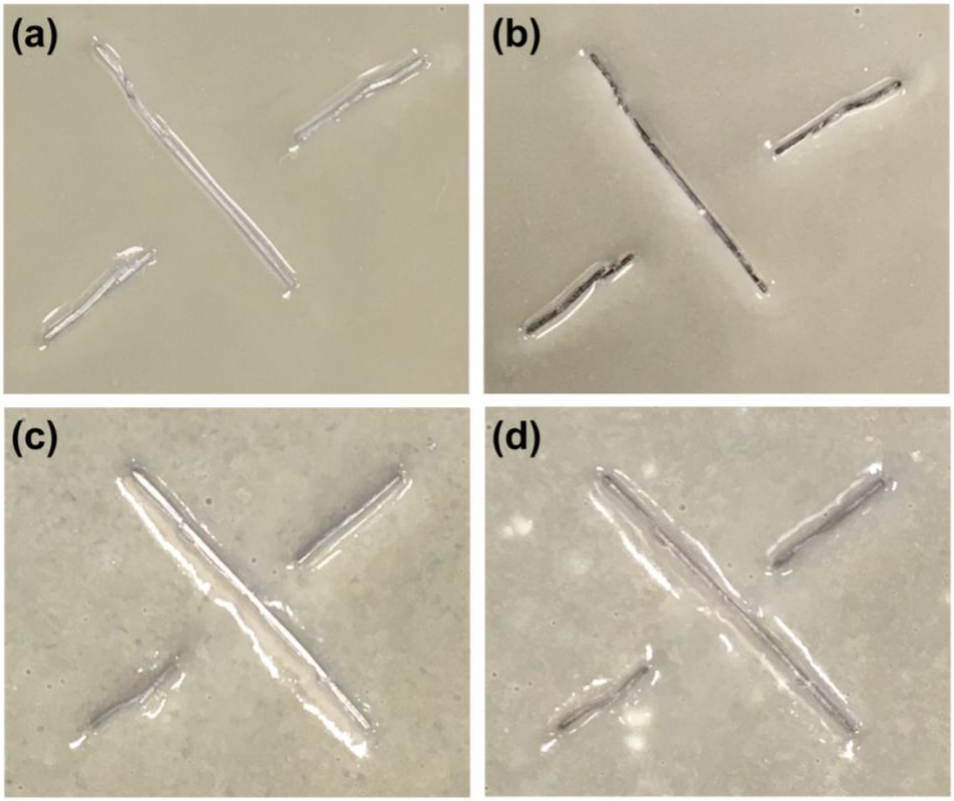

Figure 3.7. Optical microscope images of the control (a → b) and encapsulated TEA (c → d) coating before and after 60 days of corrosion testing in 5 wt % NaCl.

3.3.4. Surface and Elemental Analysis by SEM-EDS

Figure 3.8 shows the SEM images and EDS analysis results, which reveals surface morphologies and compositions, respectively, after 60 days of immersion testing in a 5 wt % NaCl solution. In the absence of the nanocapsules, Figure 3.8a,c depicts a severely degraded metal surface caused by a corrosive environment. The lack of surface protection enabled the formation of crack-shaped corrosion products, which were revealed to have a considerable amount of oxygen by EDS analysis. Such a high oxygen amount may indicate

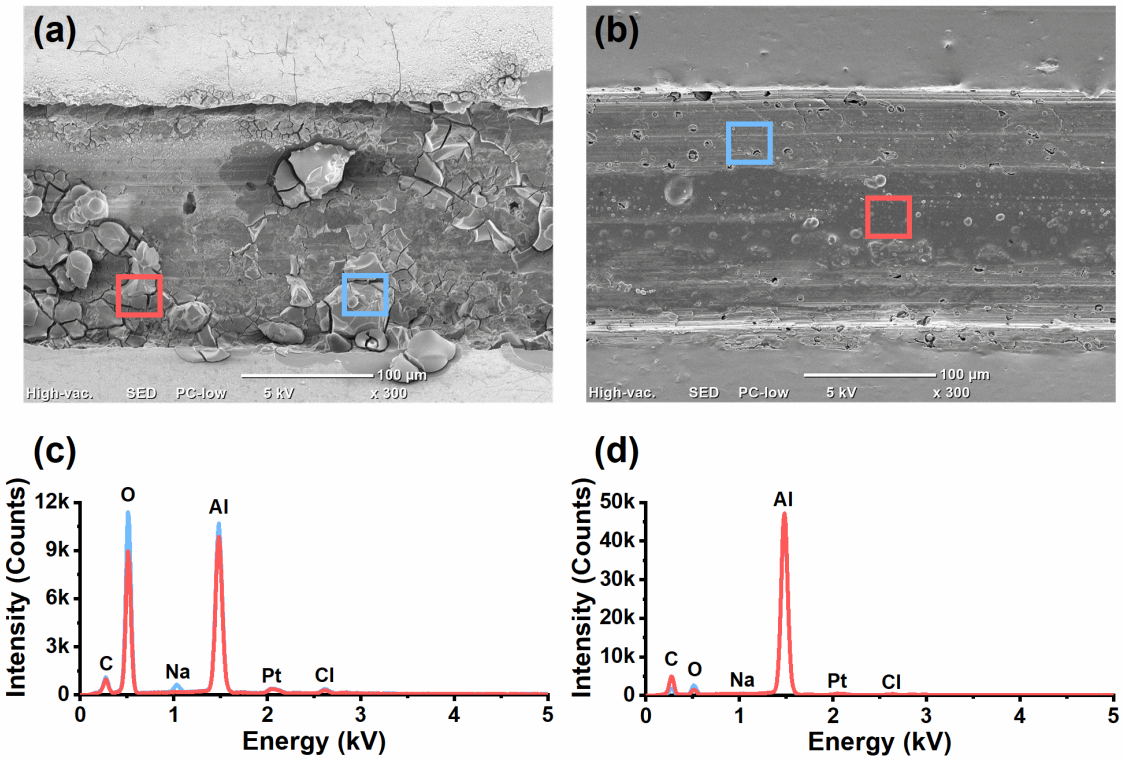

Figure 3.8. SEM-EDS analysis of the artificially defective area with the (a and c) absence and (b and d) presence of encapsulated TEA after 60 days of corrosion testing in 5 wt % NaCl.

the presence of aluminum corrosion products, which could correspond to Al_2O_3 or $Al(OH)_3$. Among the various aluminum-driven corrosion products, $Al(OH)_3$ has been reported to reveal a black color [35], which is in good agreement with the optical microscope observation shown in Figure 3.7b. Additionally, the $Al(OH)_3$ is known to form a porous structure [36], thus the formation of $Al(OH)_3$ could not densely cover the exposed area and therefore cannot provide an adequate barrier protection to the exposed area. Such insufficient protection allowed a continuous water supply that caused considerable metal dissolution that finally resulted in the growth of corrosion products.

In the presence of the nanocapsules, shown in Figure 3.8b,d, the metal surface was relatively less degraded without any distinct block of corrosion products. Only mild corrosion was observed at the edge of the marked area during the early testing period. However, the initiation of such corrosion triggered the release of TEA from the nanocapsules to form an inhibiting layer, preventing more severe corrosion from occurring. The adsorption of the TEA on the metal surface formed a dense inhibiting layer that significantly covered the exposed area, thereby limiting the water supply, which is needed for the continuous corrosion reaction to proceed, and preventing the metal dissolution, and the formation of an oxide layer could be prevented. Additionally, the EDS analysis showed a significantly lower oxygen content compared with the aluminum content, which evidenced that the corrosion attack was restricted and limited to form aluminum corrosion products. Such results are in accordance with the EIS results in Figures 3.2b and 3.3b and Table 3.1, which showed considerably enhanced impedance values and phase shifts toward semi- capacitive behavior.

3.3.5. Electrolyte Analysis by NMR

The obtained NMR spectra after 60 days of corrosion testing in a 5 wt % NaCl solution are shown in Figure 3.9. Compared with the pure TEA solution, only the electrolyte obtained from the encapsulated TEA coating sample showed the two triplets at chemical shifts of 3.0 and 3.8 ppm ^{1}H NMR spectra, respectively, which are matched with the spectrum of pure TEA. This observation indicates that the TEA was successfully

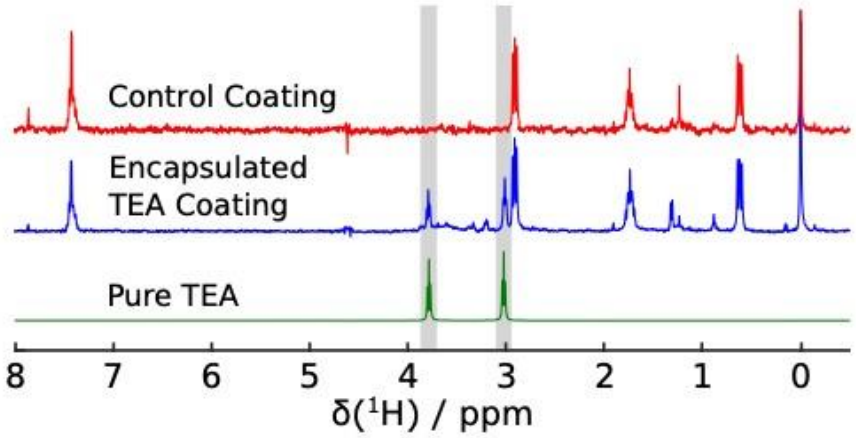

Figure 3.9. ^{1}H-NMR spectra of electrolyte after 60 days of corrosion testing from (top) control coating, (mid) encapsulated TEA coating, and (bottom) pure TEA for comparison. The gray shaded boxes indicate the chemical shifts of TEA. The chemical shifts of 0 and 4.7 represent DSS for calibration and suppressed water, respectively.

released over the testing period, accelerated by the varied pH distribution along the artificially defective area. Meanwhile, there are other noticeable chemical shifts within the encapsulated TEA sample matched with those of the control coating sample, indicating that they originated from the coating components that may have partially dissolved in solutions during the extended immersion period.

3.4. Summary

This study described the application of a self-healing-based anticorrosive coating for the long-term protection of an aluminum alloy through an encapsulated amine-based inhibitor, TEA. The TEA nanocapsules were successfully synthesized via a free-radical microemulsion polymerization and subsequently embedded into the coating system. After

corrosion was initiated on the artificially defective area during the early period of immersion, the EIS results showed that the encapsulated TEA coating system successfully released the TEA when the local pH level changed to help with the formation of an inhibiting layer throughout the experimental period. The significant increase in impedance parameters observed after the initial period indicated the successful repassivation of the metal surface, resulting in an inhibition efficiency >85%. According to the SVET measurements performed in a weak-base environment, the current density of the metal substrate with the presence of the encapsulated TEA coating was considerably lower than that of the control coating that had no TEA nanocapsules. The aforementioned results demonstrated a successful corrosion inhibition even without the native protective oxide layer of aluminum. Furthermore, such results were evidenced by surface character- ization techniques using SEM and EDS, which showed a relatively well-protected metal surface with a lower oxygen content, denoting that the metal oxidization process was slowed by the inhibiting effect of the encapsulated TEA. In addition, the NMR spectra demonstrated that the encapsulated TEA coating successfully released the TEA during the prolonged period of corrosion testing. In contrast, the higher oxygen concentration measured in the control coating, indicative of $Al(OH)_3$, could be attributed to the active corrosion process in the absence of a proper barrier.

Such noticeable suppression of corrosion activity was observed only from the sample with embedded nanocapsules, and it verified that it can provide long-term anticorrosion performance, especially in a chloride-rich environment.

3.5. References

[1] T.L. Metroke, R.L. Parkhill, E.T. Knobbe, Passivation of metal alloys using sol–gel-derived materials—a review, Progress in Organic Coatings. 41 (2001) 233–238.

[2] C. Van Dinh, M. Kubouchi, An Approach for the Prediction of Blistering on Polymer–Steel Lining Systems Exposed to an Aqueous Environment, Ind. Eng. Chem. Res. 51 (2012) 11681–11687.

[3] E. McCafferty, Introduction to corrosion science, Springer Science & Business Media, 2010.

[4] T. Szauer, A. Brandt, On the role of fatty acid in adsorption and corrosion inhibition of iron by amine—fatty acid salts in acidic solution, Electrochimica Acta. 26 (1981) 1257–1260.

[5] H. Kaesche, N. Hackerman, Corrosion inhibition by organic amines, Journal of the Electrochemical Society. 105 (1958) 191–198.

[6] T. Szauer, A. Brandt, The corrosion inhibition of iron by amines and fatty acids in neutral media, Corrosion Science. 23 (1983) 473–480.

[7] T. Szauer, A. Brandt, Adsorption of oleates of various amines on iron in acidic solution, Electrochimica Acta. 26 (1981) 1253–1256.

[8] S.-H. Yoo, Y.-W. Kim, K. Chung, N.-K. Kim, J.-S. Kim, Corrosion Inhibition Properties of Triazine Derivatives Containing Carboxylic Acid and Amine Groups in 1.0 M HCl Solution, Ind. Eng. Chem. Res. 52 (2013) 10880–10889.

[9] W. Shang, C. He, Y. Wen, Y. Wang, Z. Zhang, Performance evaluation of triethanolamine as corrosion inhibitor for magnesium alloy in 3.5 wt% NaCl solution, RSC Advances. 6 (2016) 113967–113980.

[10] L.B. Coelho, M. Taryba, M. Alves, X. Noirfalise, M.F. Montemor, M.-G. Olivier, The corrosion inhibition mechanisms of Ce (III) ions and triethanolamine on graphite—AA2024-T3 galvanic couples revealed by localised electrochemical techniques, Corrosion Science. 150 (2019) 207–217.

[11] D. Zhu, W.J. Van Ooij, Corrosion protection of metals by water-based silane mixtures of bis-[trimethoxysilylpropyl] amine and vinyltriacetoxysilane, Progress in Organic Coatings. 49 (2004) 42–53.

[12] M. Kendig, M. Hon, L. Warren, 'Smart'corrosion inhibiting coatings, Progress in Organic Coatings. 47 (2003) 183–189.

[13] S. Sathiyanarayanan, S. Muthkrishnan, G. Venkatachari, Corrosion protection of steel by polyaniline blended coating, Electrochimica Acta. 51 (2006) 6313–6319.

[14] V. Subramanian, W.J. van Ooij, Effect of the Amine Functional Group on Corrosion Rate of Iron Coated with Films of Organofunctional Silanes, CORROSION. 54 (1998) 204–215.

[15] J. Sinko, Challenges of chromate inhibitor pigments replacement in organic coatings, Progress in Organic Coatings. 42 (2001) 267–282.

[16] S.K. Ghosh, Self-healing materials: fundamentals, design strategies, and applications, Wiley Online Library, 2009.

[17] A. Kumar, L.D. Stephenson, J.N. Murray, Self-healing coatings for steel, Progress in Organic Coatings. 55 (2006) 244–253.

[18] S.H. Cho, S.R. White, P.V. Braun, Self-Healing Polymer Coatings, Advanced Materials. 21 (2009) 645–649.

[19] Z. Szklarska-Smialowska, Pitting corrosion of aluminum, Corrosion Science. 41 (1999) 1743–1767.

[20] H. Choi, Y.K. Song, K.Y. Kim, J.M. Park, Encapsulation of triethanolamine as organic corrosion inhibitor into nanoparticles and its active corrosion protection for steel sheets, Surface and Coatings Technology. 206 (2012) 2354–2362.

[21] M.L. Zheludkevich, J. Tedim, M.G.S. Ferreira, “Smart” coatings for active corrosion protection based on multi-functional micro and nanocontainers, Electrochimica Acta. 82 (2012) 314–323.

[22] D. Borisova, H. Möhwald, D.G. Shchukin, Influence of embedded nanocontainers on the efficiency of active anticorrosive coatings for aluminum alloys part I: influence of nanocontainer concentration, ACS Applied Materials & Interfaces. 4 (2012) 2931–2939.

[23] D. Borisova, H. Möhwald, D.G. Shchukin, Influence of Embedded Nanocontainers on the Efficiency of Active Anticorrosive Coatings for Aluminum Alloys Part II: Influence of Nanocontainer Position, ACS Appl. Mater. Interfaces. 5 (2013) 80–87.

[24] E.D. Mekeridis, I.A. Kartsonakis, G.C. Kordas, Multilayer organic–inorganic coating incorporating TiO2 nanocontainers loaded with inhibitors for corrosion protection of AA2024-T3, Progress in Organic Coatings. 73 (2012) 142–148.

[25] I.A. Kartsonakis, E. Athanasopoulou, D. Snihirova, B. Martins, M.A. Koklioti, M.F. Montemor, G. Kordas, C.A. Charitidis, Multifunctional epoxy coatings combining a mixture of traps and inhibitor loaded nanocontainers for corrosion protection of AA2024-T3, Corrosion Science. 85 (2014) 147–159.

[26] M. Pourbaix, Atlas of electrochemical equilibria in aqueous solutions, National Association of Corrosion Engineers, 1974.

[27] L. Niu, Y.F. Cheng, Electrochemical characterization of metastable pitting of 3003 aluminum alloy in ethylene glycol–water solution, J Mater Sci. 42 (2007) 8613–8617.

[28] J.A. Gonzalez, E. Otero, A. Bautista, E. Almeida, M. Morcillo, Use of electrochemical impedance spectroscopy for studying corrosion at overlapped joints, Progress in Organic Coatings. 33 (1998) 61–67.

[29] J.-H. Chen, Z.-C. Lin, S. Chen, L.-H. Nie, S.-Z. Yao, An XPS and BAW sensor study of the structure and real-time growth behaviour of a complex surface film on copper in sodium chloride solutions (pH= 9), containing a low concentration of benzotriazole, Electrochimica Acta. 43 (1998) 265–274.

[30] Y. Qiang, S. Zhang, S. Yan, X. Zou, S. Chen, Three indazole derivatives as corrosion inhibitors of copper in a neutral chloride solution, Corrosion Science. 126 (2017) 295–304.

[31] S.V. Lamaka, M.L. Zheludkevich, K.A. Yasakau, R. Serra, S.K. Poznyak, M.G.S. Ferreira, Nanoporous titania interlayer as reservoir of corrosion inhibitors for coatings with self-healing ability, Progress in Organic Coatings. 58 (2007) 127–135.

[32] B. Hirschorn, M.E. Orazem, B. Tribollet, V. Vivier, I. Frateur, M. Musiani, Constant-Phase-Element Behavior Caused by Resistivity Distributions in Films I. Theory, J. Electrochem. Soc. 157 (2010) C452–C457.

[33] C.H. Hsu, F. Mansfeld, Concerning the conversion of the constant phase element parameter Y0 into a capacitance, Corrosion. 57 (2001) 747–748.

[34] A.S. Nguyen, N. Causse, M. Musiani, M.E. Orazem, N. Pébère, B. Tribollet, V. Vivier, Determination of water uptake in organic coatings deposited on 2024 aluminium alloy: Comparison between impedance measurements and gravimetry, Progress in Organic Coatings. 112 (2017) 93–100.

[35] I.O. Wallinder, W. He, P.-E. Augustsson, C. Leygraf, Characterization of black rust staining of unpassivated 55% Al–Zn alloy coatings. Effect of temperature, pH and wet storage, Corrosion Science. 41 (1999) 2229–2249.

[36] R. Salomão, L. Fernandes, Porous co-continuous mullite structures obtained from sintered aluminum hydroxide and synthetic amorphous silica, Journal of the European Ceramic Society. 37 (2017) 2849–2856.

4. ELECTROCHEMICAL EVALUATION OF EPOXY-COATED-REBAR CONTAINING PH-RESPONSIVE NANOCAPSULES IN SIMULATED CARBONATED CONCRETE PORE SOLUTION[*]

In this chapter, an enhanced corrosion performance of an epoxy coated rebar (ECR) embedded with the nanocapsules containing triethanolamine (TEA) as the corrosion inhibitor will be discussed. Electrochemical corrosion tests were performed and indicated a successful protection of the artificially defected area from the sample with encapsulated TEA coating, especially in the initial immersion period, indicating that there was a successful release of TEA from the embedded nanocapsules. A considerably lower surface current density of the encapsulated TEA coating also indicated that the electrochemical reactions were delayed which were further confirmed by surface micrographs that revealed a relatively less degraded artificial defect of the sample with the encapsulated TEA coating. The corrosion product analysis denoted that the inhibiting action has delayed the further oxidation of the exposed surface by having an enhanced barrier protection that helped to maintain a lower O/Fe ratio.

4.1. Introduction

[*] Part of this section is reprinted with permission from "Electrochemical evaluation of epoxy-coated-rebar containing pH-responsive nanocapsules in simulated carbonated concrete pore solution" by Changkyu Kim, Reece Goldsberry, Ahmad Ivan Karayan, Jose Milla, Luke Goehring, Marwa Hassan, and Homero Castaneda, 2021. *Progress in Organic Coatings*, 183, 106549 Copyright © 2021 by Elsevier Ltd.

The degradation of reinforced concrete structures due to corrosion of the reinforcing steel has been considered as one of the major concerns for both new and existing structures. A recent cost-of corrosion study performed by Federal Highway Administration has estimated the annual cost caused by the corrosion issues of the US bridges to be approximately $30 Billion, not including indirect costs incurred by the traveling public due to infrastructural closures [1].

In the fresh concrete, a passive layer is well-formed on the reinforcing steel attributing to the concrete's high alkalinity [2]. However, over the service period, the corrosion of reinforcing steel can be initiated by either carbonation or a build-up of chloride ions at the rebar/concrete interface [3]. Carbonation lowers the local pH within the cementitious matrix from 12.5 to 8.5, due to the reaction between CO_2 and the pore solution that forms carbonates (CO_3^{2-}) and bicarbonates (HCO_3^-) [2]. Meanwhile, the build-up of chloride ions can also trigger corrosion by breaking the passive layer through chloride absorption [4]. Once the breakdown of the passive layer occurs either by acidification/carbonation or chloride accumulation, the corrosion regime initiates with following representative reactions [5,6].

$$\text{Anode :} \quad 2\,Fe\,(s) \rightarrow 2\,Fe^{2+}\,(aq) + 4\,e^- \tag{4.1}$$

$$\text{Cathode :} \quad 2\,H_2O\,(l) + O_2\,(g) + 4\,e^- \rightarrow 4\,OH^-\,(aq) \tag{4.2}$$

$$\text{Overall :} \quad 2\,Fe\,(s) + 2\,H_2O\,(l) + O_2\,(g) \rightarrow 2\,Fe^{2+}\,(aq) + 4\,OH^-\,(aq) \tag{4.3}$$

Epoxy-coated rebar (ECR) has been introduced since the 1970s on more than 20,000 reinforced concrete structures to extend their service life and reduce the overall

maintenance costs of concrete bridge decks [7]. The existence of epoxy layer on top of the reinforcing steel can provide barrier protection as long as the coating remains intact without mechanical damage nor severe water-uptake throughout the coating layer.

However, ECR can also be exposed to the unintended mechanical defects during fabrication, transport, or construction of the reinforced structures. When electrolyte uptakes throughout the concrete matrix, any existing defect on the coating would allow electrochemical reactions between the electrolyte and reinforcing steel to produce corrosion products [8,9]. The porous ferrous corrosion products often do not provide barrier protection for the substrate owing to their structures or layer forming scheme represented as the Pilling-Bedworth ratio (R_{PB}) [10,11]. Such features are illustrative that the formation of certain types of ferrous corrosion products would likely to allow a repeated water uptake that enables a continuous dissolution of the substrate [12].

To overcome the limitations of the ECR and extend the service period of the substrate, a self-healing coating concept has been suggested with the usage of nano- to micro-sized capsules filled with corrosion inhibitors. Such a technique allows an autonomous healing of the degrading sites by releasing the corrosion inhibitor only when the activating conditions are met. The capsules embedded in the coating can be activated by mechanically, chemically or electrochemically driven damages to build a protective layer [13–15]. Compared to the mechanically driven capsule activation that requires mechanical damage, the capsules can also be activated by local pH gradient due to electrochemical reactions at the electrolyte-substrate interface [16–18]. During the corrosion regime, there are local anodes and cathodes that shift their positions over time,

and this changes the local pH gradient that releases the corrosion inhibitor from the capsules to prevent further degradation.

Organic amines have been widely used as corrosion inhibitors due to their low costs and effective corrosion retarding capabilities [8,19]. Among these compounds, triethanolamine (TEA) has been widely studied because of its strong physisorption and chemical coordination with the metallic substrate. Successful applications have been observed with TEA when employed as a chemical admixture or as an encapsulated inhibitor in reinforced concrete [20–23]. Despite the extensive studies of the encapsulated corrosion inhibitors, there is still limited information its applicability in carbonated concrete. As such, this study evaluated the anticorrosion performance of encapsulated TEA on ECR with an artificial defect in a simulated carbonated concrete pore solution.

4.2. Materials and Methods

4.2.1. Sample Preparation

The TEA encapsulation was performed by following the procedures and related parameters shown in Table 2.1. No. 3 carbon steel reinforcement bars that meet ASTM A615 specifications ($0.24 < C < 0.33$, $S + P < 0.12$, and Fe balance, all wt.%) were used as the substrate. Prior to the coating, the substrates were sandblasted to remove existing corrosion products, then cleaned and degreased with ethanol. After cleaning, the rebars were dried prior to the coating application. The coating was prepared by mixing resin and hardner part of the MasterEmaco ADH 1090RS epoxy (BASF) then 30 wt.% of the synthesized nanocapsules was added. The coating mixture was then applied on the

substrate with an average coating thickness of 500 μm, and then cured with a desiccator filled with silica gel for humidity removal. An artificial defect with a width of 250 μm and a length of 5 mm was created before the coating was cured to prevent rupturing the embedded capsules. The samples with fully cured coating were subjected to ultrasonic cleaning then fully dried prior to the immersion test. Epoxy coated samples with no capsules were prepared as the control set prepared by the described steps also with an artificial defect. Duplicates of each coating type were prepared to evaluate the reproducibility of the results.

4.2.2. Electrochemical Measurements

To compare the electrochemical performance against the corrosion for the coating with or without the nanocapsules, the samples were immersed in a simulated carbonated concrete pore solution consisting of 0.015 M $NaHCO_3$ and 0.005 M Na_2CO_3 (pH ~ 9) [24]. Additionally, 3.5wt% NaCl was added to simulate an aggressive, chloride-rich condition. Such electrolyte was chosen to simulate the pore solution that is anticipated to be formed in the reinforced concrete structure that being exposed at the coastal region for a long period. Electrochemical impedance spectroscopy (EIS) measurements were conducted at open-circuit potential (OCP) using a potentiostat (Gamry Reference 1000E). A three-electrode electrochemical cell composed of ECR, graphite rod, and saturated calomel electrode (SCE) serving as working, counter, and reference electrodes, respectively, was used. The measuring frequency range of the impedance signal was from 100 kHz to 20 mHz, and 10 logarithmical frequency points were measured for each decade with an

amplitude of 10 mV rms. To characterize the anti-corrosion performance at the initial period, EIS measurements were successively performed during the 24-hour immersion period. The experimental setup used for the electrochemical testing is shown in Figure 4.1 with the exposed area of 12.16 cm^2. The setup was used for both types of coatings with and without the embedded nanocapsules.

4.2.3. Materials Characterization

The samples after the immersion test were optically visualized to qualitatively compare the effect of nanocapsule-containing coating under corrosive environment. The defective area was visualized more in detail using the scanning electron microscope (SEM, JEOL JCM-600 Plus) coupled with energy-dispersive X-ray spectroscopy (EDS) to

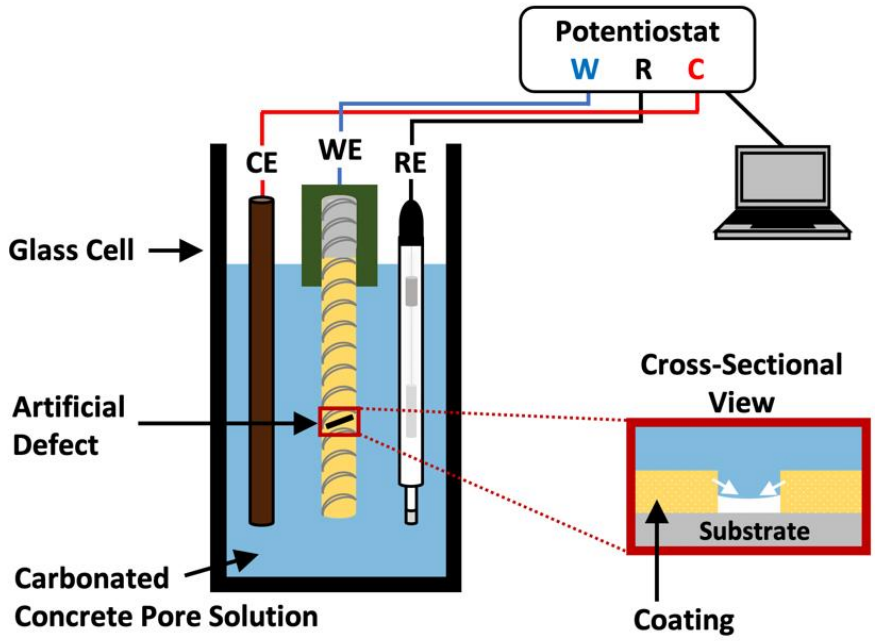

Figure 4.1. Experimental set-up for electrochemical testing (encapsulated TEA coating).

provide quantitative elemental analysis. The surface of the samples was pretreated with 5 nm Pt coating by sputter coater (Cressington 208 HR) prior to SEM-EDS to minimize surface charging.

To specify the types of corrosion products formed, X-ray powder diffraction (XRD, Bruker-D8 Advance) was performed with the corrosion products collected after the immersion test. The XRD patterns were obtained by Cu Kα radiation (1.5406 Å) from 15° to 70° (2θ) with a step size of 0.015°.

4.3. Results and Discussion

4.3.1. Open Circuit Potential (OCP)

The open circuit potential (OCP) can be used as a surface predominance indicator on whether the sample is undergoing corrosion [25]. Figure 4.2 shows the OCP trends of the samples during the immersion period using ASTM's criteria to classifying the corrosion condition [6]. The control sample experienced a freely corroding regime from the beginning of the immersion, and such regime continued until the 24-hour immersion. On the other hand, the sample with TEA coating initially showed higher OCP levels, which can be attributed to the release of TEA from the nearby nanocapsules in such early period. However, with the prolonged immersion, the OCP of the encapsulated TEA coating revealed more negative values that represented an insufficient level of substrate protection. Specifically, an inhibitive layer that formed during the earlier period may have been penetrated by the aggressive environment, which allowed the locally active metal

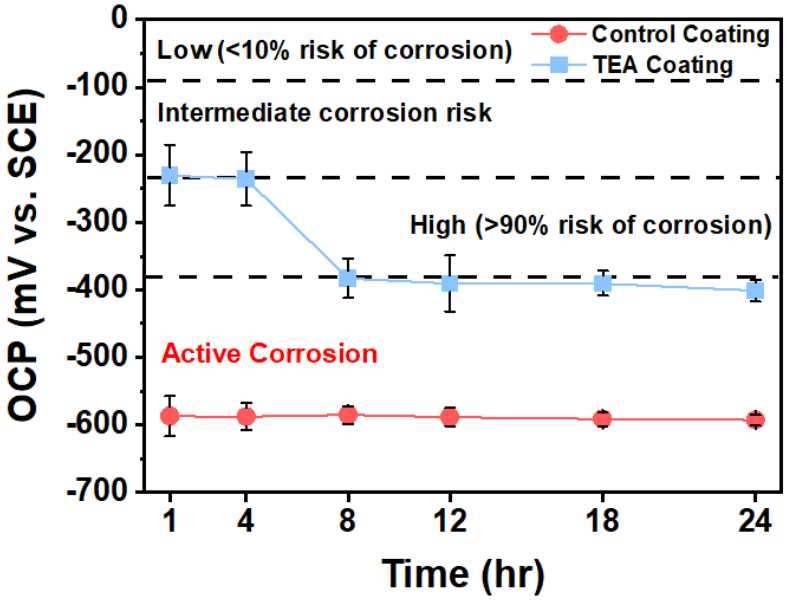

Figure 4.2. OCP evolution of different types of coatings over immersion testing.

dissolution that led to the incomplete formation of the protective layer. Such trend may have attributed to the immersion testing set-up that used the bulk electrolyte, since the TEA released from the nanocapsules may have been diluted, therefore the TEA concentration at the metal surface could have depleted significantly. Nevertheless, it is clear that the encapsulated TEA coating sample shows relatively more positive OCP values compared to that of the control sample throughout the immersion period, and such represents the exposed surface can be expected to be less stained following the aforementioned corrosion condition criterion [6]. Meanwhile, when the real concrete condition is considered for the practical application of ECR, the coated rebar is more likely to be exposed to local water uptake rather than being exposed to bulk solution. This may indicative that the concentration of TEA at the metal surface would not be diluted as much

in the case of bulk electrolyte, therefore the longer protection of the substrate can be expected.

4.3.2. EIS Study in a Simulated Carbonated Pore Solution

To investigate the changes of the surface properties over the immersion period, the EIS was performed in a simulated carbonated pore solution as shown in Figure 4.3. The Nyquist plot of the control sample, shown in Figure 4.3a, represents a freely corroding system of the coated material with defect. Specifically, it reveals the existence of multiple semicircles that can be attributed to the presence of coating at high-frequency (HF) range and electrolyte/metal interface at low-frequency (LF) range, respectively. Over the prolonged immersion, it is noticeable that the size of semicircles at the HF to mid-frequency (MF) range has increased. This can be due to the formation and accumulation of corrosion products as the freely corroding regime, also denoted by the OCP trend, continuously dissolved the substrate and produced the corrosion products.

Meanwhile, in Figure 4.3b that shows the Nyquist plot of the encapsulated TEA sample, where it is noticeable that the size of semicircle in the plot is considerably bigger than that of the control sample, especially in the early stage. Considering the control sample that revealed the freely corroding regime from the immersion, the encapsulated TEA sample is also likely to experience the corroding regime right after the immersion. By the active corrosion that brings the local pH gradient [26,27], it is estimated that the TEA had successfully released from the embedded nanocapsules to inhibit the existing corroding regime. Specifically, when local pH gradient occurs as a consequence of

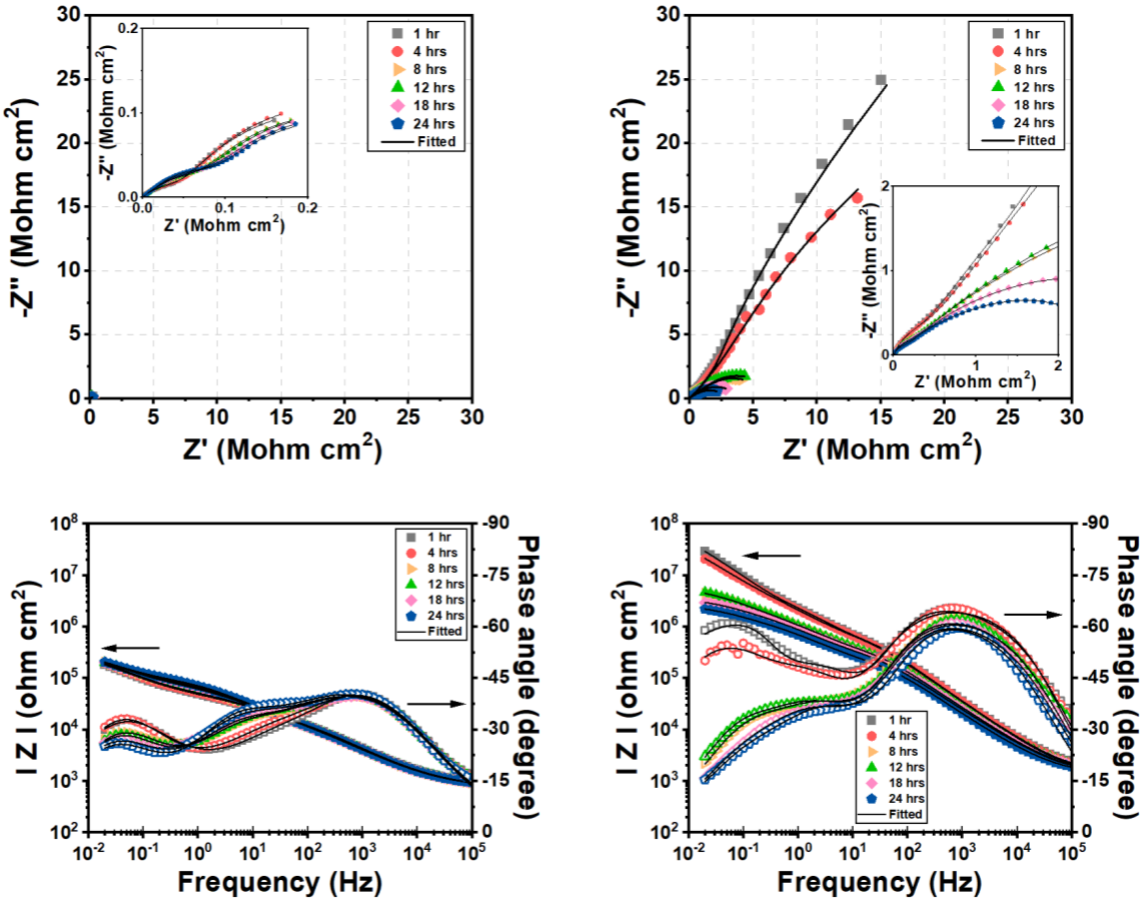

Figure. 4.3. Nyquist and Bode plots for the immersion test of (a,c) control and (b,d) encapsulated TEA coating.

corrosion activation processes, the salt-formed TEA existing inside of the nanocapsules can be ionizable and readily released by ionic diffusion through polymer wall [21]. Hence, when the exposed metal forms local anodic or cathodic sites, the electrolyte becomes locally basic or acidic respectively, and such allows enhanced hydrolysis of the salt that can be released into the electrolyte. The released TEA is adsorbed on the exposed metal surface via electron donation, and the array of the adsorbed amine species can serve as a barrier that isolates the substrate from corrosive electrolyte [8]. Such actions can be

illustrated as the bigger size of the Nyquist plot in the early period of immersion. Despite the formation of an inhibiting layer in the earlier period, Figure 4.3b also shows the gradual decrease of the size of the impedance over the prolonged immersion. This represents that the inhibiting layer formed in the earlier period may have allowed water uptake in local spots, therefore it is estimated that corrosion would have occurred in such local spots by introducing the corrosive media to produce corrosion products. As ferrous corrosion products are known to be soluble in aqueous condition and therefore they can be flaky and friable [28]. As such, this can provide another water uptake path even in the presence of an inhibiting layer, which may have resulted in the decrease of barrier performance over time. It is also worth noting that the gradually decreasing barrier performance in an early immersion may owing to the dilution of TEA released from the nanocapsules by the immersion in a bulk electrolyte, therefore the inhibiting performance of TEA may have underestimated in this study. Hence, future studies would be needed to evaluate the inhibiting performance under a real concrete system.

Figure 4.3c,d illustrates the Bode plots of the control and TEA samples, respectively. Throughout the immersion period, the control sample revealed three time-constants (TCs) which can be assigned to the contribution of coating, corrosion product, and charge transfer for HF, MF, and LF range, respectively. The evolution of time constant at MF around 10 Hz is noticeable, and this is owing to the accumulation of the corrosion products resulted by the freely corroding regime that the sample experienced. However, the TC positioned at LF also revealed a gradually decreasing phase angle values over the immersion period. This indicates that while the considerable amount of corrosion products

formed at the electrolyte/metal interface did not provide enough barrier effect and allowed a continuous water supply for the sequential electrochemical reactions at the exposed metal surface, which have occurred the continuous surface degradation by losing its semi-capacitive behavior.

With the presence of the encapsulated TEA in the coating, the sample revealed the existence of systems that correspond to coating, inhibiting film, and charge transfer mechanism. In addition to the Nyquist plot's trend, the Bode plot also reveals the considerable level of substrate protection in the early immersion period, represented by the impedance modulus (|Z|) and the relatively higher phase angle of the TCs. When the immersion was prolonged, the phase angle of the TCs at HF gradually decreased. In contrast, the control sample did not reveal such phase angle decrease at such frequency range, and this represents the gradual decrease of phase angle in the TEA sample may come from the gradual loss of the inhibiting performance. For that reason, the phase angle of the TC at both MF and LF also decreased at the longer immersion time which attributed to the aggressive electrolyte with an insufficient substrate protection. In spite of the imperfect inhibiting performance, the obtained impedance modulus (|Z|) of the encapsulated TEA sample is still over tenfold compared to that of the control sample throughout the immersion period, indicative that the encapsulated TEA coating can help delay the overall corrosion damage even when it may contain local defects.

An electrical equivalent circuit (EEC) models has proposed as shown in Figure 4.4 to provide quantitative analysis of the effective parameters in the electrochemical system. The impedance spectra of the sample with absence or presence of encapsulated TEA were

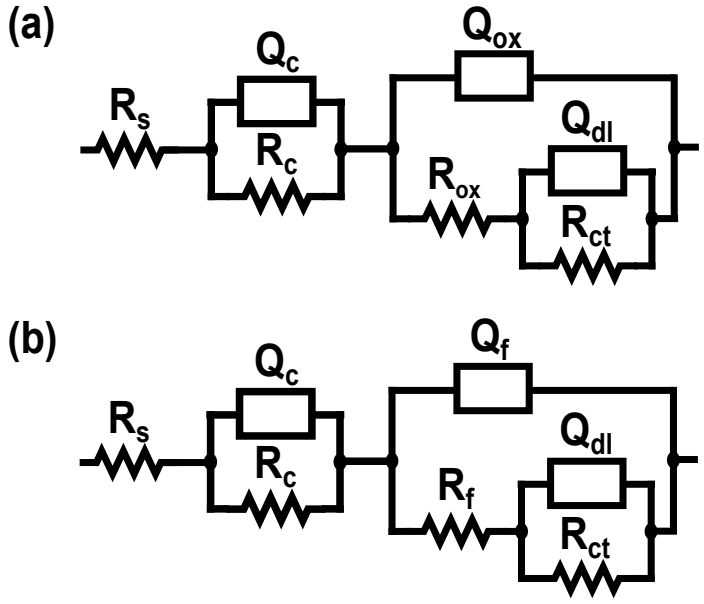

Figure 4.4. Schematic representation of the corresponding electrical equivalent circuits used for fitting the experimental EIS results of (a) control and (b) encapsulated TEA coating.

fitted with the EEC shown in Figure 4.4a,b, respectively. The EECs were composed of elements, namely, solution resistance (R_s), coating pore resistance (R_c), oxide layer resistance (R_{ox}), inhibiting layer resistance (R_f), charge-transfer resistance (R_{ct}), and the capacitance in terms of the constant phase element (CPE), coating film capacitance (Q_c), oxide layer capacitance (Q_{ox}), inhibiting layer capacitance (Q_f), and double-layer capacitance (Q_{dl}). The CPE concept was introduced to represent the depressed impedance loops, which can be occurred from the distribution of physical properties, resulting in the time constant distributions [29].

The quantified impedance parameters obtained from the EECs are listed in Table 4.1. In the case of the control sample, the gradually increasing R_{ox} values over the immersion period can be caused by an accumulation of porous corrosion products from a

Table 4.1. Impedance parameters for the corrosion of ECR in simulated carbonated pore solution.

Control Coating

Time (hrs)	R_c ($\Omega\ cm^2$)	Q_c ($F\ cm^{-2}\ s^{n-1}$)	n_c	R_{ox} ($\Omega\ cm^2$)	Q_{ox} ($F\ cm^{-2}\ s^{n-1}$)	n_{ox}	R_{ct} ($\Omega\ cm^2$)	Q_{dl} ($F\ cm^{-2}\ s^{n-1}$)	n_{dl}	R_p ($\Omega\ cm^2$)	χ^2
1	4.1×10^4	3.6×10^{-6}	0.52	3.8×10^3	1.2×10^{-6}	0.76	3.7×10^5	1.8×10^{-5}	0.64	4.1×10^5	8.4×10^{-3}
4	4.9×10^4	3.6×10^{-6}	0.53	5.1×10^3	2.2×10^{-6}	0.66	3.5×10^5	1.8×10^{-5}	0.69	4.0×10^5	8.0×10^{-3}
8	5.5×10^4	3.6×10^{-6}	0.64	1.5×10^4	2.6×10^{-6}	0.56	3.2×10^5	1.8×10^{-5}	0.70	3.9×10^5	7.7×10^{-3}
12	5.8×10^4	3.6×10^{-6}	0.66	1.8×10^4	2.6×10^{-6}	0.55	3.1×10^5	1.8×10^{-5}	0.70	3.9×10^5	8.1×10^{-3}
18	6.4×10^4	3.3×10^{-6}	0.67	1.7×10^4	2.6×10^{-6}	0.55	3.1×10^5	1.9×10^{-5}	0.68	3.9×10^5	8.8×10^{-3}
24	6.6×10^4	3.0×10^{-6}	0.70	1.9×10^4	2.4×10^{-6}	0.55	3.0×10^5	1.9×10^{-5}	0.68	3.8×10^5	1.0×10^{-2}

Encapsulated TEA Coating

Time (hrs)	R_c ($\Omega\ cm^2$)	Q_c ($F\ cm^{-2}\ s^{n-1}$)	n_c	R_f ($\Omega\ cm^2$)	Q_f ($F\ cm^{-2}\ s^{n-1}$)	n_f	R_{ct} ($\Omega\ cm^2$)	Q_{dl} ($F\ cm^{-2}\ s^{n-1}$)	n_{dl}	R_p ($\Omega\ cm^2$)	χ^2
1	2.3×10^5	3.4×10^{-8}	0.89	1.2×10^7	1.2×10^{-7}	0.67	2.7×10^8	3.4×10^{-8}	1	2.8×10^8	2.1×10^{-2}
4	3.4×10^5	5.0×10^{-8}	0.81	1.1×10^7	1.4×10^{-7}	0.68	8.9×10^7	7.0×10^{-8}	0.79	1.0×10^8	2.5×10^{-2}
8	1.8×10^5	5.9×10^{-8}	0.83	2.8×10^6	2.7×10^{-7}	0.63	3.2×10^6	4.9×10^{-7}	0.74	6.2×10^6	2.2×10^{-2}
12	2.0×10^5	6.6×10^{-8}	0.80	3.3×10^6	2.9×10^{-7}	0.63	3.3×10^6	5.5×10^{-7}	0.77	6.8×10^6	2.7×10^{-2}
18	1.7×10^5	7.3×10^{-8}	0.81	2.5×10^6	3.5×10^{-7}	0.62	1.2×10^6	1.3×10^{-6}	0.73	3.9×10^6	1.8×10^{-2}
24	1.1×10^5	7.7×10^{-8}	0.83	1.6×10^6	4.0×10^{-7}	0.62	1.0×10^6	1.6×10^{-6}	0.72	2.7×10^6	1.6×10^{-2}

freely corroding substrate. Since such permeable layer cannot block the electrolyte uptake, the electrochemical charge transfer reactions could have continuously occurred, as evidenced by the gradual decrease of the R_{ct} values. Additionally, the increasing trend of the Q_{dl} values was attributed to the active corrosion regime with extensive charge transfer reactions, which results in an increased double layer charge capacity. Meanwhile, the sample with encapsulated TEA revealed a superior substrate protection especially in an early immersion period, as seen through the higher R_{ct} values compared to the control sample, and this comes from the barrier contribution of the inhibiting layer represented as R_f. Meanwhile, over the prolonged immersion, there was a gradual decrease of the inhibiting performance represented by the decrease of R_f and R_{ct} values which also resulted in a decrease of $R_p = \sum R$. This is potentially due to the locally activating spots by dissolving or electrolyte up-taking corrosion products and the lack of protective native oxide of the substrate from the aggressive electrolyte condition [30]. Nevertheless, it is obvious that the encapsulated TEA sample experienced considerably delayed the corrosion regime by maintaining higher corrosion resistance values with the presence of inhibiting layer. Specifically, inhibiting layer represented the higher resistance and lower capacitance values compared to those of the corrosion product layer from the control sample throughout the immersion tests, and these indicate the inhibitor that came from the embedded nanocapsules successfully provided efficient barrier protection better than the accumulated corrosion products. Despite of the gradually increasing Q_{dl} values of such sample, which may be illustrative of the weakened substrate protection, such capacitance values were maintained in a lower range for the TEA sample than those of the control

sample, denoting that the metal/electrolyte interface would have remained relatively less degraded over the immersion test.

4.3.3. Corrosion Inhibiting Action by SVET Study

The localized electrochemical reactions on the artificial defect of both control and encapsulated TEA samples in simulated carbonated pore solution (pH ~9, Resistivity ~1.70 ohm-cm) were studied using SVET analysis, as illustrated in Figure 4.5. The control sample, shown in Figure 4.5a, represents considerably higher current density in the early period which is owing to the vigorous charge-transfer reactions without any barrier effect. Over the prolonged immersion, the surface activity in terms of current density tended to be slightly lower, and this may have attributed to the formation of corrosion products that provided a temporary barrier effect. However, the exposed surface was still revealing the appreciable current density values, and this is estimated by the formation of permeable corrosion products that kept allowing aggressive species to the electrolyte/metal interface.

Meanwhile, the TEA encapsulated sample revealed a greatly suppressed corrosion attack throughout the immersion period as shown in Figure 4.5b. Such decreased corrosion activity can be attributed to the successful release of TEA by the local pH gradient which occurred during the earliest immersion period. Additionally, the TEA encapsulated sample did not show a dramatic change in terms of the surface current density values during the given immersion period, which maintained a lower current density range without the aggressive corrosion. This suggests that while an inhibiting layer may have been formed imperfectly due to the absence of native protective oxide and dissolving iron corrosion

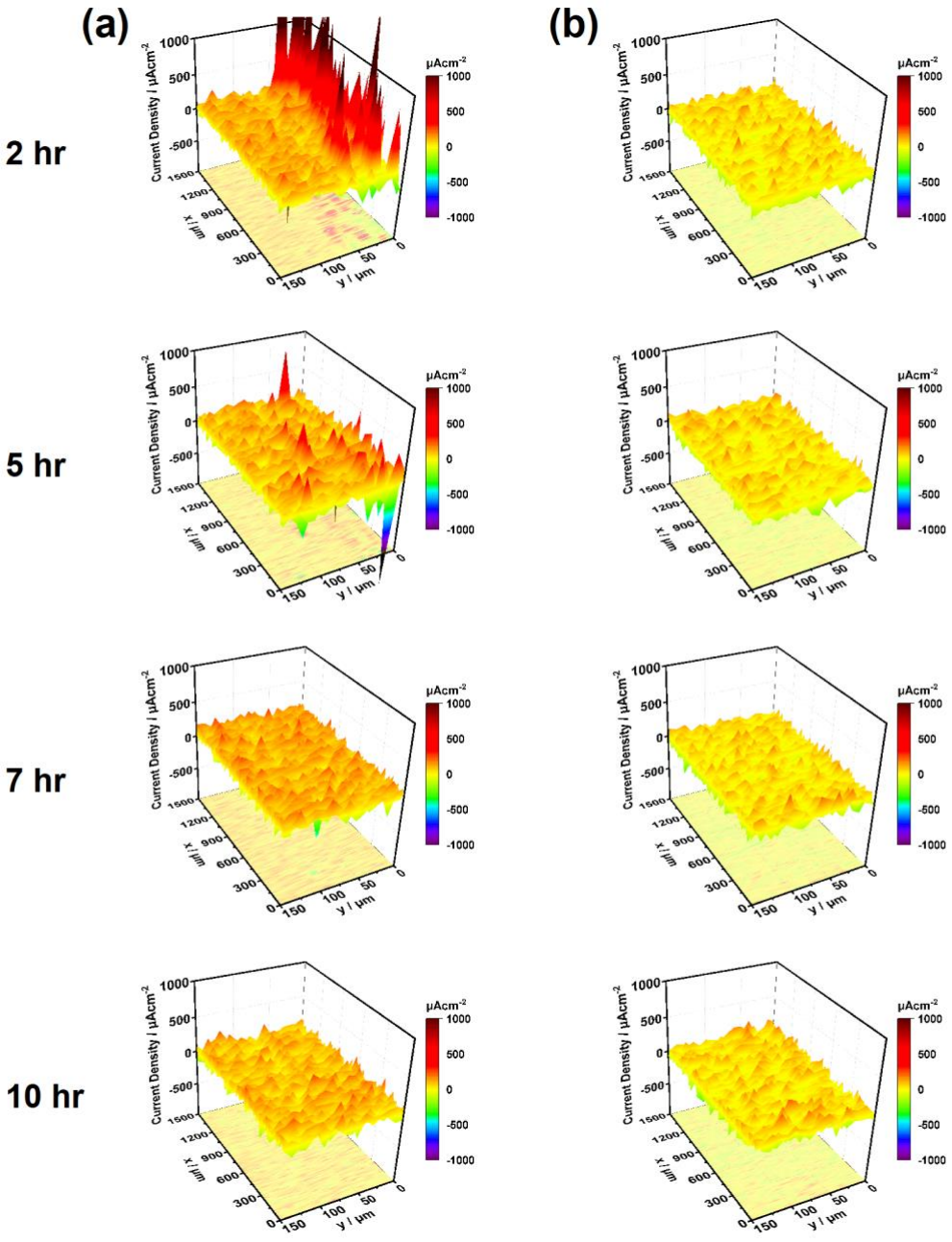

Figure 4.5. SVET current density maps of the scanned area for the immersion test of (a) control and (b) encapsulated TEA coating.

products, the continued release of TEA in response to such local metal dissolution may have helped keep the surface current density level considerably lower than that of the

control sample, which agrees with the previous EIS results by its corrosion resistance.

4.3.4. Post-Immersion Characterization

To investigate the surface degradation of the artificial defect the SEM micrographs with elemental analyses were obtained as shown in Figure 4.6. Figure 4.6a,c,e illustrates the surface of the control sample after corrosion testing, where the exposed surface was considerably oxidized and featured distinctive bulky corrosion products. However, in Figure 4.6b,d,f, the TEA encapsulated sample showed an exposed substrate that was relatively less degraded than the control sample, mostly revealing thin and plate-like surface morphology. Such finding is also supported by the O/Fe atomic ratio, where the control sample experienced more of substrate oxidation in terms of extensive charge transfer reactions at the electrolyte/metal interface. The enhanced anti-corrosion performance of the TEA encapsulated sample is attributed to the mild corrosion during the early period immersion that allowed the release of corrosion inhibitors. Meanwhile, the exposed substrate of the TEA encapsulated sample also had an O/Fe ratio close to 1, indicating that the substrate protection was imperfect. This can be owing to the presence of carbonate/bicarbonate ions that can accelerate the dissolution of ferrous substate by forming a dissolvable pseudo-passive film [31,32], which may have prevented the formation of a more compact inhibiting layer. Nevertheless, it is clear that the artificial defect of the TEA encapsulated sample experienced a slower surface oxidation with a suppressed charge transfer reaction, suggesting that the exposed surface was relatively well-preserved under an aggressive electrolyte condition.

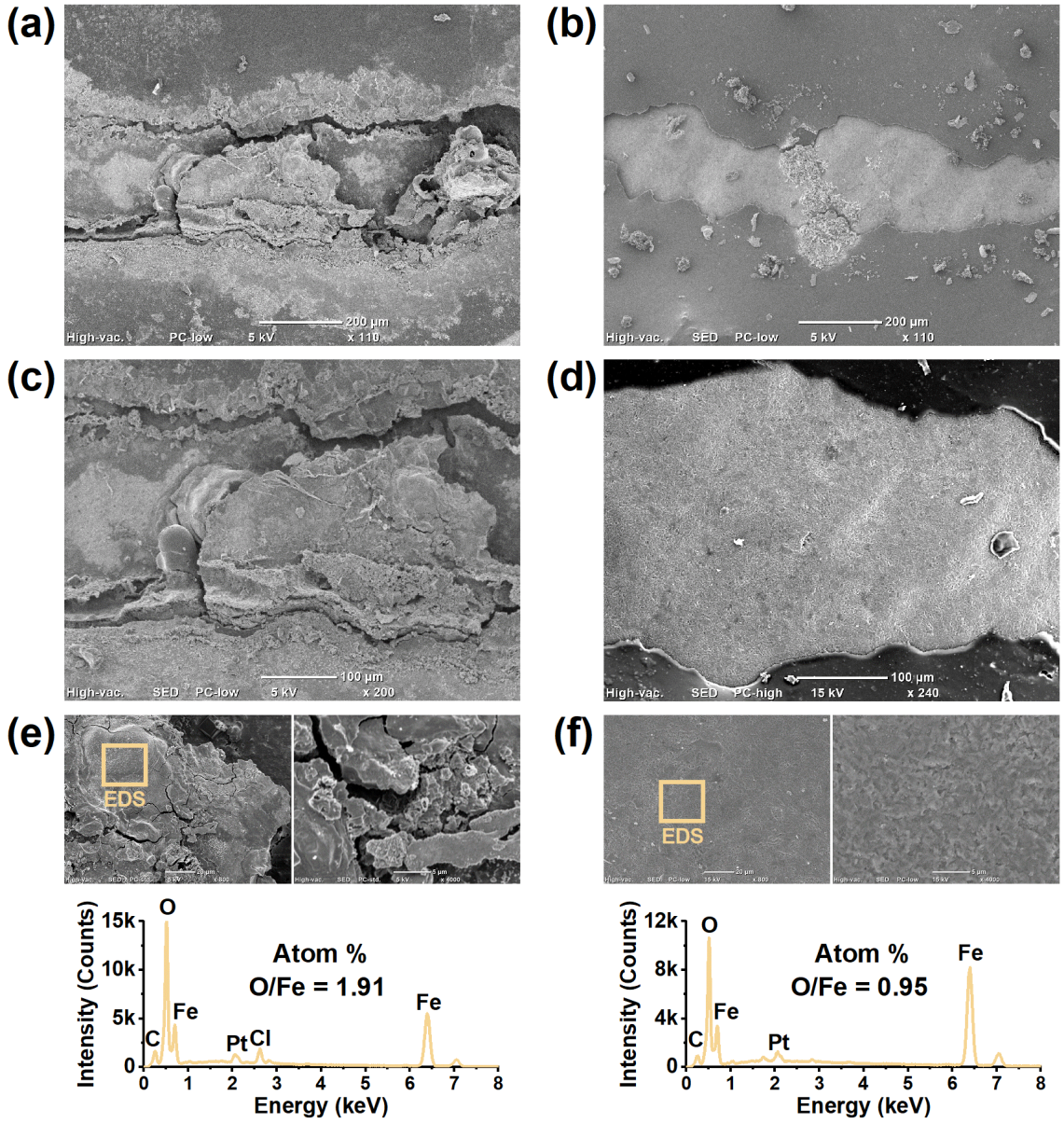

Figure 4.6. SEM micrographs with EDS analysis for the artificially defected area of (a,c,e) control and (b,d,f) encapsulated TEA coating.

The XRD patterns of the corrosion products from each type of coating are shown in Figure 4.7. The corrosion products for both samples consisted of γ-Fe_2O_3 (maghemite, JPDF No. 39-1346), Fe_3O_4 (magnetite, JPDF No. 79-0417), γ-FeO(OH) (lepidocrocite,

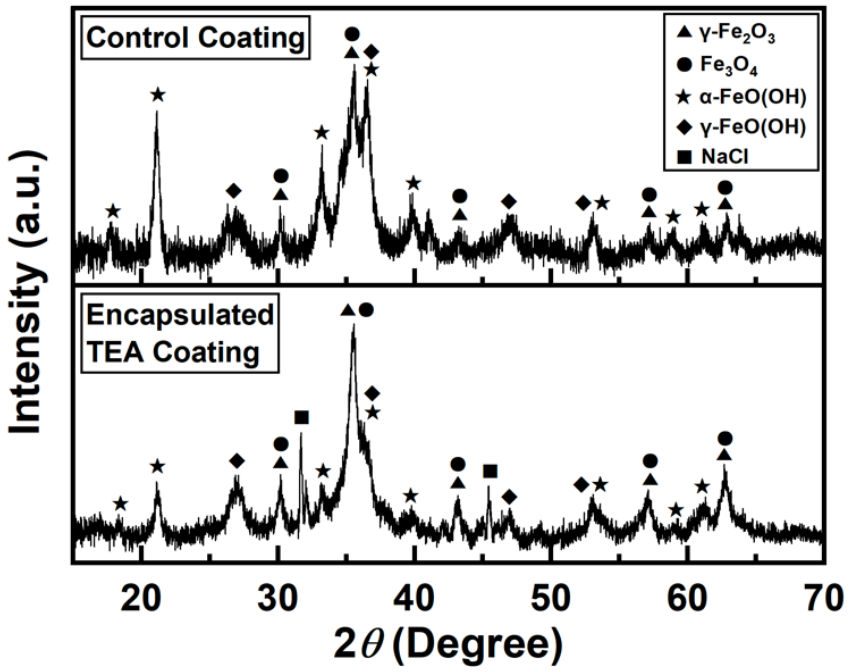

Figure 4.7. XRD patterns of the corrosion products obtained after immersion test from different types of coatings.

JPDF No. 74-1877), and α-FeO(OH) (goethite, JPDF No. 29-0713). In the early period of immersion, it is estimated that both samples allowed electrochemical reactions that resulted in the formation of Fe_3O_4 corrosion products [28,33]. In the case of the TEA encapsulated sample, such electrochemical reactions in the early period have caused the formation of local anodes and cathodes that triggered the local pH gradient that allowed an accelerated release of the inhibitor to provide a barrier protection. Therefore, such initial corrosion products could have been retained by delayed further oxidation, as illustrated in Figure 4.6b,d,f that revealed the lower O/Fe ratio than that of the control sample. Additionally, the XRD pattern for the encapsulated TEA coating is indicative that the dominant corrosion product is likely to be the Fe_3O_4 rather than other minor corrosion products, also denotes suppressed further oxidation of the surface.

Meanwhile, the control sample revealed an extensively oxidized surface as shown in Figure 4.6a,c,e, and this suggests the initial corrosion products are likely to be transformed by further oxidation. Specifically, it is estimated that the Fe_3O_4 layer formed in the earlier period may have experienced partial transformation towards γ-Fe_2O_3 which is known to be non-protective by its R_{PB}, therefore the electrochemical reactions could have continued at the electrolyte/metal interface [10,28,33]. Additionally, the γ-FeO(OH) that formed can be also transformed into α-FeO(OH) owing to its thermodynamic instability [34], and their non-protective structures would have allowed repeated water uptake [11,12]. Meanwhile, it is observable that there is no distinct difference in the types of formable corrosion products between the samples. This illustrates that both samples had similar electrochemical reaction pathway during the immersion test, albeit with a different level of surface degradation on the exposed substrate by the presence of TEA nanocapsules.

4.3.5. Corrosion Inhibiting Action by Nanocapsules

Figure 4.8 shows the schematic illustration of delaying corrosion damage by the embedded nanocapsules containing TEA corrosion inhibitor. Through the artificial defect produced on the substrate was exposed to the electrolyte that contains corrosive species. Once the electrochemical charge transfer reactions initiate, the pH gradient formed nearby the active substrate triggers the release of TEA from the nanocapsules. The released inhibitor species can be adsorbed on the exposed metal surface to provide a barrier effect that isolates the substrate from the corrosive electrolyte environment. As shown in the

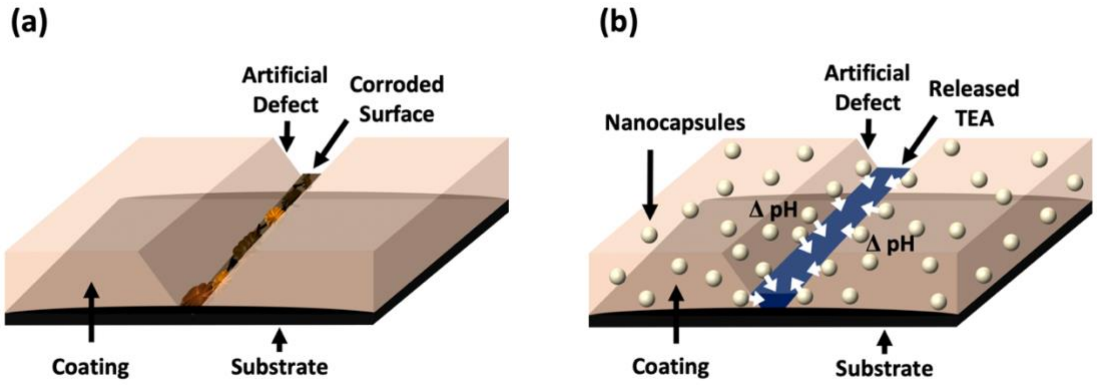

Figure 4.8. Schematic illustration of dominating regime at artificially defected area in (a) control and (b) encapsulated TEA coating.

previous results, including OCP, EIS, SVET, and surface micrography, the application of the nanocapsules into the ECR system successfully slowed down the electrochemical material degradation. Compared to the control sample that revealed the severe corrosion regime throughout the tests, the smart coating equipped with an extra barrier protection can help with suppressing the corrosion activity, possibly leads to the longer service period of the reinforcing steel at last.

4.4. Summary

This study described the application of an encapsulated corrosion inhibitor, TEA, into an epoxy coated rebar system to achieve an enhanced substrate protection from the corrosive environment. The electrochemical signals, such as relatively more positive OCP values and noticeable differences in impedance parameters obtained illustrated an enhanced barrier protection of the exposed metal surface, especially during an early immersion period. According to the SVET measurements, the current density of the

encapsulated TEA sample was maintained at a considerably lower range than that of the control sample. Such results were further evidenced by the surface characterization, where the TEA sample showed a less degraded surface with a lower O/Fe ratio, indicating the oxidation of the substrate was delayed by the released TEA from the embedded nanocapsules. Meanwhile, the level of surface oxidation also affected the surface morphology due to the formation of corrosion products. The control sample showed the formation of bulky and further oxidized corrosion products that would have allowed continued water uptake by their non-protective features, which caused continued active corrosion regime. In contrast, the surface of encapsulated TEA sample was considerably less degraded, evidenced by thin and plate-like surface morphology, showing that the further oxidation of exposed surface was suppressed by having an extra barrier protection from the embedded nanocapsules.

4.5. References

[1] W.H. Hartt, R.G. Powers, V. Leroux, D.K. Lysogorski, Critical literature review of high-performance corrosion reinforcements in concrete bridge applications, United States. Federal Highway Administration. Office of Infrastructure Research and Development, 2004.

[2] J.A. Grubb, H.S. Limaye, A.M. Kakade, Testing pH of Concrete, CI. 29 (2007) 78–83.

[3] C. Kim, D.-E. Choe, P. Castro-Borges, H. Castaneda, Probabilistic Corrosion Initiation Model for Coastal Concrete Structures, Corrosion and Materials Degradation. 1 (2020) 328–344.

[4] D.D. Macdonald, The point defect model for the passive state, Journal of The Electrochemical Society. 139 (1992) 3434.

[5] U.M. Angst, B. Elsener, C.K. Larsen, Ø. Vennesland, Chloride induced reinforcement corrosion: Electrochemical monitoring of initiation stage and chloride threshold values, Corrosion Science. 53 (2011) 1451–1464.

[6] J.P. Broomfield, Steel corrosion in concrete—Understanding, investigation and repair, Taylor & Francis: London, UK, 2007.

[7] Y.P. Virmani, G.G. Clemena, Corrosion protection: Concrete bridges, United States. Federal Highway Administration, 1998.

[8] E. McCafferty, Introduction to corrosion science, Springer Science & Business Media, 2010.

[9] M. Pourbaix, Atlas of electrochemical equilibria in aqueous solutions, National Association of Corrosion Engineers, 1974.

[10] M. Schütze, D.R. Holmes, Protective oxide scales and their breakdown, Wiley Chichester, 1997.

[11] D. De la Fuente, I. Díaz, J. Simancas, B. Chico, M. Morcillo, Long-term atmospheric corrosion of mild steel, Corrosion Science. 53 (2011) 604–617.

[12] T. Kamimura, S. Hara, H. Miyuki, M. Yamashita, H. Uchida, Composition and protective ability of rust layer formed on weathering steel exposed to various environments, Corrosion Science. 48 (2006) 2799–2812.

[13] S.H. Cho, S.R. White, P.V. Braun, Self-Healing Polymer Coatings, Advanced Materials. 21 (2009) 645–649.

[14] S.K. Ghosh, Self-healing materials: fundamentals, design strategies, and applications, Wiley Online Library, 2009.

[15] A. Kumar, L.D. Stephenson, J.N. Murray, Self-healing coatings for steel, Progress in Organic Coatings. 55 (2006) 244–253.

[16] A. Turnbull, Corrosion chemistry within pits, crevices and cracks, International Atomic Energy Agency, 1987.

[17] J. Ress, U. Martin, J. Bosch, D.M. Bastidas, pH-Triggered Release of NaNO2 Corrosion Inhibitors from Novel Colophony Microcapsules in Simulated Concrete Pore Solution, ACS Appl. Mater. Interfaces. 12 (2020) 46686–46700.

[18] J. Ress, U. Martin, J. Bosch, D.M. Bastidas, Protection of Carbon Steel Rebars by Epoxy Coating with Smart Environmentally Friendly Microcapsules, Coatings. 11 (2021) 113.

[19] T. Szauer, A. Brandt, On the role of fatty acid in adsorption and corrosion inhibition of iron by amine—fatty acid salts in acidic solution, Electrochimica Acta. 26 (1981) 1257–1260.

[20] W. Shang, C. He, Y. Wen, Y. Wang, Z. Zhang, Performance evaluation of triethanolamine as corrosion inhibitor for magnesium alloy in 3.5 wt% NaCl solution, RSC Advances. 6 (2016) 113967–113980.

[21] H. Choi, Y.K. Song, K.Y. Kim, J.M. Park, Encapsulation of triethanolamine as organic corrosion inhibitor into nanoparticles and its active corrosion protection for steel sheets, Surface and Coatings Technology. 206 (2012) 2354–2362.

[22] C. Kim, A.I. Karayan, J. Milla, M. Hassan, H. Castaneda, Smart Coating Embedded with pH-Responsive Nanocapsules Containing a Corrosion Inhibiting Agent, ACS Appl. Mater. Interfaces. 12 (2020) 6451–6459.

[23] J.O. Okeniyi, A.P.I. Popoola, C.A. Loto, Corrosion-inhibition and compressive-strength performance of Phyllanthus muellerianus and triethanolamine on steel-reinforced concrete immersed in saline/marine simulating-environment, Energy Procedia. 119 (2017) 972–979.

[24] L. Bertolini, F. Bolzoni, T. PASTORE, P. Pedeferri, Behaviour of stainless steel in simulated concrete pore solution, British Corrosion Journal. 31 (1996) 218–222.

[25] M. Pourbaix, Thermodynamics and corrosion, Corrosion Science. 30 (1990) 963–988.

[26] T. Balusamy, T. Nishimura, In-Situ Monitoring of Local Corrosion Process of Scratched Epoxy Coated Carbon Steel in Simulated Pore Solution Containing Varying percentage of Chloride ions by Localized Electrochemical Impedance Spectroscopy, Electrochimica Acta. 199 (2016) 305–313.

[27] X. Chen, X.G. Li, C.W. Du, Y.F. Cheng, Effect of cathodic protection on corrosion of pipeline steel under disbonded coating, Corrosion Science. 51 (2009) 2242–2245.

[28] G.S. Duffó, W. Morris, I. Raspini, C. Saragovi, A study of steel rebars embedded in concrete during 65 years, Corrosion Science. 46 (2004) 2143–2157.

[29] B. Hirschorn, M.E. Orazem, B. Tribollet, V. Vivier, I. Frateur, M. Musiani, Constant-Phase-Element Behavior Caused by Resistivity Distributions in Films I. Theory, J. Electrochem. Soc. 157 (2010) C452–C457.

[30] D.D. Macdonald, Y. Zhu, J. Yang, J. Qiu, G.R. Engelhardt, A. Sagüés, L. Sun, Z. Xiong, Corrosion of rebar in concrete. Part IV. On the theoretical basis of the chloride threshold, Corrosion Science. 185 (2021) 109460.

[31] M. Moreno, W. Morris, M.G. Alvarez, G.S. Duffó, Corrosion of reinforcing steel in simulated concrete pore solutions: Effect of carbonation and chloride content, Corrosion Science. 46 (2004) 2681–2699.

[32] D.H. DAVIES, G.T. BURSTEIN, The Effects of Bicarbonate on the Corrosion and Passivation of Iron, Corrosion. 36 (1980) 416–422.

[33] S. Kim, J. Surek, J. Baker-Jarvis, Electromagnetic Metrology on Concrete and Corrosion, J Res Natl Inst Stand Technol. 116 (2011) 655–669.

[34] R.M. Cornell, U. Schwertmann, The Iron Oxides: Structure, Properties, Reactions, Occurrences and Uses, John Wiley & Sons, 2003.

5. CORROSION BEHAVIOR OF AL-SI-MG COATED HOT-PRESS-FORMING STEEL*

This study introduces enhanced corrosion performance of the Al-Si-Mg coated 22MnB5 boron steel. Structural changes of the coating after hot-dip-aluminizing and hot-press-forming processes with presence of Mg included compacter surface with Mg segregation and thicker crack-free layer. Electrochemical corrosion tests indicated higher polarization resistance from Al-Si-Mg sample compared to reference Al-Si sample, especially in early period of immersion. Such enhanced anti-corrosion performance can be attributed to aforementioned structural changes and pore-filling effect of corrosion products. This study depicts that the Al-Si-Mg coating can be considered as another option for hot-press-forming steel by its enhanced barrier protection vs. Al-Si coating.

5.1. Introduction

The demands for light-weight vehicles to be equipped with Ultra-High-Strength-Steel (UHSS) has been globally increased in past decades by enhanced safety and environmental regulations in the automotive industry. In accordance with such a trend, the field of hot-press-forming (HPF) steel has received much attention for its advantages, such that allows high tensile strength, simplified joining, and stress-relieving characteristics

* Part of this section is reprinted with permission from "Corrosion behavior of Al-Si-Mg coated hot-press-forming steel" by Changkyu Kim, Seongkoo Cho, Wonseog Yang, Ahmad Ivan Karayan, and Homero Castaneda, 2021. *Corrosion Science*, 183, 109339,

[1,2]. In the HPF process, the cold-rolled blank steel sheet is de-coiled then heated up to 880-950°C for 3-10 minutes to obtain austenite microstructure. The sheet is then compressed by pressing die and water-quenched to achieve a full martensitic transformation, which provides ultra-high tensile strength that exceeds 1 GPa [1,3].

The application of a coating, also known as hot-dip aluminizing (HDA), aims to prevent either substrate oxidation or decarburization during the HPF process. The HDA process for the conventional Al-Si includes dipping of the de-coiled plate into the Al-Si melting pot for a few seconds under inert environment. Such Al-Si coating has been popularly used to provide substrate protection by oxidized aluminum layer from corrosion even after the HPF process. In addition to the general HPF process, the coating can be applied right after the de-coiling process prior to the heating as shown in Figure 5.1. The

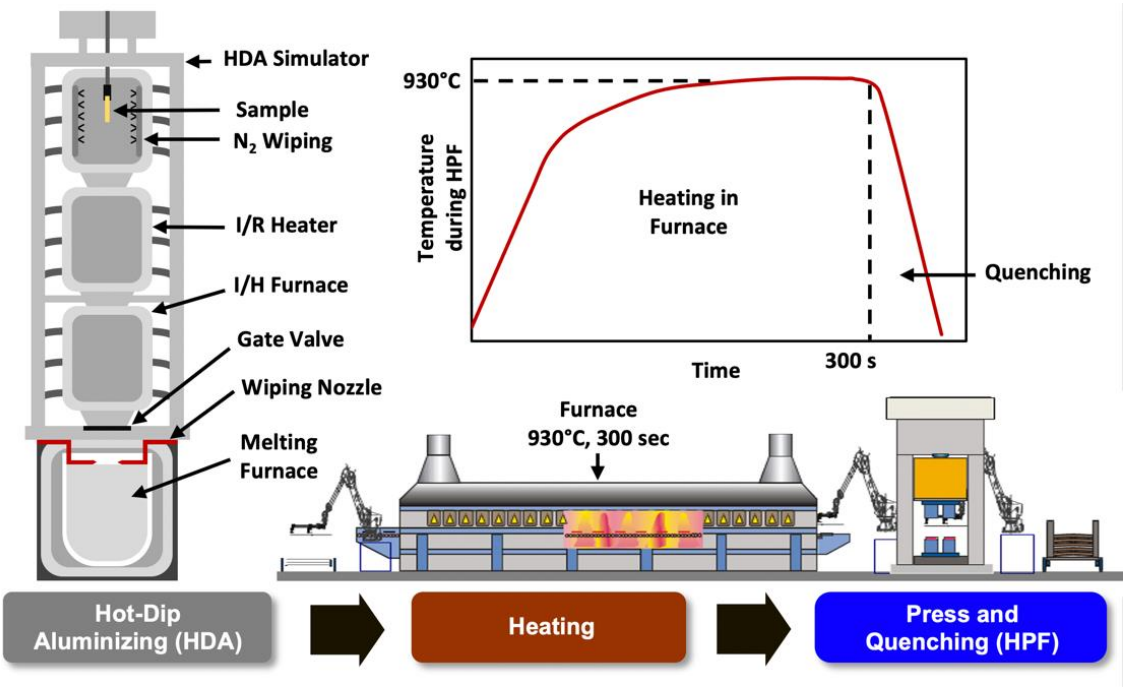

Figure 5.1. General hot-dip-aluminizing and hot-press-forming process.

applied coating experiences noticeable structural changes during the prolonged heat treatment for steel austenitization at high temperature over 900°C, and such structural changes occurred are known to provide anti-corrosion properties by enhancing the barrier performance.

The applied coating by the HDA process can be classified into 2 types depending on the presence of Si: when the coating is composed of Al with 7-11 wt% Si, it is called a type-1 aluminized coating, whereas a type-2 aluminized coating contains no Si [3]. It is known that the addition of Si (7-11 wt%) allows a formation of Fe_2SiAl_7 interdiffusion layer during HDA which limits the growth of Fe-Al intermetallic phases between the coating and substrate during the HPF [4].

The morphology of the coating layer is known to be affected by multiple parameters, including heating rate, temperature, heating period, and chemical composition [5,6]. It has been shown that the more continuous layers are generally formed with a lower heating rate or shorter heat treatment, and faster heating rate or longer heat treatment tends to cause more of island-type coating morphology. The structures of the multi-layered aluminized coating after HPF have been extensively reported from previous studies that have processing parameters of around 5 minutes of retention at over 900°C [5,7–9]. The chemical composition of such layers was revealed as the combination of intermetallic compounds among Fe, Al, and Si, forming $FeAl_2$, Fe_2SiAl_2, and Fe(Al,Si) by iron diffusion from the bulk substrate.

Meanwhile, it is known that such intermetallic layers do not provide cathodic protection, but just barrier protection [8], and it can be possibly explained by the formation

of Fe-Al intermetallic phases throughout the coating matrix during the HPF process that known to have the similar volta potential range compared to that of the substrate [10,11]. Additionally, since the Al-Si coating is susceptible to microcrack due to the different thermal expansion coefficient between coating and substrate, the thickness of the diffusion layer, where the microcrack does not propagate, has been considered as an important factor for a better corrosion performance [1,12].

To enhance the anti-corrosion performance of the Al-Si coating, an addition of the Mg element has been suggested [13–18]. It has been reported that the addition of Mg can possibly enhance the anti-corrosion performance of the aluminized coating by a formation of the Mg_2Si phase that allows cathodic protection. Additionally, an introduction of Mg to Al-Zn-Si coating occurred a better corrosion resistance by exhibiting both Mg_2Si and $MgZn_2$ phases [19]. Although such studies have mostly focused on the cathodic protection feature that is obtainable as a result of the HDA process, but there is still a lack of knowledge in regards of the possible role of Mg during the HPF process that includes prolonged high temperature heat treatment and quenching for martensitic transformation of the substrate [8].

Meanwhile, it is also known that the Mg element addition in Al-rich phase can possibly occur surface segregation through a prolonged heat treatment [20–22]. Considering the rough surface morphology from the existing voids of conventional Al-Si coating after HPF process [5,7,23], such Mg segregation during the heat treatment, represented here by HDA and HPF, can possibly modify the top-most surface with filling the existing voids, and this may contribute to enhance the barrier property of the coating.

In this study, the effect of the Mg addition (0.1 and 0.5 wt.%) into the conventional Al-Si coating on the corrosion performance is investigated. The differences driven by varied coating element compositions before and after the HPF process are discussed, and it is also described how such differences can affect to the anti-corrosion performance evaluated by electrochemical tests. This study conveys the Al-Si-Mg coating for corrosion control action and shows its possibility to be used as a primer prior to the electrodeposited (ED) painting to provide a longer service period.

5.2. Experimental Section

5.2.1. Hot-Dip-Aluminizing (HDA) and Hot-Press-Forming (HPF)

Blank sheets of 22MnB5 (C 0.22 wt.%, Mn 1.19 wt.%, Si 0.24 wt.%, B 0.02 ppm, Fe balance) were obtained from Hyundai Steel and used for all experiments. The HDA was performed with the 1.0 mm thickness of samples by dipping them into the ~660°C molten Al-Si or Al-Si-xMg (x=0.1 or 0.5) bath for 3 seconds, under an inert nitrogen environment. The chemical compositions of Al-Si, Al-Si-0.1Mg, and Al-Si-0.5Mg coatings are shown in Table 5.1. The nitrogen wiping was also applied to control the thickness of the coating as 18-20 μm during the HDA. Following the HDA process, the samples were annealed at 930°C for 300 seconds to form austenitization then pressed and water-quenching for the full lath martensitic transformation of the substrate during the HPF process. The yield strength of 1.5 GPa was obtained for all the samples used in this study.

Table 5.1. Chemical compositions of the Al-Si and Al-Si-Mg coatings used in this study.

Coating Types		Al-Si	Al-Si-0.1Mg	Al-Si-0.5Mg
Chemical Composition (wt %)	Si	6.97	6.37	6.49
	Mg	-	0.065	0.495
	Al	Residual		

5.2.2. Surface and Coating Characterization

The samples before and after the HPF process were characterized using a scanning electron microscope (SEM, JEOL JCM-600 Plus) coupled with energy-dispersive X-ray spectroscopy (EDS). The SEM visualized the morphology of both top and cross-sectional surfaces of the coating, and the EDS revealed the elemental distributions that can help to investigate the effect of the prolonged heat treatment on coating structures, either layered- or island-type. Prior to SEM-EDS, both top and epoxy-mounted cross-sectional surfaces were pretreated with 2 nm thick Pt coating by sputter coater (Cressington 208 HR) to minimize surface charging.

To evaluate the formation of different intermetallic compounds by varied chemical element compositions, the existing compounds after the HPF were identified by X-ray diffraction (XRD, Bruker-D8 Advance) operated with Cu Kα radiation (1.5406Å). The samples were scanned continuously from 10° to 70° with a step size of 0.015°. Additionally, the outermost surface chemical compositions were confirmed by X-ray photoelectron spectroscopy (XPS, Omicron XPS/UPS with Argus detector) performed with Mg Kα X-ray source (1253.6 eV), to evaluate how the top most surface has been modified by the added Mg element, which can potentially help to understand their

distinctive contribution against corrosive environment after the immersion tests. The spectrometer equipped with electron flood source (CN 10 scientaomicron) provided charge neutralization, and argon ion sputter gun (NGI 3000 LK Tech) cleaned the sample surface. The analyzer was operated in fixed analyzer transmission (FAT) mode with pass energy of 20 eV for the high-resolution spectra of Al 2p and Mg 2p. The binding energies used in this study were calibrated to the binding energy of the carbon C 1s peak (285.0 eV), and the identification of peak was referenced based on the literature data.

The depth profiles of the main elements were obtained using the glow discharge optical emission spectrometer (GDOES, Horiba GD-Profiler 2) before and after the HPF process. The element profiles obtainable from the GDOES analysis can allow the layer estimation by elemental distribution. The area of 4 mm radius was analyzed with an applied 35 W power source under 600 Pa Argon pressure.

5.2.3. Electrochemical Measurements

To compare the barrier performance against the corrosion for the coating with different chemical compositions, the samples were immersed in a 0.1 M sodium chloride (NaCl) electrolyte. The electrochemical impedance spectroscopy (EIS) measurements were conducted for 10 days at open-circuit potential (OCP) using a potentiostat (Gamry Reference 1000E). A three-electrode electrochemical cell was used at room temperature, and the sample after HPF, graphite, and saturated calomel electrode (SCE) were served as working, counter, and reference electrodes, respectively. The measuring frequency range

of the impedance signal was from 100 kHz to 10 mHz, and 10 logarithmically spaced frequency points were measured for each decade with an amplitude of 10 mV rms.

5.3. Results and Discussion

5.3.1. Visual Inspection Before and After the HPF Process

Figure 5.2 represents the optical microscopic images before and after the HPF process. After the HDA process, all types of coating represent an aluminum-like color representation, indicating the dominating element at the top-most surface would be aluminum. Such would be due to the short heat treatment, therefore the other elements may not have enough time to diffuse toward the top-most surface. Meanwhile, after the HPF process, the surface of the samples tends to reveal more darker colors, especially noticeable in the conventional Al-Si coating system. As more of Mg element was added, the surface color tended to show toward a lighter blue color, and this represents the difference in the Al-Si-Mg coating system rely on the amount of Mg element, in terms of the microstructural coating formation which can also affect the anti-corrosion performance when such coatings are exposed to corrosive electrolytes.

5.3.2. Morphology Changes Before and After the HPF Process

The scanning electron microscopy (SEM) images obtained from the coatings with different chemical compositions are illustrated in Figure 5.3. Before the HPF process, also described as post-HDA, all types of samples showed distinct layer formations which can be recognized as Al-Si matrix, interdiffusion layer, and substrate, respectively, as

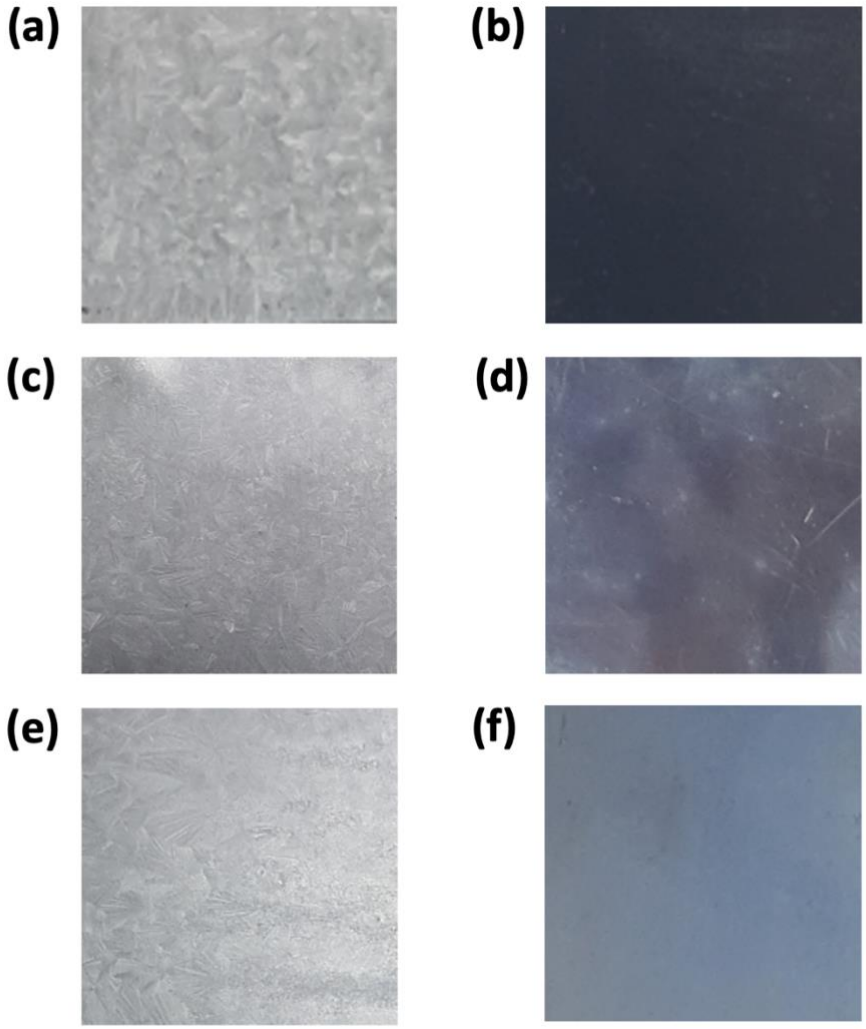

Figure 5.2. Optical micrographs of the Al-Si (a→b), Al-Si-0.1Mg (c→d), and Al-Si-0.5Mg (e→f) coatings before and after HPF at 930°C for 300 seconds.

illustrated in Figure 5.3a,d,g which is in a good agreement compared to the previous studies [5,6,10]. The thickness of the coatings after HDA was in a similar range, 15-18 μm, which possibly attribute to the wiping system that controls the thickness of the coating purposefully. Nevertheless, a thicker interdiffusion layer is observable as the Mg is introduced in the HDA process. This implies that the added Mg counteracted the role of

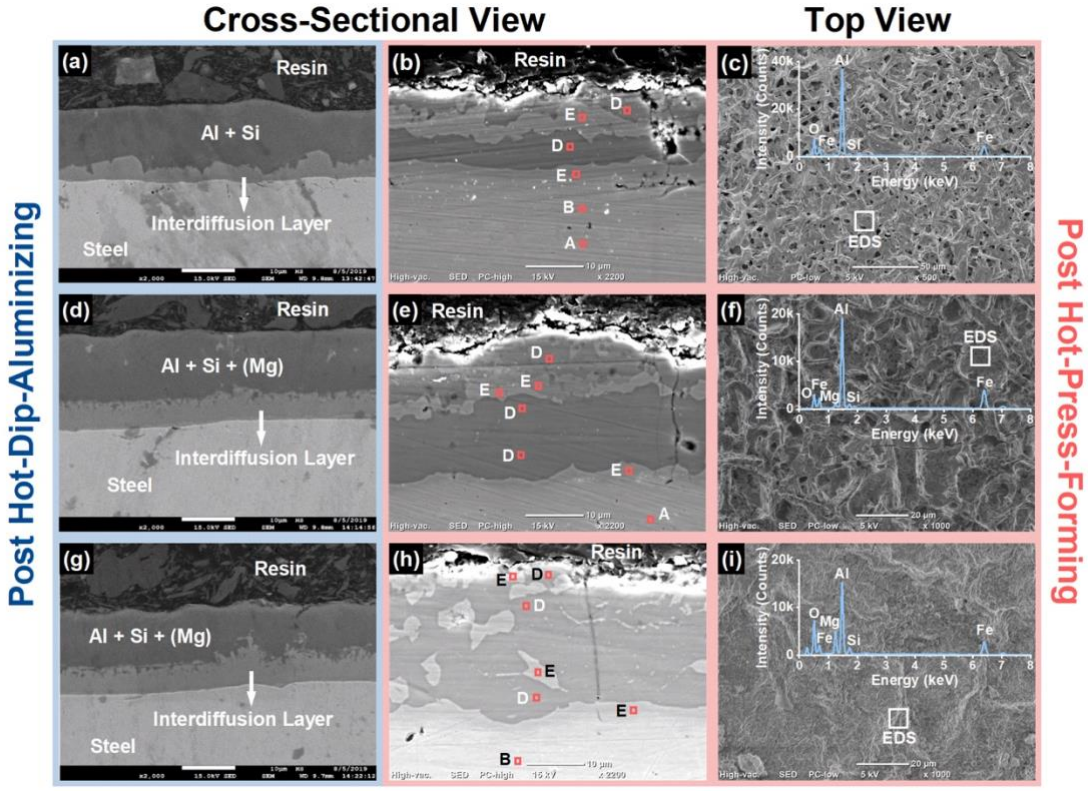

Figure 5.3. SEM micrographs with EDS analysis of the Al-Si (a-c), Al-Si-0.1Mg (d-f), and Al-Si-0.5Mg (g-i) coatings before and after HPF at 930°C for 300 seconds. The designated letter regions are in accordance with the Figure 5.4.

Si in the formation of interdiffusion layer, since such layer is known to prevent both the over diffusion of Fe and over invasion of Al and Fe-Al phases [3], the addition of Mg may have resulted in an enhanced Fe diffusion even before the HPF process.

According to Figure 5.3b,e,h, there were some noticeable structural changes after the HPF process that contains the heat treatment at 930°C for 300 seconds followed by press and water quenching. Such changes can be attributed to the thermal treatment under air condition that potentially enhanced mobility of the elements, especially Fe and Mg toward O at top-most surface. Compared to the Al-Si coating shown in the Figure 5.3b,

thicker coating formation with disappearing layered structures are observable when more of the Mg element was added. It is also noticeable that the silicon-rich layer, shown as Region E, at the middle of the coating matrix has diminished by thinning then finally formed an island-type coating over the increased Mg element. Additionally, the total coating thickness was shown to be increased, mostly by expansion of Region D, even when even a small amount of Mg was added into the coating process. The thickness of the coatings was measured as 25-27, 36-40, and 37-40 μm for each coating of Al-Si, Al-Si-0.1Mg, and Al-Si-0.5Mg, respectively. The possible coating thickening mechanisms will be discussed in a later section. Meanwhile, it is known that the heat treatment of aluminized coating can occur the accumulated Kirkendall pores in between coating and substrate which results in the delamination of coating [24], which was not the case for this study.

As shown in the figures, each layer or spot is designated with the capital letters following ternary Fe-Si-Al phase diagram that previously suggested [5], which are shown in Figure 5.4. Such a phase diagram well summarizes the observed results from the previous studies [4,25,26] obtained by SEM-EDS microstructural analysis. It should be marked that such compositional analysis obtained neglects the nonequilibrium thermodynamics since each region can have several phases, and the nonstoichiometric structural compositions are neglected, thus there might be a limitation in estimating the exact composition of each element [5]. According to Figure 5.4, it is clear that the coating compounds after the HPF process have mostly belonged to Region B, C, D, and E, where each includes Fe-Si-Al solid solution, FeAl, Fe_2Al_5/$FeAl_2$, and Fe_2SiAl_2, respectively,

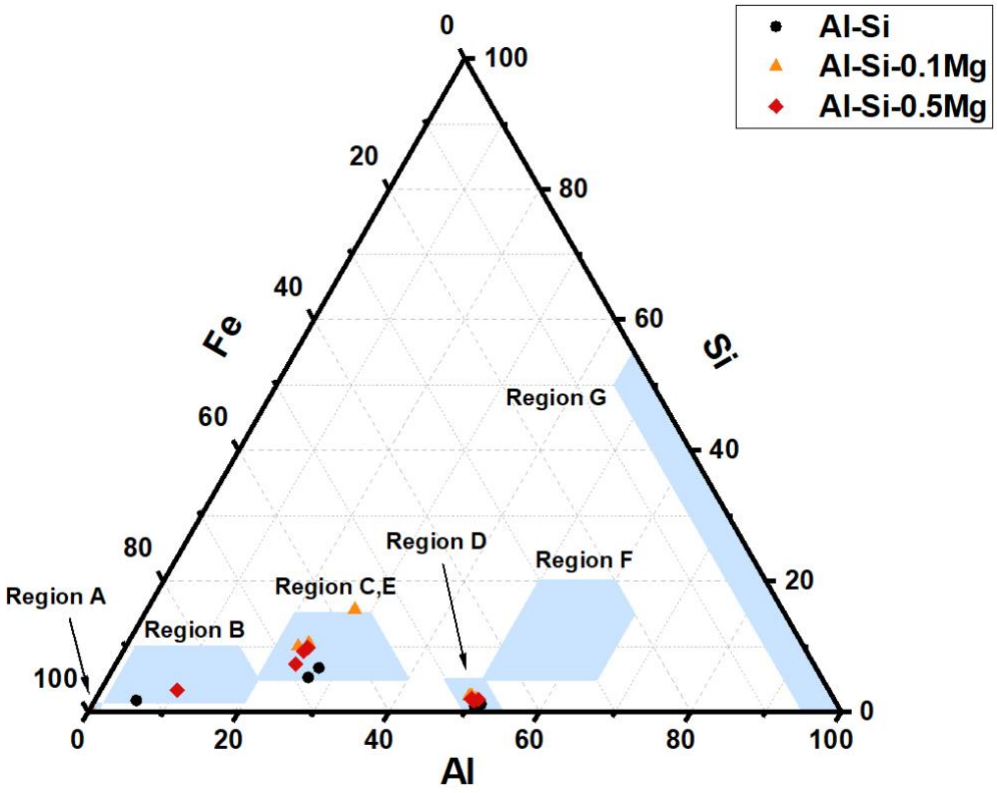

Figure 5.4. EDS map that shows compositional range for each region in Figure 5.3 by weight percent.

while the compounds prior to HPF are observed in Region F and G that includes Fe_2SiAl_7 and Al-Si solid solution, respectively.

After the HPF process, the Si-rich compounds in all types of samples are found have belonged to Region E. In such region, the higher Si concentration is observed in Mg-added samples which can be related to the thinning of Si-rich layer by adding Mg element which resulted in the formation of layer or island with higher Si concentration which corresponds to Figure 5.3b,e. Additionally, the decreased Al concentration in such region is also indicative of the more preferable reaction between Al and Fe element to form more

abundant Region D products that include Fe_2Al_5, which is shown to be a predominant compound of the Al-Si-Mg coating in Figure 5.3e,h.

Meanwhile, the top-view SEM figures shown in Figure 5.3c,f,i represent the modified top-most layers by adding the Mg element. Specifically, the microvoids that can be seen from the surface of conventional Al-Si coating system tended to be filled as the Mg was introduced up to 0.5 wt.%. Such surface modification with a void-filling effect triggered by adding a specific Mg element can possibly delay the water uptake by more compact coating surface formation which may results in an enhanced barrier protection. The EDS results imply that the surface chemical compositions of the reference Al-Si coating are mostly Al and O, while more of Mg element is detected at the surface level with an increased intensity, which is indicative of the Mg segregation toward the top-most surface. Considering the designed ratios of Mg were only 0.1 and 0.5 wt.%, the observed 2.66 wt.% and 10.47 wt.% of Mg at the surface level for each sample obtained by SEM-EDS (quantitative results are not shown) well represents the occurrence of Mg surface segregation during the HPF process.

5.3.3. Effect of Mg Addition on Coating Chemical Compositions and Coating Thickening Effect

The aforementioned structural changes triggered by introducing a low amount of Mg into the Al-Si coating system can possibly be explained by Mg segregation effects driven by enhanced diffusivity towards oxidation at higher temperature conditions [20–22,27]. To confirm and study more precisely of the Mg enrichment by segregation effect,

the XPS analysis was performed as shown in Figure 5.5. Such analysis identified the surface elements and compounds existing at the top-most coating surface. The Al 2p spectra of the samples are shown in Figure 5.5b, representing dominant contribution of aluminum oxides that include Al_2O_3 at 72.9 eV and 75.0 eV, respectively [28,29]. In addition to the existence of the native aluminum oxides, the Mg 2p spectra of the Mg-added samples are indicative that the surface is composed of a considerable amount of Mg

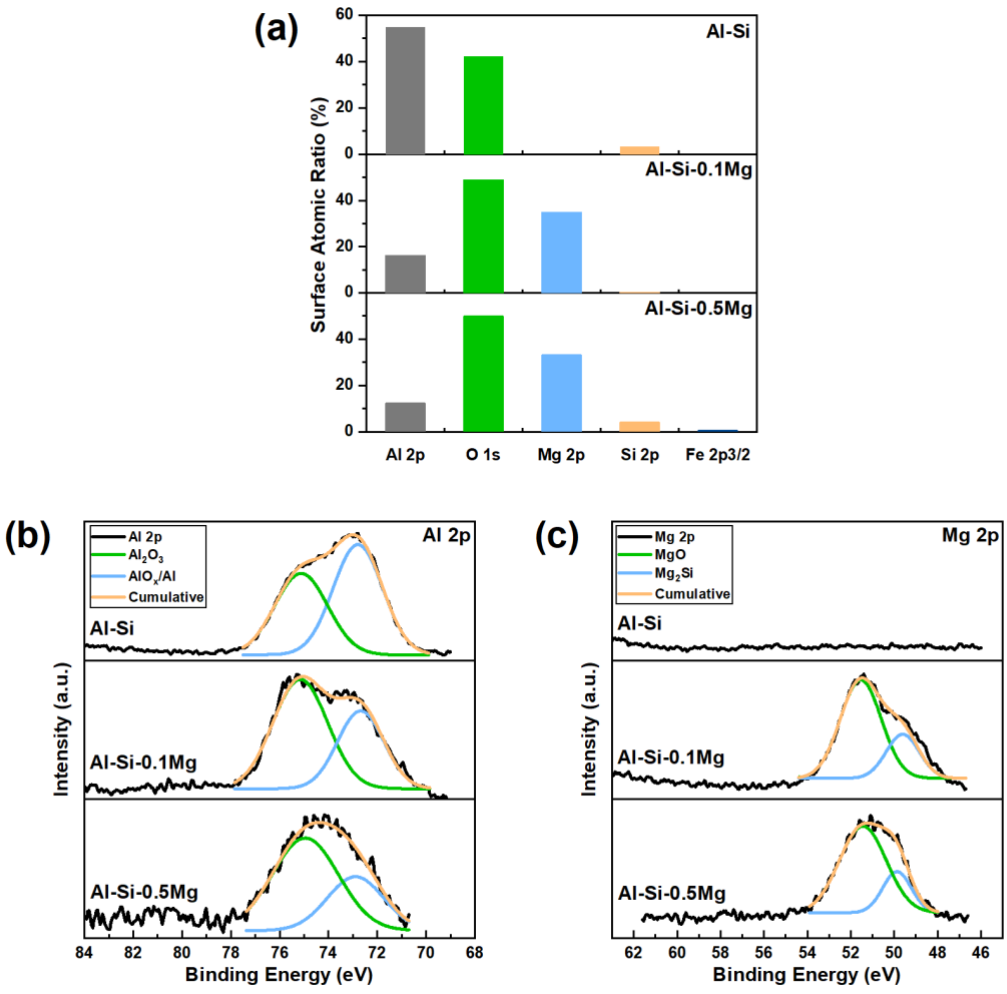

Figure 5.5. Elemental analysis (a) and high-resolution spectra (b-c) obtained by XPS study for different types of HPF coating samples prior to immersion test.

shown in Figure 5.5c, and such can be deconvoluted into MgO and Mg_2Si at 51.1 eV and 49.9 eV, respectively [30,31]. According to Figure 5.5a, the amount of Al element has been considerably decreased as the Mg was added, and this is illustrative of the stronger segregation tendency of Mg towards the oxygen during the press and water-quenching process which partially replaced the atomic ratio of the top-most surface. Indeed, compared to the reference Al-Si coating, the added Mg clearly segregated towards the top-most surface with the slightly increased O element that possibly depicts an existence of more oxides at surface level.

Among the Mg-based compounds, MgO was a predominant compound rather than Mg_2Si for both samples, and Al-Si-0.5Mg showed slightly more amount of Si element which may depict more of the Mg_2Si can exist compared to the Al-Si-0.1Mg. Nevertheless, the Mg_2Si can be estimated as a minor compound for both samples, and such a lack of the Mg_2Si compound that is known to be able to provide cathodic protection [19] may reasonable to predict that there would be no considerable or long-lasting cathodic protection when the sample is immersed into an electrolyte. Hence, this analysis suggests the top-most coating surface is mostly covered with Al_2O_3 or MgO (when Mg is added) rather than the Fe-oxide family, regardless of the sample types.

Figure 5.6 shows the XRD results of the coatings after HPF at 930°C for 300 seconds. Among the different peaks from the samples that represent the existence of multiple intermetallic phases, the dominating peaks are observable at around 42 to 45° that in accordance with the Fe-Al or Fe-Si-Al phases and α'-Fe (martensite) (JPDF No. 29-0043, 45-120(4,5), 51-0891, 44-1293), which are in good agreement with the SEM-

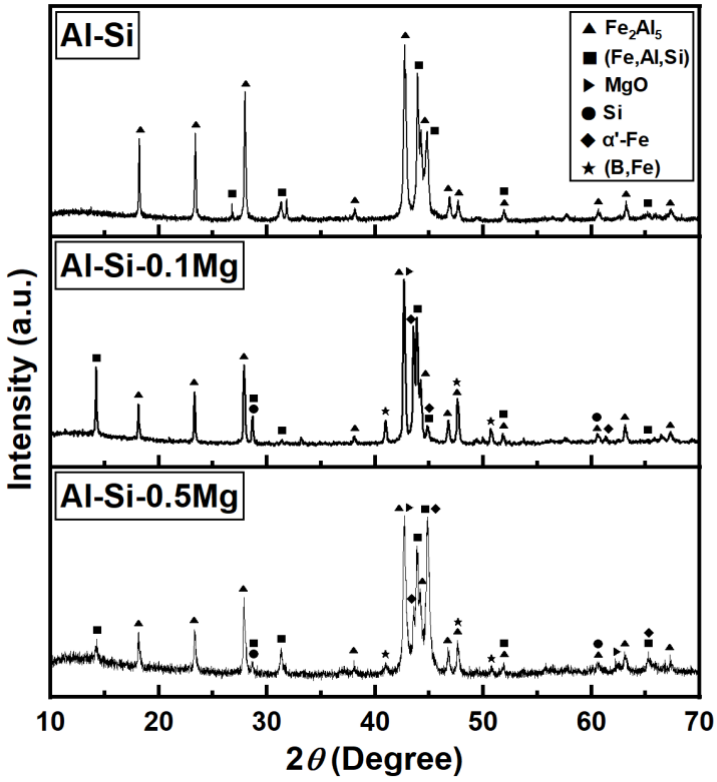

Figure 5.6. XRD patterns of the different types of HPF coating samples prior to immersion test.

EDS observations. Additionally, the Si-rich Fe-Si-Al phase has been detected at around 14.25° only from the Mg-added samples, and such agrees with the results shown in Figure 5.4 which revealed higher silicon content in region E. The presence of MgO is also captured when Mg element was added (JPDF No. 75-1525). The peaks for Mg_2Si phase were not recognizable, estimated due to its minor presence from small amount Mg addition.

A coating thickening effect was observed with the addition of Mg element. Such effect is inevitably related to the addition and segregation of Mg element which was the sole varying parameter in this study. The tendency of Mg segregation has been observed

from the HDA process which normally performed at or slightly over 650°C, and the addition of small amount of Mg counteracted the diffusion inhibiting effect of Si [32] by thickening the interdiffusion layer as more of Mg was added in the melting pot for the HDA process. The segregation tendency of Mg in Al-Mg system to reduce the free energy of the system [33,34] or to relieve the stress occurred by impurity size effect [35–37], can possibly help with the Fe diffusion even from the HDA process shown in Figure 5.3a,d,g. The thickened diffusion layer by adding Mg may stand for the weakened diffusion inhibiting performance of such layer, which may have allowed more reactions between Al and Fe at the same heat treatment time frame during HPF that resulted in thicker coatings. Another possible approach can include the enhanced Fe diffusivity by vacancy diffusion via Mg at high temperature heating, as Mg has lower vacancy formation and migration energy compared to those of Al [38]. When more of Fe is diffused towards the surface, more reaction between the Fe and Al can be occurred, resulting in a thinning of Si-rich layer with a decreased Al content (shown in Figure 5.4 Region E) and a thickening of the whole coating with the thickened $FeAl_2/Fe_2Al_5$ layer.

The GDOES results before and after the HPF are shown in Figure 5.7. Prior to the HPF or Post HDA, it is shown that the added Mg partially segregated as noticeably shown in Al-Si-0.5Mg sample. Such partial segregation of Mg triggered the expanded interdiffusion layer by allowing increased Fe interdiffusion. Considering the short period of HDA that performed for 3 seconds, the thickened diffusion layer is noteworthy along with the partial Mg segregation shown in Al-Si-0.5Mg sample at Figure 5.7e. Compared to the Al-Si-0.5Mg, the elemental distributions of Al-Si-0.1Mg indicated the tendency of

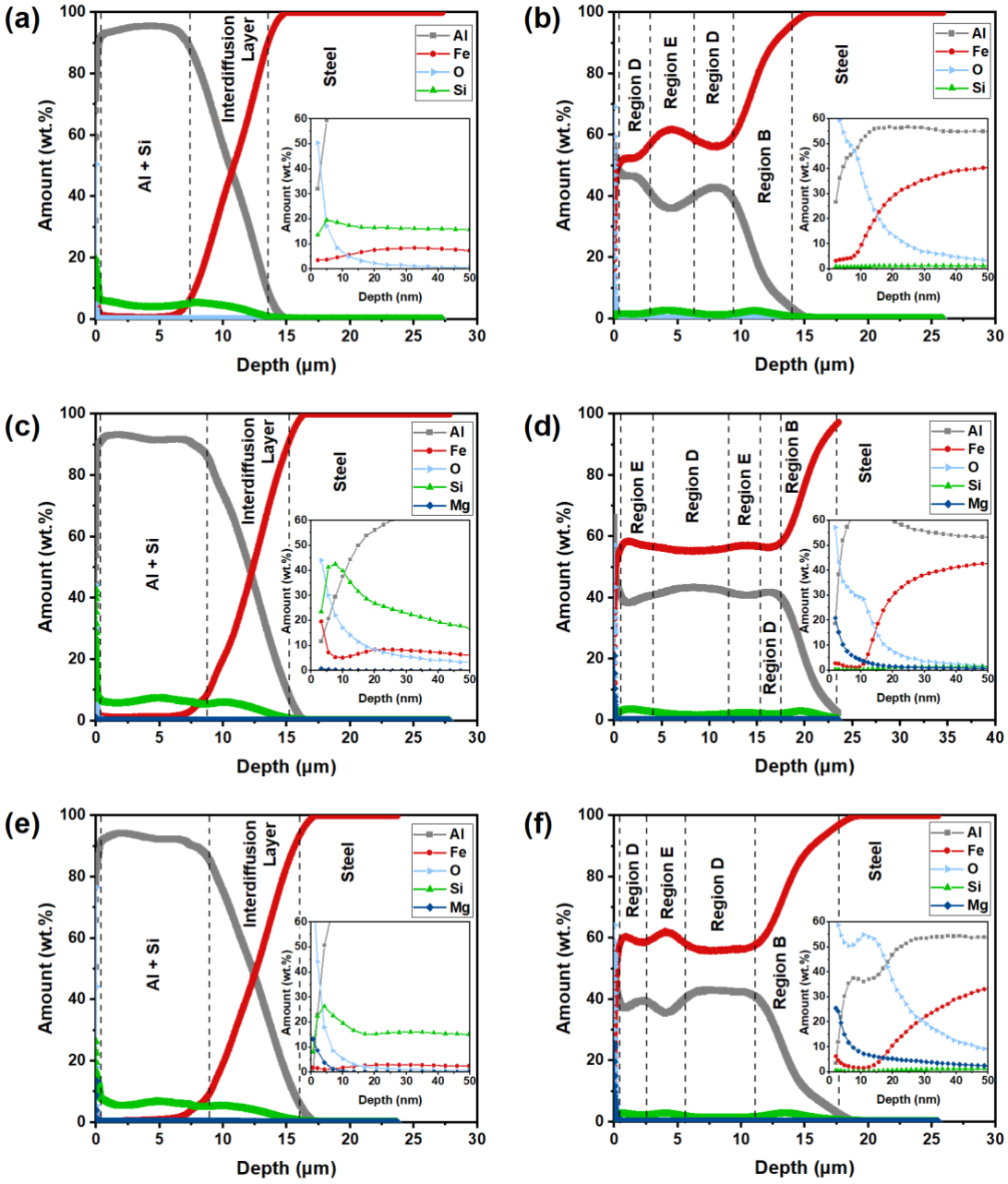

Figure 5.7. GDOES sputter depth profile before and after HPF coatings of Al-Si (a→b), Al-Si-0.1Mg (c→d), and Al-Si-0.5Mg (e→f).

Mg segregation at the top-most surface even before the HPF, but the trend is not clear which may attribute to the small amount of Mg added.

However, more clearer Mg segregation behavior was observed for both Mg-added samples after HPF process as illustrated in Figure 5.7d,f. Such figures evidence that the prolonged high temperature heat treatment can induce more of the Mg segregation towards the top-most surface. It is also shown that the induced Mg segregation triggered element replacement at the top-most surface from Al and O to Mg and O. It is clear that such results are in good agreement to the XPS results, that revealed the segregated Mg exists as MgO more dominantly. Meanwhile, a relatively thicker oxide scale is observable in Al-Si-0.5Mg system after HPF process. Considering the high-temperature oxidation during HPF process under air condition [39,40], the MgO formed at the top-most surface of Al-Si-0.5Mg may have allowed an enhanced intrusion of O^{2-} anion compared to that through the Al_2O_3 formed at the Al-Si surface. The GDOES results also represent the Mg-added samples formed the thickened coating with relatively more uniform Fe distribution compared to the reference Al-Si coating. The element stoichiometry of the GDOES may not distinctively indicate the compound of the layer by the winding layers or island type inter-coating formation. Nevertheless, it is clearly shown that the introduced Mg occurred the increased diffusion of Fe elements throughout the coating matrix together with the Mg segregation in both HDA and HPF process.

Meanwhile, it can be estimated that even such increased Fe element did not trigger the introduction of new inter-coating compound that does not exist in the reference Al-Si coating, but caused more voluminous compounds of $FeAl_2$, Fe_2Al_5, and the Fe-Si-Al intermetallic compounds that belong to Region B and D. Between such regions, the thickened compounds that belong to Region B as shown in Figure 5.7f, can enhance the

barrier property against corrosion since such region is known to be soft enough to arrest the microcracks [3]. Nevertheless, in order to fully understand the coating thickening effect, further studies are needed regarding the diffusion activation energy and vacancy formation/migration energy in Fe-Si-Al-Mg system.

5.3.4. EIS Study in 0.1 M NaCl Solution

To achieve information about the surface properties over the testing period, the EIS was performed for the different coatings in a 0.1 M NaCl solution. Such electrolyte was chosen to trigger relatively mild corrosion compared to the seawater (~3.5 wt.%), which allows to observe the corrosion responses of the coatings in a slower manner. Figure 5.8 shows both Nyquist and Bode plots for each type of coating.

Figure 5.8a,c,e shows the Nyquist plots for each Al-Si, Al-Si-0.1Mg, and Al-Si-0.5Mg, respectively. It is observable that the bigger size of the semicircle was obtained from the Mg-added samples at the early period of immersion. This can be attributed to the more compact coating formation achieved by the segregation of the added Mg element, according to Figure 5.3, that may have constrained an early-period active charge transfer reaction represented by higher impedance values compared to Al-Si at LF. Meanwhile, the samples tended to be degraded over the testing period represented by the decrease of semicircle diameter with its depressed shape. Such degradation of the coatings is possibly accelerated by water uptake through the pre-existing microvoids or microcracks from the surface level. More porous surfaces can allow more water uptakes that possibly trigger a

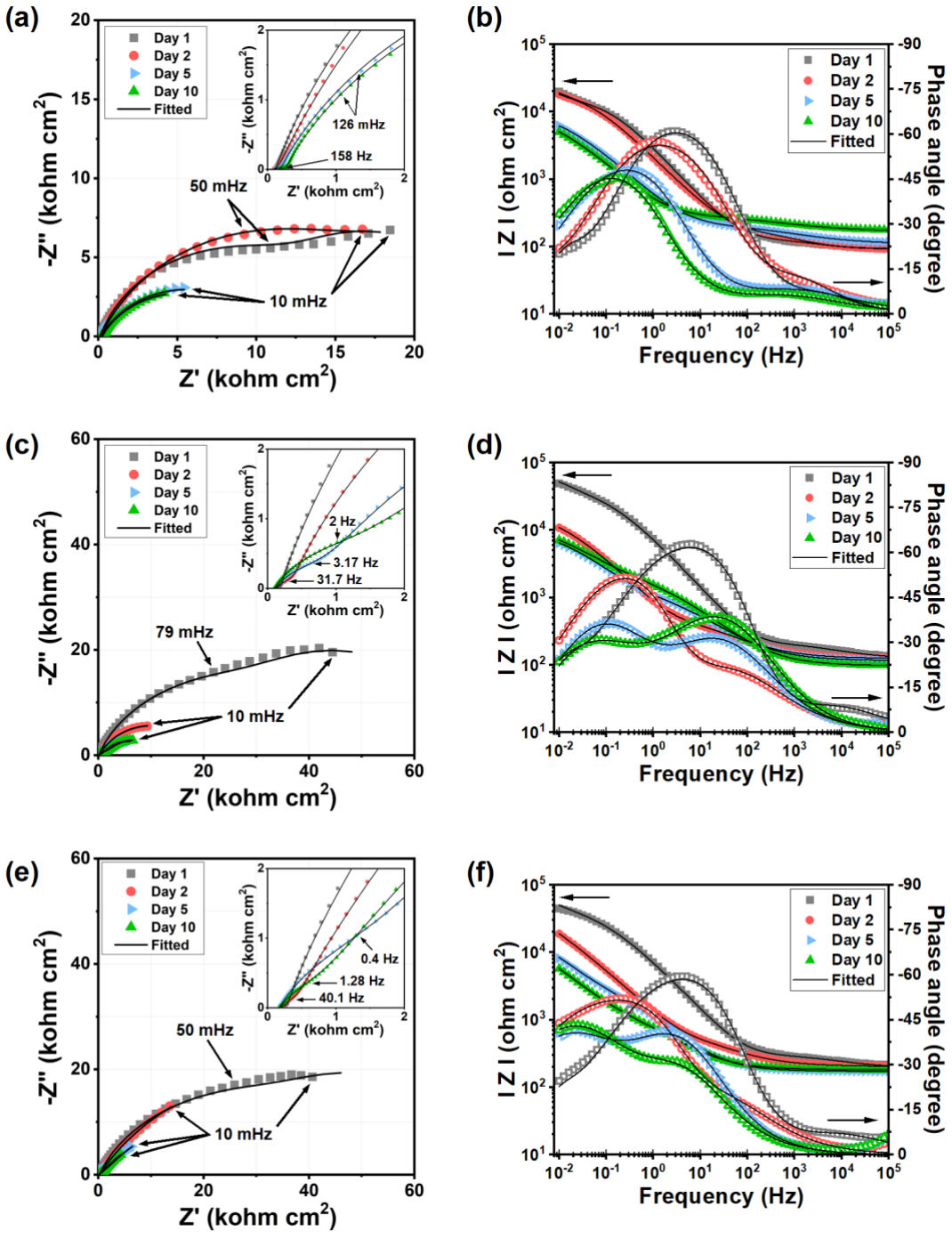

Figure 5.8. Nyquist and Bode plots for the immersion tests in 0.1 M NaCl for HPF coatings of Al-Si(a-b), Al-Si-0.1Mg (c-d), and Al-Si-0.5Mg (e-f).

more accelerated corrosion process. Compared to the Al-Si and Al-Si-0.1Mg, the Al-Si-

0.5Mg maintained a relatively bigger semicircle with less depressed shape, and this can be attributed to the more void-filled surface structures which were observable according to Figure 5.3i. Additionally, the thicker crack-free layer of Al-Si-0.5Mg, shown by GDOES results in Figure 5.7f, can also contribute to relatively bigger impedance values compared to other samples at the same immersion time.

Meanwhile, Figure 5.8b,d,f shows the Bode plots for the samples. Throughout the experimental period, the samples revealed two time-constants (TCs) which can be considered as a contribution of coating and charge transfer, respectively. It is also observable that there was a diffusion regime that disappeared after the early immersion period (day 1 or 2) which means the other elements, such as coating pore resistance or charge transfer resistance played more dominant roles after the initial immersion period in the corroding system.

During the immersion testing period, the differences in phase shifts for each coating type are also notable. The 2 TCs of Al-Si sample that initially located at high-frequency (HF) and mid-frequency (MF) range, respectively, were shifted towards lower frequency over time. In addition, the gradual decrease of the phase peak of TC at MF is observed over time with shifting to low-frequency (LF) which can be caused by continued water penetration represented as a diminishing phase angle of the TC at HF that moved to MF at last. This can be explained by the microvoids existing in a coating, where the existing pores might have bigger size than its effective pore size which could provide a barrier effect by filling the pores with corrosion products. As a result, the size of the

semicircle at HF shown in the inset Nyquist plot of Figure 5.8a have almost unchanged over the testing period.

Meanwhile in the Mg contained coating system, there similar shifts of TCs from HF and MF to MF and LF, respectively over the immersion period. The observable phase evolution at MF that is in accordance to the first semicircle assigned to coating, is representative of the coating which pores filled with corrosion products. Thus, it can be estimated that such accumulation of corrosion product in the Mg-added samples have resulted in the evolution of the coating impedance shown in the inset Nyquist plot of Figure 5.8c,e. As the coating impedance does not increase monotonically, such corrosion products may be considered as semi-protective which may allow the re-penetration of water by prolonged immersion.

Two electrical equivalent circuit (EEC) models are suggested as shown in Figure 5.9 to provide effective parameters quantitatively in the corroding system. The impedance spectra that included the diffusion regime were fitted with the EEC shown in Figure 5.9a, and the others were fitted with the EEC shown in Figure 5.9b. The EECs included elements, namely, the solution resistance (R_s), coating pore resistance (R_c), charge transfer resistance (R_{ct}), capacitance in terms of the constant phase element (CPE), coating capacitance (Q_c), double-layer capacitance (Q_{dl}), and finite-length Warburg impedance (Z_D) which is composed of Warburg diffusion resistance (W_R) and Warburg time constant (W_T) for the diffusion of metal cations and oxygen ions which have been limited by the presence of coating. The CPE concept was introduced to represent the depressed impedance semicircles, which is known to be occurred from the physical property

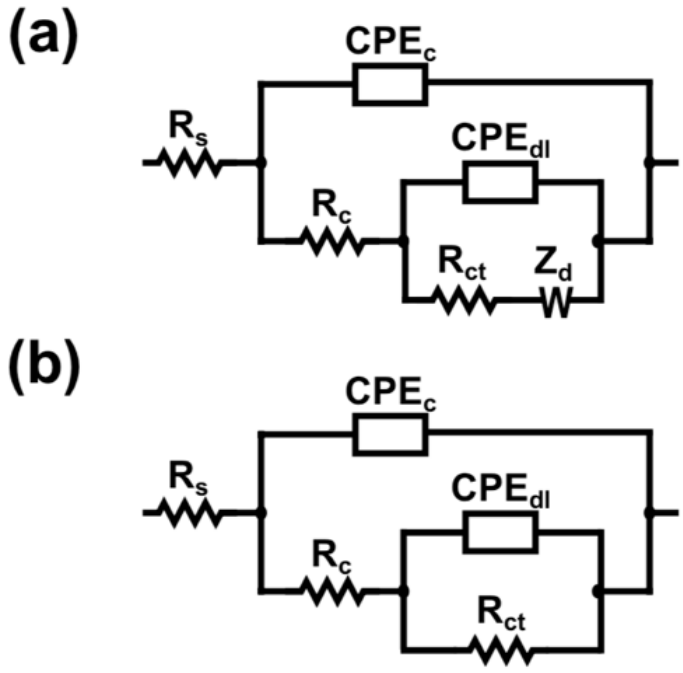

Figure 5.9. Schematic representation of the corresponding electrical equivalent circuits used for fitting the experimental EIS results with (a) and without (b) the diffusion regime.

distributions that can result in the time constants distributions [41]. The double layer capacitance, C_{dl}, can be described using a formula proposed by Brug et al. [42]:

$$C_{dl} = Q^{1/\alpha}(1/R_e + 1/R_t)^{(\alpha-1)/\alpha} \quad (5.1)$$

where Q is CPE capacitance, $0 < \alpha \leq 1$ is model parameter, and R_e / R_t as electrolyte/charge transfer resistance, respectively.

The quantified impedance parameters obtained from the aforementioned EECs are described in Table 5.2. At the initial immersion period, all samples experience diffusion regime, and such is illustrative of the limited mass transport of metal cations and oxygen ions by the presence the coating which may have dominated the corrosion kinetics during

Table 5.2. Impedance parameters for the corrosion of HPF steels in 0.1 M NaCl.

Material ID	Time (day)	R_c ($\Omega\, cm^2$)	Q_c ($F\, cm^{-2}\, s^{n-1}$)	α_c	R_{ct} ($\Omega\, cm^2$)	Q_{dl} ($F\, cm^{-2}\, s^{n-1}$)	α_{dl}	C_{dl} ($F\, cm^{-2}$)	W_R ($\Omega\, cm^2$)	W_T (s)	R_p ($\Omega\, cm^2$)	χ^2
Al-Si	1	3.7×10^{1}	1.5×10^{-5}	0.76	1.4×10^{4}	6.4×10^{-5}	0.78	1.5×10^{-5}	1.1×10^{4}	35	2.4×10^{4}	3.3×10^{-2}
	2	8.6×10^{1}	3.4×10^{-5}	0.69	1.9×10^{4}	9.4×10^{-5}	0.72	1.6×10^{-5}	6.6×10^{3}	65	2.6×10^{4}	3.9×10^{-2}
	5	1.1×10^{2}	1.9×10^{-4}	0.48	1.1×10^{4}	3.9×10^{-4}	0.73	1.2×10^{-4}	-	-	1.1×10^{4}	9.3×10^{-3}
	10	1.7×10^{2}	2.3×10^{-4}	0.46	1.1×10^{4}	5.9×10^{-4}	0.73	2.5×10^{-4}	-	-	1.1×10^{4}	8.7×10^{-3}
Al-Si-0.1Mg	1	1.0×10^{2}	2.3×10^{-5}	0.59	4.4×10^{4}	1.3×10^{-5}	0.86	4.9×10^{-6}	2.9×10^{4}	27	7.3×10^{4}	3.3×10^{-2}
	2	4.9×10^{2}	2.0×10^{-4}	0.56	2.0×10^{4}	1.7×10^{-4}	0.83	7.8×10^{-5}	-	-	2.1×10^{4}	5.3×10^{-3}
	5	1.2×10^{3}	1.5×10^{-4}	0.60	9.0×10^{3}	4.3×10^{-4}	0.67	9.8×10^{-5}	-	-	1.0×10^{4}	7.7×10^{-3}
	10	1.9×10^{3}	1.1×10^{-4}	0.63	1.1×10^{4}	4.6×10^{-4}	0.58	5.8×10^{-5}	-	-	1.3×10^{4}	4.3×10^{-3}
Al-Si-0.5Mg	1	1.3×10^{2}	2.5×10^{-5}	0.55	5.2×10^{4}	1.5×10^{-5}	0.84	5.1×10^{-6}	2.5×10^{4}	40	7.7×10^{4}	5.9×10^{-2}
	2	6.6×10^{2}	1.8×10^{-4}	0.57	7.8×10^{4}	7.7×10^{-5}	0.80	2.8×10^{-5}	-	-	7.9×10^{4}	1.4×10^{-2}
	5	2.8×10^{3}	2.3×10^{-4}	0.67	2.9×10^{4}	4.8×10^{-4}	0.63	1.1×10^{-4}	-	-	3.2×10^{4}	1.1×10^{-2}
	10	1.3×10^{3}	3.5×10^{-4}	0.62	2.3×10^{4}	6.2×10^{-4}	0.64	1.8×10^{-4}	-	-	2.4×10^{4}	1.0×10^{-2}

such period [43]. Such phenomena can correspond to the finite-length Warburg impedance at last [44]. Meanwhile, relatively higher R_{ct} values are observable from the Mg-added samples which are originated from their more compact coating formation prior to the severe water uptake through the microcracks. Compared to Al-Si-0.1Mg, the Al-Si-0.5Mg revealed a more delayed decrease of R_{ct} values which can be attributed to the structural effects including both less porous surface and thicker crack-free diffusion layer as shown in Figure 5.3i,f, respectively. Similarly, higher values of coating pore resistance, R_c, were also obtained from the Mg-added samples throughout the period. While the R_c values were maintained relatively higher in the Mg containing samples over the prolonged immersion, the polarization resistance values of the samples were tended to decrease similar to the Al-Si coating, which can be triggered by the decreased R_{ct} of the substrate from continued charge transfer reactions. The increasing trend of C_c values over the testing period is observable for every sample. This implies that the water supplied from the immersed condition was penetrated to a deeper part of the coating, even with the presence of the corrosion products which may have played only a semi-protective role versus the water uptake.

5.3.5. Post-Immersion Characterization

The cross-sectional SEM images obtained after the corrosion testing for each type of coating with different chemical compositions are shown in Figure 5.10. According to the general corrosion regime shown by the tested samples, it is noticeable that the coating itself did not provide enough cathodic protection, rather estimated that most corrosion was

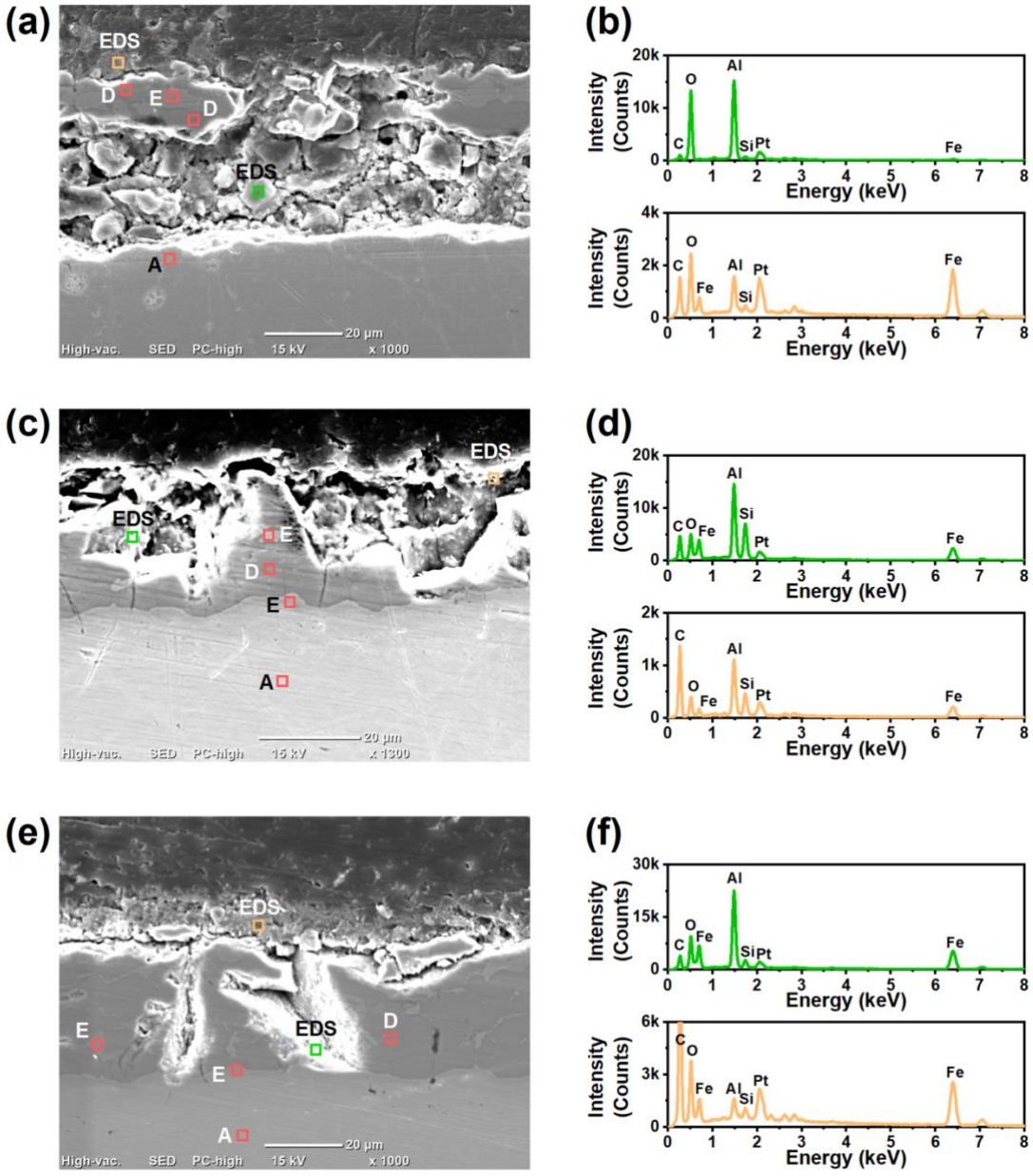

Figure 5.10. SEM micrographs with EDS analysis after the corrosion testing of the HPF coatings. Al-Si (a-b), Al-Si-0.1Mg (c-d), and Al-Si-0.5Mg (e-f).

triggered following the existing microcracks or microvoids. In general, it is possible that the water penetrated through such coating defects, and the coating dissolution occurred simultaneously. When the metallic coating dissolves, it can trigger a bigger water coverage

area that enlarges the defect not only deeper but also wider throughout the coating horizon. Figure 5.10a represents the reference Al-Si coating system that shows the invaded and dissolved substrate with abundant corrosion products while its part of the coating was kept intact with maintained layered structure. The severe degradation of the middle zone of the figure can be triggered by pre-existing microcracks, and it is also observable that degradation regime at the soft layer (Region B) and the substrate (Region A) would have uniform corrosion.

A similar coating degradation process was observable in the Mg-added samples, shown in Figure 5.10c,e, as the degradation occurred mostly through the existing defects. Nevertheless, compared to the reference Al-Si coating system, the damage was less severe at the Mg-added ones which can be explained by the aforementioned structural changes with the surface modification that helped to delay water uptake. Considering these metallic coatings are commonly used as a primer before the electrodeposited (ED) coating [45], such these water-uptake delaying factors can also contribute to enhancing the anti-corrosion performance dramatically with an applied ED layer on top of it.

The elemental analyses provided for each sample are indicative of either Fe- or Al-rich oxide complexes. More detailed specifications of the corrosion products are provided in the next section. Meanwhile, it is noticeable that there are the region indicators for the part of the well-preserved coating (red markers, EDS are not shown in the Figure) that illustrates coating/substrate degradation dominantly occurred following the existing defects with a lack of cathodic protection.

Figure 5.11 illustrates the estimation of the corrosion products obtained by XRD spectra. For all types of the samples, it was figured out that the γ-FeO(OH) (lepidocrocite, JPDF No. 74-1877) was the dominating corrosion products from the immersion testing with the minor presence of α-FeO(OH) (goethite, JPDF No. 29-0713). The dominating corrosion product, γ-FeO(OH), has been known to be thermodynamically less stable compared to other iron hydroxide phases, such as α-FeO(OH) or β-FeO(OH) [46,47]. Thus, the γ-FeO(OH) formed during the immersion test can be either dissolved or transformed into more stable phases in a longer period immersion. In this case, the α-FeO(OH) produced can be due to the transformation of the initial corrosion product, γ-

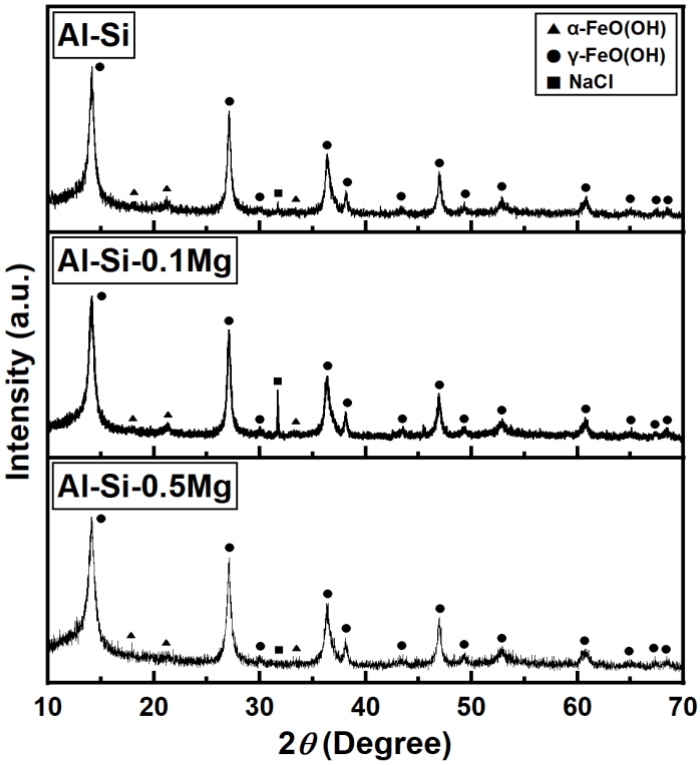

Figure 5.11. XRD patterns of the different types of HPF coatings after immersion test.

FeO(OH). Moreover, γ-FeO(OH) has been known to have a flowery structure [48]. These features depict that the formation of such product can only provide a short-term protection even though it can fill up the micropores in coating by accumulation. The Al- and Mg-based corrosion products were hard to detect in this corrosion product analysis. Their corrosion products, such as AlO(OH), $Al(OH)_3$, and $Mg(OH)_2$ may have formed during the immersion test, but it is estimated that their relative quantity compared to the Fe-based corrosion products were negligible due to the abundant formation of Fe-based corrosion products.

The corrosion products formed may have helped with enhancing the barrier performance temporarily, especially in the early period of immersion, but such products typically cannot provide a long-term barrier protection unless they completely fill the cracks or damaged area, thus allowing a repeated water uptake over the period [49,50]. Meanwhile, it is observable that there is no distinct difference in corrosion product types among the samples, and this possibly depicts that there was no considerable difference in the electrochemical reaction pathways, but only difference observed was in the level of coating degradation, represented by both polarization resistance and corrosion rate which may ascribed to the coating morphology formed during the HPF process.

5.4. Summary

This study described the corrosion behavior of the Al-Si-Mg coated HPF boron steel. When Mg was added, there was a thicker interdiffusion layer formation even after the HDA process that is indicative of the Mg segregation during the HDA process. The

followed heat treatment during the HPF process, at 930°C for 300 seconds, have accelerated the Mg segregation which may counteracted the inhibiting interdiffusion layer. Therefore, when Mg exists the enhanced reaction between Al and Fe may have triggered the expanded Region B and D compared to that of the reference Al-Si coating. Along with the thickening trend of the Al-Si-Fe intermetallic layer which was observed with an increasing Mg amount, the visualized surface image by SEM depicted the more compact surface structures of Mg-added samples, especially in Al-Si-0.5Mg sample, compared to the surface of the reference Al-Si coating which showed highly porous surface structures. The element depth profile obtained by the GDOES study revealed the segregation of Mg at a surface level as well as the thickened crack-free region that potentially contributed to the longer substrate protection. The segregated Mg element was shown to exist as MgO and Mg_2Si which were confirmed by XPS and XRD studies.

The EIS results obtained during the early immersion period revealed that all samples experienced diffusion regime that governs concentration distribution of the metal and oxygen ions. Additionally, considerably higher impedance values were observed in Mg-added samples, especially during the early period of immersion. Such can be attributed to the formation of more compact top-most surface and thicker crack-free layer with the presence of Mg element. The electrochemical results demonstrated a more protective coating formation of the Mg-added samples, especially the Al-Si-0.5Mg sample was the one that showed a better anti-corrosion performance represented by the higher polarization resistance compared to that of the other samples.

Meanwhile, the prolonged immersion of the samples triggered the degradation of the samples at last. The cross-sectional SEM revealed the main corrosion pathway can be the pre-existing defects that include microcracks or microvoids, and the Al-Si-Fe intermetallic layer (Region B) and substrate (Region A) showed relatively more uniform corrosion regime. Followed XRD study that have revealed the corrosion products were to be γ-FeO(OH) and α-FeO(OH) for all samples, that may indicate that the addition of Mg did not change the electrochemical reaction pathways. Nevertheless, the structural changes triggered by adding Mg element have enhanced the coating's barrier protection which were attributed to more compact surface through the Mg segregation, pore filling effect by the accumulation of corrosion products even though they may not provide long-term protection, and the thicker crack-free layer formation with absence of microcrack propagation.

5.5. References

[1] E. Billur, Hot Stamping of Ultra High-Strength Steels, Springer, 2019.

[2] Y. Chang, Z. Meng, L. Ying, X. Li, N. Ma, P. Hu, Influence of Hot Press Forming Techniques on Properties of Vehicle High Strength Steels, J. Iron Steel Res. Int. 18 (2011) 59–63.

[3] D.W. Fan, B.C.D. Cooman, State-of-the-Knowledge on Coating Systems for Hot Stamped Parts, Steel Research International. 83 (2012) 412–433.

[4] R.W. Richards, R.D. Jones, P.D. Clements, H. Clarke, Metallurgy of continuous hot dip aluminizing, International Materials Reviews. 39 (1994) 191–212.

[5] F. Jenner, M.E. Walter, R. Mohan Iyengar, R. Hughes, Evolution of Phases, Microstructure, and Surface Roughness during Heat Treatment of Aluminized Low Carbon Steel, Metall and Mat Trans A. 41 (2010) 1554–1563.

[6] F.D. Wei, K.H. Soo, O.H. Jin-Keun, C. Kwang-Geun, D.C.B. C, Coating Degradation in Hot Press Forming, ISIJ International. 50 (2010) 561–568.

[7] M. Suehiro, J. Maki, K. Kusumi, M. Ohgami, T. Miyakoshi, Properties of aluminized steels for hot-forming, SAE Technical Paper, 2003.

[8] L. Dosdat, J. Petitjean, T. Vietoris, O. Clauzeau, Corrosion Resistance of Different Metallic Coatings on Press-Hardened Steels for Automotive, Steel Research International. 82 (2011) 726–733.

[9] D.W. Fan, B.C. De Cooman, Formation of an aluminide coating on hot stamped steel, ISIJ International. 50 (2010) 1713–1718.

[10] I. De Graeve, I. Schoukens, A. Lanzutti, F. Andreatta, A. Alvarez-Pampliega, J. De Strycker, L. Fedrizzi, H. Terryn, Mechanism of corrosion protection of hot-dip aluminium–silicon coatings on steel studied by electrochemical depth profiling, Corrosion Science. 76 (2013) 325–336.

[11] C.P. Couto, R.I. Revilla, M.A. Colosio, I. Costa, Z. Panossian, I. De Graeve, H. Terryn, J.L. Rossi, Electrochemical behaviour of 22MnB5 steel coated with hot-dip Al-Si before and after hot-stamping process investigated by means of scanning Kelvin probe microscopy, Corrosion Science. (2020) 108811.

[12] Y.-Y. Chang, C.-C. Tsaur, J.C. Rock, Microstructure studies of an aluminide coating on 9Cr-1Mo steel during high temperature oxidation, Surface and Coatings Technology. 200 (2006) 6588–6593.

[13] N. Takata, T. Tsukahara, S. Kobayashi, M. Takeyama, Microstructure control of dual-phase steels through hot-dip Al–Mg–Si alloy coating process, ISIJ International. 56 (2016) 319–325.

[14] N. Takata, M. Nishimoto, S. Kobayashi, M. Takeyama, Morphology and formation of Fe–Al intermetallic layers on iron hot-dipped in Al–Mg–Si alloy melt, Intermetallics. 54 (2014) 136–142.

[15] A.P. YADAV, A. NISHIKATA, T. TSURU, Effect of Corrosion Product on the Electrochemical Behavior of Zn, Zn-Al and Al-Mg-Si Alloy Coated Steel, Electrochemistry. 80 (2012) 218–221.

[16] N. Takata, M. Nishimoto, S. Kobayashi, M. Takeyama, Growth of Fe2Al5 phase on pure iron hot-dipped in Al–Mg–Si alloy melt with Fe in solution, ISIJ International. 55 (2015) 1454–1459.

[17] C. Kruehong, G.A. EL-Mahdy, A. Nishikata, T. Tsuru, Influence of second phases on the electrochemical behavior of hot dipped Al–Mg–Si coated steel, Corrosion Science. 52 (2010) 2379–2386.

[18] M. Yıldırım, D. Özyürek, The effects of Mg amount on the microstructure and mechanical properties of Al–Si–Mg alloys, Materials & Design. 51 (2013) 767–774.

[19] W. Liu, M.-C. Li, Q. Luo, H.-Q. Fan, J.-Y. Zhang, H.-S. Lu, K.-C. Chou, X.-L. Wang, Q. Li, Influence of alloyed magnesium on the microstructure and long-term

corrosion behavior of hot-dip Al–Zn–Si coating in NaCl solution, Corrosion Science. 104 (2016) 217–226.

[20] C. Lea, C. Molinari, Magnesium diffusion, surface segregation and oxidation in Al-Mg alloys, Journal of Materials Science. 19 (1984) 2336–2352.

[21] S.O. Saied, J.L. Sullivan, A study of thermally induced segregation of magnesium in aluminium-magnesium alloys by means of AES, J. Phys.: Condens. Matter. 5 (1993) A165–A166.

[22] H. Deng, W. Hu, X. Shu, B. Zhang, Analytic embedded-atom method approach to studying the surface segregation of Al–Mg alloys, Applied Surface Science. 221 (2004) 408–414.

[23] Z. Gui, W. Liang, Y. Zhang, Enhancing ductility of the Al-Si coating on hot stamping steel by controlling the Fe-Al phase transformation during austenitization, Science China Technological Sciences. 57 (2014) 1785–1793.

[24] M.C. Galetz, C. Oskay, S. Madloch, Microstructural degradation and interdiffusion behavior of NiAl and Ge-modified NiAl coatings deposited on Alloy 602 CA, Surface and Coatings Technology. 364 (2019) 211–217.

[25] M.V. Akdeniz, A.O. Mekhrabov, T. Yilmaz, The role of Si addition on the interfacial interaction in Fe-Al diffusion layer, Scripta Metallurgica et Materialia;(United States). 31 (1994).

[26] S.P. Gupta, Intermetallic compound formation in Fe–Al–Si ternary system: Part I, Materials Characterization. 49 (2002) 269–291.

[27] J. Guillot, N. Valle, E. Maitre, S. Verdier, H.-N. Migeon, Investigation on the magnesium segregation in low-magnesium aluminium alloys, Surface and Interface Analysis. 42 (2010) 735–738.

[28] Y.-C. Kim, H.-H. Park, J.S. Chun, W.-J. Lee, Compositional and structural analysis of aluminum oxide films prepared by plasma-enhanced chemical vapor deposition, Thin Solid Films. 237 (1994) 57–65.

[29] T.J. Carney, P. Tsakiropoulos, J.F. Watts, J.E. Castle, Oxidation and surface segregation in rapidly solidified aluminum alloy powders, International Journal of Rapid Solidification. 5 (1990) 189–217.

[30] X.D. Peng, M.A. Barteau, Spectroscopic characterization of surface species derived from HCOOH, CH3COOH, CH3OH, C2H5OH, HCOOCH3, and C2H2 on MgO thin film surfaces, Surface Science. 224 (1989) 327–347.

[31] M.R.J. Van Buuren, F. Voermans, H. VanKempen, Bonding in Mg2Si studied with x-ray photoelectron spectroscopy, The Journal of Physical Chemistry. 99 (1995) 9519–9522.

[32] S.K. Kim, Hot-Dip Aluminizing with Silicon and Magnesium Addition I. Effect on Intermertallic Layer Thickness, Korean Journal of Metals and Materials. 51 (2013) 795–799.

[33] C. Kittel, P. McEuen, P. McEuen, Introduction to solid state physics, Wiley New York, 1996.

[34] R.C. Picu, D. Zhang, Atomistic study of pipe diffusion in Al–Mg alloys, Acta Materialia. 52 (2004) 161–171.

[35] G. Wu, K. Dash, M.L. Galano, K.A.Q. O'Reilly, Oxidation studies of Al alloys: Part II Al-Mg alloy, Corrosion Science. 155 (2019) 97–108.

[36] D.T.L. Van Agterveld, G. Palasantzas, J.T.M. De Hosson, Magnesium surface segregation and oxidation in Al–Mg alloys studied with local probe scanning Auger-scanning electron microscopy, Applied Surface Science. 152 (1999) 250–258.

[37] F.J. Esposto, C.-S. Zhang, P.R. Norton, R.S. Timsit, Segregation of Mg to the surface of an Al-Mg single crystal alloy and its influence on the initial oxidation at room temperature, Surface Science. 302 (1994) 109–120.

[38] T. Angsten, T. Mayeshiba, H. Wu, D. Morgan, Elemental vacancy diffusion database from high-throughput first-principles calculations for fcc and hcp structures, New Journal of Physics. 16 (2014) 015018.

[39] C. Wagner, N.F. Mott, Z. phys. Chem., Ohio, American Society for Metals Metals Park, 1933.

[40] M.G. Fontana, Corrosion engineering, Tata McGraw-Hill Education, 2005.

[41] B. Hirschorn, M.E. Orazem, B. Tribollet, V. Vivier, I. Frateur, M. Musiani, Constant-Phase-Element Behavior Caused by Resistivity Distributions in Films I. Theory, J. Electrochem. Soc. 157 (2010) C452–C457.

[42] G.J. Brug, A.L. van den Eeden, M. Sluyters-Rehbach, J.H. Sluyters, The analysis of electrode impedances complicated by the presence of a constant phase element, Journal of Electroanalytical Chemistry and Interfacial Electrochemistry. 176 (1984) 275–295.

[43] S.P. Sah, Corrosion of 304 stainless steel in carbonates melt– a state of enhanced dissolution of corrosion products, Corrosion Science. 169 (2020) 108535.

[44] T.Q. Nguyen, C. Breitkopf, Determination of Diffusion Coefficients Using Impedance Spectroscopy Data, J. Electrochem. Soc. 165 (2018) E826–E831.

[45] W. Yang, E. Hwang, H. Kim, S. Ahn, S. Kim, H. Castaneda, A study of annealing time to surface characteristics and hydrogen embrittlement on AlSi coated 22MnB5 during hot stamping process, Surface and Coatings Technology. 378 (2019) 124911.

[46] R.M. Cornell, U. Schwertmann, The Iron Oxides: Structure, Properties, Reactions, Occurrences and Uses, John Wiley & Sons, 2003.

[47] H. Liu, P. Li, M. Zhu, Y. Wei, Y. Sun, Fe (II)-induced transformation from ferrihydrite to lepidocrocite and goethite, Journal of Solid State Chemistry. 180 (2007) 2121–2128.

[48] D. De la Fuente, I. Díaz, J. Simancas, B. Chico, M. Morcillo, Long-term atmospheric corrosion of mild steel, Corrosion Science. 53 (2011) 604–617.

[49] C. Kim, A.I. Karayan, J. Milla, M. Hassan, H. Castaneda, Smart Coating Embedded with pH-Responsive Nanocapsules Containing a Corrosion Inhibiting Agent, ACS Appl. Mater. Interfaces. 12 (2020) 6451–6459.

[50] T. Kamimura, S. Hara, H. Miyuki, M. Yamashita, H. Uchida, Composition and protective ability of rust layer formed on weathering steel exposed to various environments, Corrosion Science. 48 (2006) 2799–2812.

6. CONCLUSIONS AND FUTURE RECOMMENDATIONS

6.1. Conclusions

To overcome the limitations of conventional organic and inorganic coating systems in terms of the substrate protection from corrosion attack, especially with the presence of unintentionally formed defects or during their longer service time, this research investigated the applicability of modifying surface, specifically an interface between electrolyte and substrate, via nanocapsule embedded coating and Al-Si-Mg coating systems. Electrochemical properties related to impedance were examined and characterized through various experimental techniques in order to understand the changes observable at the surface during the immersion tests. The findings of this study can be summarized as follows:

- The encapsulation of triethanolamine (TEA) as a corrosion inhibitor was successfully performed via a free-radical microemulsion polymerization. The mean particle size of the nanocapsules produced was 450 nm, and an enhanced corrosion inhibiting releasing behavior was observed at the biased pH levels, indicating the corrosion reactions that causes local pH gradient by forming local galvanic cell can induce an autonomous self-healing effect that can delay the degradation of substrate by corrosion phenomena.

- The encapsulated TEA was embedded into conventional epoxy coating to study the applicability of such nanocapsules to protect the aluminum alloy with the presence of artificially defected area. After the initiation of corrosion reactions by chloride ion containing electrolyte, the coating with the embedded TEA nanocapsules successfully released the corrosion inhibitor to form an inhibiting layer throughout the experimental period to isolate the substrate from the corrosive electrolyte. Such enhanced anti-corrosion characteristics were evidenced by both electrochemical parameters obtained from EIS and SVET, and characteristic techniques from optical microscopy, SEM-EDS, and NMR. As the noticeable suppression of the corrosion activity was only observed from the sample with embedded TEA nanocapsules, this study verified the coating with the addition of TEA nanocapsules can provide a long-term aluminum alloy protection even under a chloride-rich environment.

- To address more practical applicability of the nanocapsules, such concept was adopted to epoxy-coated-rebar (ECR) system with wider artificially defective area under simulated carbonated concrete pore solution environment to examine the effect of the embedded nanocapsules in epoxy coating versus corrosion phenomena. Compared to the control sample that revealed a freely corroding regime of the exposed rebar substrate, the coating with TEA nanocapsules clearly revealed considerably delayed surface morphology, evidenced by both electrochemical and characteristic techniques. Nevertheless, compared to the

aluminum alloy study that showed long-term substrate protection, the applied TEA nanocapsule containing coating provided only short-term substrate protection. This may due to either the absence of native oxide layer in reinforcing steel surface that can intensify the inhibiting efficiency or the wider artificially defected area created in this study. To overcome these limitations, the proposed future study shown in the next section can be used as an important guide for an optimal design of the organic coating embedded with inhibitor containing nanocapsules.

- To improve an anti-corrosion performance of the conventional Al-Si inorganic coating that has been used for hot-press-forming steel system, the addition of Mg element to form Al-Si-Mg coating was proposed. Compared to the conventional Al-Si coating system, the addition of Mg element caused a modified microstructures throughout the coating system via segregation of Mg element during the heat treatment, evidenced by both top-most surface and cross-sectional micrographs. Compared to the conventional Al-Si coating sample that showed a severe corrosion regime upon the exposure to corrosive electrolyte, the Al-Si-Mg coating with such structural changes depicted enhanced anti-corrosion characteristics supported by electrochemical parameters and post-immersion characterization. The improved barrier protection of the Al-Si-Mg coating by Mg segregation can potentially probe the utilization of segregating features of IIA element family, not only limited to Mg element but also Ca or Sr, to improve the

anti-corrosion features of such coating to suppress corrosion activity of hot-press-forming ultra-high-strength-steel for automotive industry.

6.2. Future Recommendations

It is expected that the research will be proceeded to overcome the limitations observed in this study. Based on the outcomes of this research, the following future takes are recommended.

1) Relationships among the amount and distribution of nanocapsules, size of artificially defected area, and the inhibiting effect: The epoxy coating embedded with nanocapsules used in this study relied on much amount and random distribution of nanocapsules during the sample preparation. Depends on the previous studies [1–3], it has been shown the position of nanocapsules can affect the inhibiting efficiency. In order to maximize the corrosion inhibiting performance with minimize addition of nanocapsules, it is required to elucidate the relationship between the amount and distribution of nanocapsules, size of artificially defected area, and the inhibiting effect. This finding will benefit the future self-healing coating designer to design more optimized self-healing systems.

2) Addition of other 2A family elements into the conventional Al-Si coating system: The proposed study only has discussed with the addition of Mg element.

Meanwhile, the other elements belonged to 2A family, such as Ca or Sr, are known to have greater oxidizing power and great mobility [4,5]. Hence, the addition of such element potentially provides an enhanced substrate protection not only via the barrier protection but also the cathodic protection mechanism, by the difference in oxidizing power between Al and 2A elements. Additionally, the formation of new intermetallic phases is also expected, and revealing their roles in electrochemical system also benefit the development of aluminized coating for hot-press-formed ultra-high-strength-steel.

6.3. References

[1] D. Borisova, D. Akçakayıran, M. Schenderlein, H. Möhwald, D.G. Shchukin, Nanocontainer-Based Anticorrosive Coatings: Effect of the Container Size on the Self-Healing Performance, Advanced Functional Materials. 23 (2013) 3799–3812.

[2] D. Borisova, H. Möhwald, D.G. Shchukin, Influence of Embedded Nanocontainers on the Efficiency of Active Anticorrosive Coatings for Aluminum Alloys Part II: Influence of Nanocontainer Position, ACS Appl. Mater. Interfaces. 5 (2013) 80–87.

[3] D. Borisova, H. Möhwald, D.G. Shchukin, Influence of embedded nanocontainers on the efficiency of active anticorrosive coatings for aluminum alloys part I: influence of nanocontainer concentration, ACS Applied Materials & Interfaces. 4 (2012) 2931–2939.

[4] J. Emsley, Nature's building blocks: an AZ guide to the elements, Oxford University Press, 2011.

[5] D. Heiserman, Exploring chemical elements and their compounds, McGraw-Hill, 1991.

APPENDIX A

DISTINCTION BETWEEN CORROSION INHIBITOR AND CORROSION INHIBITION EFFECT[*]

To clearly understand the mechanisms of the successful spontaneous repassivation of aluminum alloy during the long-term immersion test, it is needed to distinguish the difference between corrosion inhibitor and corrosion inhibition effect. Therefore, the definitions of the corrosion inhibitor and corrosion inhibition effect were illustrated in this part, and the their distinctions in electrochemical impedance spectroscopy were shown based on the experimental data shown in Chapter 3.

A.1. Direct Contribution of Corrosion Inhibitor

Corrosion inhibitor is any chemical substance which is added to an electrolyte to enhance the anti-corrosion performance of substrate. It may modify electrochemical reactions by their actions from either electrolyte or metal/electrolyte interface [1]. In case of the triethanolamine (TEA) as a type of corrosion inhibitor used in the studies, it is an amine-based corrosion inhibitor which can be classified as an adsorption corrosion inhibitor [2]. Such type of corrosion inhibitor can form chemisorptive bonds on the metal

[*] Part of this section is reprinted with permission from "Smart coating embedded with pH-responsive nanocapsules containing a corrosion inhibiting agent" by Changkyu Kim, Ahmad Ivan Karayan, Jose Milla, Marwa Hassan, and Homero Castaneda, 2020. *ACS Applied Materials & Interface*, 12, 6451-6459, Copyright © 2020 American Chemical Society.

surface by donating electrons, and once such bonds are formed with having an array feature, the hydrocarbon tails of the amine-based chemical which face away from the metal surface. Therefore, the arrayed hydrocarbon tails that are hydrophobic can provide a barrier protection by keeping the corrosive ions away from the electrolyte/metal interface. Hence, we can conclude the addition of TEA corrosion inhibitor, either it is applied directly into electrolyte or indirectly via coating with embedded nanocapsules, directly contributes to enhance the anti-corrosion performance of the exposed metal surface.

A.2. Indirect Contribution of Native Oxide Layer

Meanwhile, the corrosion inhibition effect represents consequential phenomena related to the substrate degradation. It can be caused by the contribution of corrosion inhibitors, but also caused by the formation of native passive layer in the case of aluminum alloy. Compared to the corrosion inhibitor that represented a direct and relatively more independent contribution for an enhanced anti-corrosion performance, the formation of native passive layer of metal tends to rely on either its inherent material property or surrounding environment, such as metal type, surrounding pH, and presence of corrosive ions [3]. With the presence of external barrier protection provided by either coating or inhibiting layer which both represent direct enhancement of anti-corrosion property, the recovery of native oxide layer by having an isolated regime from the corrosive environment can be considered as an indirect contribution towards enhanced anti-corrosion performance.

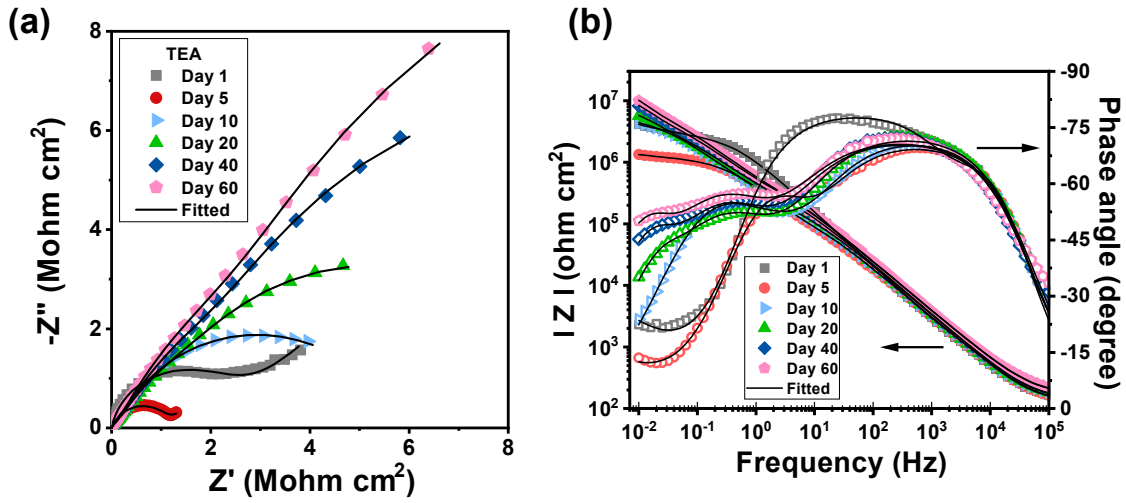

Figure A.1. (a) Nyquist plot and (b) Bode plot for the corrosion of aluminum alloy 3003 in 5 wt % NaCl with the presence of encapsulated TEA embedded in organic coating.

A.3. Mixed Contribution

Both direct and indirect contributions towards suppressed corrosive activity are well-illustrated in Figure A.1 which were taken from Chapter 3. According to the Bode plots it is observable that there is an evolution of time-constant (TC) at the frequency around 0.5 Hz after day 5 which can be considered as the formation of inhibiting layer by the direct contribution of TEA species which were released from the embedded nanocapsules then successfully chemisorbed at the exposed metal surface. Meanwhile, we can also observe another TC at the lower frequency at around 20 mHz which is indicative of the metal/electrolyte interface, and over the immersion period, it showed a gradual recovery of its semi-capacitive behavior represented by the higher phase angle value which can be considered as the recovery of native oxide layer of the aluminum alloy. Such also reveals that the faradaic reactions were suppressed at the metal/electrolyte interface,

and this is owing to not only the direct contribution of the TEA corrosion inhibitors but also from the indirect contribution of the recovery of native oxide layer, and both could have co-existed to provide a more durable and long-lasting anti-corrosive barrier protection.

A.4. References

[1] E. McCafferty, Introduction to corrosion science, Springer Science & Business Media, 2010.

[2] T. Szauer, A. Brandt, On the role of fatty acid in adsorption and corrosion inhibition of iron by amine—fatty acid salts in acidic solution, Electrochimica Acta. 26 (1981) 1257–1260.

[3] M. Pourbaix, Atlas of electrochemical equilibria in aqueous solutions, National Association of Corrosion Engineers, 1974.

APPENDIX B

EXAMINATION OF CORROSION INHIBITOR RELEASING BEHAVIOR FROM NANOCAPSULES: RELATIONSHIPS AMONG TIME, PH, AND CONCENTRATION

To clearly understand the kinetics of the corrosion inhibitor releasing behavior, specifically the releasing behavior of triethanolamine (TEA) from the embedded nanocapsules, the regression on the experimental data was performed based on a mathematical model that contains the experimental parameters.

B.1. Mathematical Regression Approach

To address the releasing behavior of the TEA from the nanocapsules, the Nuclear Magnetic Resonance (NMR) experiments were performed as illustrated in Chapter 2. Such examination of the releasing behavior also allows to build the relationships among the experimental parameters including time, pH level, and concentration of TEA released. The simulated tracings of the released TEA from the nanocapsules are shown in Figure B.1, based on the kinetical relationships represented in equation B.1:

$$C(T, pH) = T^{a} log_{10} T + |pH - 7|^{b} \quad \text{(B.1)}$$

where *C*, unit of mMol, represents the concentration of TEA at certain time and pH level, *T*, unit of hour, represents the immersed time under water, and *pH* represents the pH level

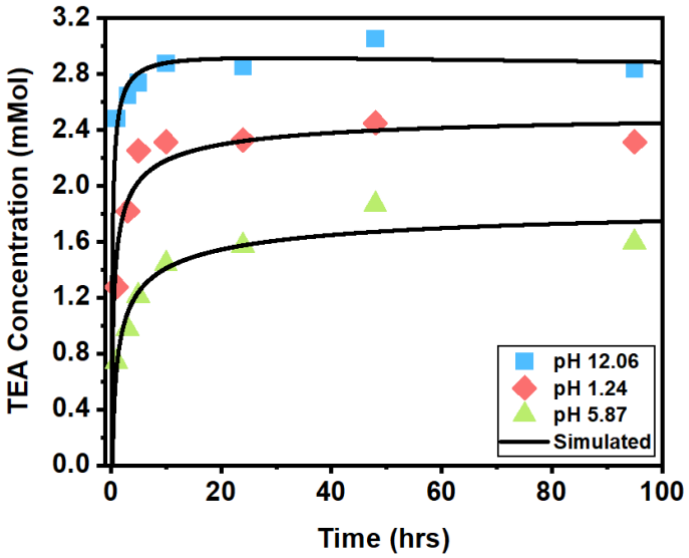

Figure B.1. TEA releasing behavior of nanocapsules in different pH range with simulated results.

of the electrolyte. The *a* and *b* are the coefficients for the varied pH levels, as the releasing kinetics are estimated to represent a strong dependance in the experimental pH levels. The coefficients for the tested pH levels are shown in Table B.1.

Table B.1. Coefficients for the kinetic model in the tested pH levels.

	a	*b*
pH 5.87	-0.1361	-3.165
pH 1.24	-0.1591	0.2272
pH 12.06	-0.2956	0.5331

According to the coefficients shown in Table B.1, it is noticeable that the parameter *a* tends to have relatively more negative values at the biased pH levels, either

acidic or basic, compared to that of the neutral pH case. This can be related to the early period TEA releasing behavior in terms of the level of ionization. At the biased pH levels the TEA could have been ionized in a relatively faster manner which have resulted in higher TEA concentration within a short time period (< 1 hr), therefore the time term as *T* represented relatively irrelevant relationship with the TEA concentration compared to the neutral pH level one. Meanwhile, the parameter *b* shows relatively more positive values in the cases of the biased pH levels. This can be understood as the contribution of pH gradient to the TEA concentration. Specifically, compared to the neutral sample that revealed negative *b* values, the parameters for biased pH levels represent positive values. This is indicative, at the biased pH levels, the dominating factor for the TEA concentration would be pH level rather than time, and this also evidences the conceptual features of the nanocapsules equipped with pH-sensitive releasing behavior.